Centro Brasileiro de Pesquisas Físicas

Doctoral Thesis

# On the elastic excitation of spin waves and the magnetoelastic interaction

by

Danilo Froes Batista

Supervised by
João Paulo Sinnecker, Mercedes Arana and Luiz Sampaio

Rio de Janeiro, Brazil
March, 2023

“ON THE ELASTIC EXCITATION OF SPIN WAVES AND THE MAGNETOELASTIC INTERACTION”

**DANILO FROES BATISTA**

Tese de Doutorado em Física apresentada no Centro Brasileiro de Pesquisas Físicas do Ministério da Ciência Tecnologia e Inovação. Fazendo parte da banca examinadora os seguintes professores:

João Paulo Sinnecker - Orientador/CBPF

Felipe Bohn - UFRN

Fanny Béron - UNICAMP

Angela Burlamaqui Klautau - UFPA

Joaquim Bonfim Santos Mendes - UFV

Rio de Janeiro, 11 de abril de 2023.

**Centro Brasileiro de Pesquisas Físicas – CBPF**
Coordenação de Matéria Condensada, Física Aplicada e Nanociências (COMAN)

# On the elastic excitation of spin waves and the magnetoelastic interaction

**Danilo Froes Batista**

Thesis submitted to the Brazilian Center for Physical Research (CBPF) Physics graduate program in partial satisfaction of the requirements for the degree of Doctor of Philosophy in Physics.

Supervised by: **João Paulo Sinnecker**
**Mercedes Arana**
**Luiz Sampaio**

Rio de Janeiro, Brazil
March, 2023

*To my parents, Maria José and Celso,*
*this is a testament to the seeds you*
*sowed and the roots you nurtured with*
*unwavering love and support.*

# Resumo

Esta tese investiga o acoplamento entre ondas elásticas e ondas de spin em filmes finos ferromagnéticos e suas potenciais aplicações em spintrônica e magnônica. Nos últimos anos, tem havido um crescente interesse em utilizar ondas de spin para desenvolver dispositivos de processamento de informação de baixo gasto energético e alta velocidade. A interação magnetoelástica, que acopla a magnetização às vibrações elásticas de um material magnético, tem sido extensivamente estudada nesse campo devido ao seu potencial uso para a manipulação de ondas de spin com eficiência energética.

Três simulações numéricas foram conduzidas nesta tese para investigar a interação magnetoelástica. A primeira simulação focou na propagação de uma onda acústica externa através de uma fita de Ni magnetoelástica sob diferentes níveis de acoplamento entre as ondas. Quando as ondas acústicas são altamente atenuadas, as ondas de spin são livres para propagar, mas desaparecem após um comprimento de decaimento. Por outro lado, quando a atenuação das ondas acústicas é muito menor do que a das ondas magnéticas, ambas as ondas propagam-se juntas, mantendo a amplitude constante. Essa simulação também calcula os componentes AC e DC da voltagem do efeito Hall de spin inverso (ISHE) que podem ser medidos em uma linha de Pt adjacente.

Na segunda simulação, investigamos a conversão de magnons em fônons em um campo magnético variável no espaço. Para isso, resolvemos simultaneamente as equações de dinâmica de magnetização e elastodinâmica, que são acopladas através da interação magnetoelástica. Essa abordagem aproveita o fato de que as curvas de dispersão magnética e elástica formam um *gap* entre si devido ao acoplamento magnetoelástico, separando-se em dois ramos. Iniciamos um pacote de onda na região quasi-magnética da curva de dispersão acoplada. Conforme esse pacote de onda se propaga através do campo estático variável no espaço, ele gradualmente varia seu comprimento de onda, mantendo sua frequência constante, transitando da região quasi-magnética para a região magnetoelástica, seguida pela região quasi-elástica. Isso resulta na conversão de uma excitação magnética em uma excitação elástica, o que pode ser verificado pela conversão da energia magnética em elástica.

Na última simulação, investigamos os modos magnéticos e elásticos, bem como a relação de dispersão, de guias de onda que contêm uma parede de domínio de Néel. As paredes de domínio são canais naturais para a propagação de ondas de spin, pois o campo desmagnetizante devido à rotação da magnetização cria um poço de potencial que confina as ondas em

sua largura, formando modos magnéticos protegidos topologicamente. Nessa simulação, investigamos como os modos elásticos, na presença da interação magnetoelástica, influenciam a dinâmica da magnetização na presença da parede de Néel. Nossas descobertas indicam que nos pontos de cruzamento na relação de dispersão, dois comportamentos diferentes podem ser observados: a formação de um *gap* quando existe um acoplamento forte, ou um ponto sem *gap* quando o feedback magnetoelástico não é completamente satisfeito. Analisamos que para a formação do *gap*, os modos elástico e magnético precisam ter uma sobreposição significativa, o que não acontece no modo confinado à parede de Néel, além de possuir a mesma simetria espacial.

Além das simulações numéricas, esta tese também inclui trabalho experimental que não foi totalmente concluído, e decidimos não incluí-lo no texto principal, mas é apresentado como um apêndice, como um guia para pesquisas futuras. Os experimentos envolvem a deposição de filmes finos piezoelétricos de ZnO por *magnetron sputtering*, a caracterização dos filmes usando microscopia eletrônica e experimentos de raios-X, e a fabricação de transdutores interdigitais sobre um substrato magnético de YIG usando litografia de feixe de elétrons e litografia a laser. Além disso, realizamos medidas de transporte elétrico nos transdutores interdigitais e experimentos de espalhamento de luz de Brillouin. O objetivo dos experimentos era obter experimentos de conversão magnon-fônon excitando ondas acústicas de superfície com os transdutores interdigitais, o que impulsionaria a dinâmica de magnetização de YIG.

Em conclusão, esta tese investiga a dinâmica de ondas de spin e ondas elásticas em materiais magnetoelásticos por meio de simulações numéricas. Esperamos que os resultados contribuam para a compreensão do papel dessa interação na dinâmica das ondas de spin e possam ser aplicados no desenvolvimento de novos dispositivos de processamento de informações.

**Palavras-chave**: Dinâmica de magnetização, ressonância ferromagnética, ondas de spin, ondas elásticas, ondas acústicas, magnon, fônon, interação magnetoelástica, bombeamento de spins, efeito Hall de spin inverso, parede de domínio de Néel, spintrônica, magnônica.

# Abstract

This thesis investigates the coupling between elastic and magnetic waves in ferromagnetic thin films and their potential applications in spintronics and magnonics. In recent years, there has been increasing interest in utilizing spin waves for developing low-power, high-speed information processing devices. The magnetoelastic interaction, which allows coupling between the magnetization and elastic vibrations of a magnetic material, has been studied extensively in this field due to its potential for energy-efficient manipulation of spin waves.

Three simulations were conducted in this thesis to investigate the magnetoelastic interaction in different structures. The first simulation focused on the propagation of an external acoustic wave through a magnetoelastic Ni stripe under different levels of coupling between the waves. When acoustic waves are highly attenuated, the spin waves are free to propagate but vanish after the decay length. On the other hand, when the acoustic wave attenuation is much lower than the magnetic waves, both spin and acoustic waves propagate together with the spin-wave maintaining the amplitude constant. This simulation also calculates the AC and DC components of the inverse spin Hall effect (ISHE) voltage that could be measured in an adjacent Pt stripe.

In the second simulation, we investigated the conversion of magnons into phonons in a spatially varying magnetic field, simultaneously solving the equations of magnetization dynamics and elastodynamics, which are coupled via the magnetoelastic interaction. This approach utilizes the fact that the magnetic and elastic dispersion curves form a gap between them due to the magnetoelastic coupling, separating into two branches. We initiated a wavepacket in the quasi-magnetic region of the coupled dispersion curve. As it propagates through the spatially varying static field, it gradually changes its wavelength while maintaining its frequency, thus transitioning to the magnetoelastic region, followed by the quasi-elastic region. This results in the conversion of a magnetic excitation into an elastic excitation, which can be verified by the conversion of magnetic energy into elastic energy.

In the final simulation, we investigated the magnetic and elastic modes, as well as the dispersion relation, of waveguides containing a Néel-type domain wall. Domain walls are natural channels for the propagation of spin waves, as the demagnetizing field due to the rotation of magnetization creates a potential well that confines the waves in their width,

forming topologically protected magnetic modes with increased propagation distances. In this simulation, we investigated how elastic modes, in the presence of magnetoelastic interaction, influence the magnetization dynamics in the presence of the Néel wall. Our findings indicate that at the crossing points in the dispersion relation, two different behaviors can be observed: the formation of an anticrossing gap when there is strong coupling, or a gapless point when the magnetoelastic feedback cycle is not completely satisfied. Our analysis showed that the formation of an anticrossing gap in the dispersion relation occurs when there is a significant overlap between the elastic and magnetic modes, which is not the case for the Néel wall-confined mode, and that matching symmetries are necessary for the other modes to exhibit gapless crossings.

In addition to the numerical simulations, this thesis includes experimental work that has not been fully concluded. While this work was not included in the main text, it is presented as an appendix to serve as a guide for future research. The aim of the experiments was to obtain magnon-phonon interactions by exciting surface acoustic waves with interdigital transducers on a piezoelectric ZnO film, which would drive the magnetization dynamics of a magnetoelastic YIG substrate. The experimental work involved the deposition of ZnO using magnetron sputtering, its characterization using electron microscopy and X-ray experiments, and the fabrication of interdigital transducers using electron beam and laser lithography. In addition, we performed electric transport measurements and Brillouin light scattering experiments.

In conclusion, this thesis investigates spin wave and elastic wave dynamics in magnetoelastic materials through numerical simulations. The results of the simulations will hopefully contribute to the understanding of the role of the magnetoelastic interaction in spin wave behavior and have potential applications in developing novel information processing devices.

**Keywords**: Magnetization dynamics, ferromagnetic resonance, spin waves, elastic waves, acoustic waves, magnon, phonon, magnetoelastic interaction, spin pumping, inverse spin Hall effect, Néel domain wall, spintronics, magnonics.

# Acknowledgements

I am grateful to many people who have supported me throughout the journey of completing this thesis. First and foremost, I want to express my deep appreciation to my supervisors, João Paulo Sinnecker, Mercedes Arana, and Luiz Sampaio, for their unwavering support, encouragement, and guidance throughout every step of this research. Without their invaluable presence and mentorship, this work would not have been possible. I also want to extend my heartfelt thanks to Professor Sérgio Rezende for his support, scientific ideas, and insightful discussions that have enriched my research experience.

I am also deeply grateful to my family, who invested so much effort in my education and have always been my biggest supporters. I want to highlight the contributions of my father Celso, my mother Maria José, my brother Matheus, my aunt Maria, and my life partner Pedro. They have been the bedrock of my academic journey, and this thesis would not exist without their unwavering support.

To my friends who have always been there for me, thank you for the moral support and encouragement that have kept me going during challenging times. I would also like to thank the staff and my colleagues at CBPF, who provided me with a stimulating and supportive research environment. Their contributions have been instrumental in the successful completion of this thesis.

Finally, I want to acknowledge the financial support provided by CNPQ, CAPES, and FAPERJ, which has enabled me to carry out this research.

# List of Publications

- Magnetoelastic modes in Néel domain walls
  **D. Froes**, M. Arana, L. C. Sampaio, and J. P. Sinnecker.
  Journal of Applied Physics, 132(22): 223908, December 2022.
  https://doi.org/10.1063/5.0128775

- Acoustic wave surfing: spin waves and spin pumping driven by elastic wave
  **D. Froes**, M. Arana, L. C. Sampaio, and J. P. Sinnecker.
  Journal of Physics D: Applied Physics, 54(25): 255001, April 2021.
  https://doi.org/10.1088/1361-6463/abed71

# Table of Contents

**List of Figures** xiii

**List of Tables** xxiii

**1 Introduction** 1

1.1 State of the art . . . 1

1.2 Objectives . . . 4

1.3 Overview of the thesis . . . 5

**2 Theoretical Background** 7

2.1 Magnetization dynamics . . . 7

2.1.1 Landau-Lifshitz-Gilbert (LLG) equation . . . 7

2.1.2 Magnetic energy terms . . . 10

2.2 Ferromagnetic Resonance (FMR) . . . 14

2.2.1 Magnetic resonance driven by alternating field . . . 15

2.2.2 Magnetic resonance in ferromagnets . . . 16

2.2.3 Spin pumping and inverse spin Hall effect (ISHE) . . . 18

2.3 Spin waves . . . 22

2.3.1 Linear chain of classical spins . . . 22

2.3.2 Spin waves in a bulk ferromagnet . . . 24
2.3.3 Spin waves in thin films . . . 26
2.4 Elastic waves . . . 29
2.4.1 Elastodynamics . . . 29
2.4.2 Elastic waves in thin films . . . 31
2.4.3 Elastic waves in waveguides . . . 31
2.5 Magnetoelastic waves . . . 35
2.5.1 Magnetoelastic interaction . . . 36
2.5.2 Magnetoelastic waves in bullk ferromagnet . . . 37
2.5.3 Magnetoelastic waves in thin films . . . 41

**3 Methods** **48**
3.1 Micromagnetic simulations . . . 48
3.2 Magnetoelastic extension . . . 49
3.3 Processing simulation data . . . 50

**4 Results and Discussion** **52**
4.1 Spin waves and spin pumping driven by elastic waves . . . 53
4.1.1 Introduction . . . 53
4.1.2 Simulation setup . . . 54
4.1.3 Results: Spin wave propagation modes . . . 55
4.1.4 Results: Spin pumping and inverse spin Hall effect (ISHE) . . . 61
4.1.5 Discussion . . . 66
4.1.6 Conclusions . . . 67
4.2 Magnon-phonon interconversion in a spatially non-uniform field . . . 68
4.2.1 Introduction . . . 68

4.2.2 Simulation setup . . . 69
4.2.3 Results . . . 70
4.2.4 Conclusions . . . 79
4.3 Magnetoelastic waves in Néel-type domain walls . . . 80
4.3.1 Introduction . . . 80
4.3.2 Simulation setup . . . 81
4.3.3 Results and discussion: Uncoupled elastic and magnetic modes . . . 84
4.3.4 Results and discussion: Coupled magnetoelastic modes . . . 88
4.3.5 Conclusions . . . 94

**5 Summary and Perspectives** **96**
5.1 Summary . . . 96
5.2 Perspectives . . . 98

**References** **101**

**APPENDICES** **117**

**A Experimental work** **118**
A.1 Introduction . . . 118
A.2 Objectives . . . 119
A.3 Methods . . . 120
A.3.1 Sample fabrication . . . 120
A.3.2 Sample characterization . . . 121
A.4 Preliminary results . . . 123
A.4.1 Device fabrication . . . 123
A.4.2 Device characterization . . . 129
A.5 Conclusion and future work . . . 136

# List of Figures

2.1 Schematic representation of the magnetization dynamics, as described by the Landau-Lifshitz-Gilbert equation. In (a), the magnetization undergoes a precession motion around the effective field direction in the absence of damping. In (b), the dynamics with damping is shown, resulting in a gradual reduction of the amplitude over time. . . . . 9

2.2 Demagnetizing tensor components for simple geometries, respectively, a sphere, an infinite film and an infinitely long cylinder. . . . . 12

2.3 Spins equilibrium position due to the exchange interaction in different magnetic materials. In panel (a), a ferromagnetic material is presented where the spins are parallel to each other. Panel (b) shows an antiferromagnetic material where the spins are antiparallel. Similarly, panel (c) shows a ferrimagnetic material, but unlike the antiferromagnetic case, the opposite spins do not cancel each other, leading to a net magnetic moment in the ferrimagnetic material. . . . . 13

2.4 (a) Real and (b) imaginary parts of magnetic susceptibility as a function of the frequency for different external magnetic field intensities calculated from equations 2.43 and 2.44 for a 14 nm Permalloy thin film ($M_s = 800kA/m$ and $A_{ex} = 13pJ/m$).The imaginary part exhibits a Lorentzian curve with a peak at the FMR frequency, and the damping of the material can be calculated from its width at half maximum. . . . . 19

2.5 The figure illustrates (a) spin pumping and (b) the inverse spin hall effects (ISHE). The magnetization dynamics of a ferromagnet can induce a spin current in a neighboring non-magnetic material through the spin pumping phenomenon, as shown in (a). On the other hand, in a non-magnetic material with strong spin-orbit coupling, spins with opposite orientation are deflected to opposite directions, which is known as the ISHE, as depicted in (b). When the incoming current is spin polarized, the spin accumulation in the opposite directions will not be equal, and this will result in a potential difference between them, leading to the ISHE voltage ($V_{ISHE}$). . . . . 20

2.6 A schematic representation of a spin wave in a linear chain of spins coupled by the exchange interaction. As the spins precess, they present a phase difference that results in the formation of a spin wave with a constant wavevector. 23

2.7 The dispersion relation for propagating spin waves in a 50 nm-tick Ni film ($M_s = 480kA/m$ and $A_{ex} = 8pJ/m$) under a 10 mT external magnetic field, taking into account both exchange and dipolar interactions from equation 2.80. The two curves plotted represent the backward volume spin waves, which are generated when the magnetization is parallel to the wavevector, and the forward surface waves, which occur when the magnetization is perpendicular to the wavevector. . . . . 28

2.8 Dispersion relation of elastic P-waves propagating in a 20 nm thick, 320 nm wide CoFeB waveguide ($\rho = 8000kg/m^3$, $C_{11} = 283GPa$, $C_{12} = 166GPa$, and $C_{44} = 58GPa$), obtained from equation 2.101. . . . . 33

2.9 Dispersion relation of elastic (a) S-waves and (b) A-waves propagating in a 20 nm thick, 320 nm wide CoFeB waveguide ($\rho = 8000kg/m^3$, $C_{11} = 283GPa$, $C_{12} = 166GPa$, and $C_{44} = 58GPa$), obtained from equations 2.111 and 2.112. . . . . 35

2.10 Dispersion curves for elastic waves and spin waves in a bulk CoFeB sample ($M_S = 1.2MA/m$, $A_{ex} = 18pJ/m$, $\rho = 8000kg/m^3$, $C_{11} = 283GPa$, $C_{12} = 166GPa$, $C_{44} = 58GPa$, and $B_1 = B_2 = -8.8MJ/m^3$), obtained from equation 2.137. Panel (a) represents the uncoupled waves, while panel (b) includes the coupling between them, resulting in the hybridization of the curves and the formation of an anticrossing gap between the transverse elastic and the spin wave. The upper branch of the hybridized curves transitions from quasi-magnetic to quasi-elastic behavior, while the lower branch transitions from quasi-elastic to quasi-magnetic. . . . . 40

2.11 The dispersion curves for magnetoelastic waves with magnetization parallel to the wave vector in a 20 nm thick CoFeB film ($M_S = 1.2MA/m$, $A_{ex} = 18pJ/m$, $\rho = 8000kg/m^3$, $C_{11} = 283GPa$, $C_{12} = 166GPa$, $C_{44} = 58GPa$, and $B_1 = B_2 = -8.8MJ/m^3$), obtained from equation 2.172. The plot reveals that the longitudinal elastic wave ($\omega_x$) does not couple to spin waves ($\omega_m$), whereas the transverse elastic waves ($\omega_y$ and $\omega_z$) hybridize and form an anticrossing gap with two branches ($\omega_-$ and $\omega_+$). . . . . 47

4.1 The simulation setup. A Ni stripe with a equilibrium magnetization at $\theta = 45^0$ with the $\hat{x}$-axis under a magnetic field $\vec{H}_0$ applied at a $\theta_H$ angle. Below, we show the elastic excitation applied for three cases: (a) high attenuation, (b) no attenuation, and (c) intermediate attenuation. . . . . 55

4.2 (a) Polar plot of the spatial-FFT amplitude of the spin waves at the wave vector of the acoustic wave as a function of the magnetization angle ($\theta$) under a longitudinal strain excitation ($\varepsilon_{xx}$). (b) The AC magnetoelastic field intensity perpendicular to the static magnetization ($\mu_0 H_{ME}$) under different $\theta$ values for the pure longitudinal strain ($\varepsilon_{xx}$) and for the more complete SAW excitation ($\varepsilon_{xx}+\varepsilon_{zz}+\varepsilon_{xz}$). They both have a maximum at $45^o$, with similar amplitudes, and only significantly differ at $\theta = 0$. . . . . 56

4.3 Strongly attenuated acoustic wave. (a) The magnetization profile of the spin-wave generated by a $f = 6$ GHz and $\lambda = 667$ nm acoustic excitation restricted to the dashed region under a 60 mT field. (b) The dispersion relation under a 60 mT field. The dashed line is the acoustic excitation wave number $k = 2\pi f/v$. The blue dotted lines represent data calculated from an analytical model. (c) The exponential decay length ($x_d$) of the spin-wave. The inset shows the z-magnetization along the x-axis with its exponential decaying amplitude for $\alpha = 10^{-3}$. . . . . 58

4.4 Non-attenuated acoustic wave. (a) Magnetization profile of spin waves excited by propagating acoustic waves with frequency and wavelength as 5 GHz and 800 nm, respectively. (b) The Fourier amplitude of the spin waves for different frequencies. In all cases the main peak coincides with the acoustic wave number (dashed line). (c) FFT power of the excited spin wave as a function of the external magnetic field for waves with frequency $f$ and wave number $k = 2\pi f/v$. . . . . 60

4.5 Partially attenuated acoustic wave. (a) The spatial magnetization profile for an exponentially attenuated acoustic excitation with decay length $x_d = 1\ \mu m$, $f = 4$ GHz and $\lambda = 1\ \mu m$ under a 20 mT magnetic field. The spin-wave transits between the excitation wavelength of 1 $\mu m$ (left) to its natural wavelength value of 256 nm at that field (right). (b) The spin-wave FFT amplitude for different attenuation decay length values $x_d$. The vertical dashed line corresponds to the excitation wave number ($k = 6.28\ \mu m^{-1}$). . 61

4.6 FM/NM (Ni/Pt) bilayer. The strain waves ($\varepsilon_{xx}$) excite the magnetization dynamics of the FM film which, in turn, leads to the generation of a spin current ($\vec{J}_S$) across the film plane. This acoustically driven spin current injected in the NM layer is converted into a charge current, $\vec{J}_C$, by the ISHE and can be detected as electric voltage ($\Delta$V) at the top of the NM line. . . 62

4.7 Spin-current in point $P_0$. (a) Time evolution of the rotated magnetization components. The inset shows the ellipsoidal motion of $m_v$ and $m_z$ around the equilibrium position. (b) The spin-current across the Ni/Pt interface generated by the spin-wave propagation. The components with v- and z-polarization are AC, with null average value, whereas the u-polarized component exhibit a constant value. . . . . 63

4.8 Spin and charge current maps. Spin-current ($J_s$) colormap across the ferromagnet for, respectively, the $\hat{u}$ and $\hat{v}$ spin-polarization directions at a given instant of time (for details see text). The charge current ($J_c$) components in the Pt line are shown as vectors inside the dashed frame. . . . . 64

4.9 ISHE voltage in NM layer. (a) The AC and DC components of the ISHE voltage for a 4 GHz, 1 $\mu$m acoustic excitation. (b) The DC value and AC amplitude as a function of the external field, presenting a resonance peak around the natural dispersion eigenmode. (c) $\Delta V_{ISHE}$ as a function of the square of the strain amplitude ($\varepsilon_{xx}^2$), which is proportional to the acoustic wave excitation power (P), showing a linear behaviour for the DC component and a $\sqrt{P}$ behaviour for the AC amplitude (see text for details). . . . . 65

4.10 The simulation setup. A CoFeB stripe with periodic boundary conditions to simulate an infinite film with a static magnetic field ($\mathbf{B}_{DC}$) applied in the y-direction. An alternate magnetic field ($\mathbf{B}_{AC}$) is applied in the x-axis in yellow region in order to drive the spin dynamics. Plane spin waves are excited and propagate along the x-axis, perpendicular to the magnetization direction. . . . . 69

4.11 The dispersion relation for magnetoelastic waves propagating along the x-direction, $\vec{k} = k_x\hat{x}$, under a static field of $\vec{B}_{DC} = (100\text{ mT})\hat{y}$. This was obtained by applying a fast-Fourier transform (FFT) of (a) $m_x$, (b) $u_x$, (c) $u_y$ and (d) $u_z$ along the x-axis. Similar results are found for the FFT of $m_x$ and $m_z$. The magnetoelastic crossover is only present at $m_x$, $m_z$ and $u_y$. For the other displacement directions only the elastic component is present with a longitudinal velocity of 5938 m/s and a transverse velocity of 2683 m/s. . . . . 71

4.12 The magnetoelastic dispersion relation obtained from the FFT of $u_y$ at an external magnetic field of (a) 40 mT and (b) 200 mT, perpendicular to the static magnetization direction. The horizontal dashed line corresponds to the frequency $f = 25$ GHz. . . . . 73

4.13 The resulting wavenumber ($k_x$) for a 25 GHz excitation for (a) the uncoupled system, with magnetoelastic constants ($B_1$ and $B_2$) set to zero, and for (b) the magnetoelastic coupled system. . . . . 74

4.14 The spatially-varying external magnetic field, $H(x)$. It decreases quadratically from a 300 mT to a 30 mT intensity. A magnetic pulse is excited at the x = 5 $\mu m$ position and propagates in the $+x$ direction. . . . . 75

4.15 Pulse propagation under a spatially-varying magnetic field. The images show $m_x$ as a function of the time. The pulse is excited at the x = -5 $\mu m$ position. The red and blue colors correspond to, respectively, positive and negative variations of the magnetization x-component. . . . . 76

4.16 (a) The wavenumber $k_x$ of the pulse measured from the spatial FFT as a function of the time as the pulse propagates in the +x direction. (b) The FFT amplitude for the corresponding wavenumber along the pulse propagation. The vertical dashed line shows the instant in which the excitation field is turned off. . . . . 77

4.17 The energy components of the system as a function of time. The magnetic energy is evaluated as the sum of the magnetostatic, exchange and Zeeman energies, and the elastic one as the sum of the Hooke's with the kinetic components. The vertical dashed line shows the instant in which the excitation field is turned off. . . . . 78

4.18 Sketch of the thin magnetic stripe of two oppositely magnetized domains with the Néel wall between them. The arrows show the direction of the magnetization at equilibrium, and the yellow stripe indicates the region where the external pulse is applied to generate spin and elastic waves. . . . 81

4.19 The magnetoelastic feedback. Scheme of the magnetoelastic interaction, the magnetization dynamics creates a force density, through the magnetostrictive effect, that drives the elastic displacement dynamics that, for instance, creates an effective magnetoelastic field from the inverse magnetostriction that drives the magnetization. This system can feedback itself generating two coupled oscillators. . . . . 82

4.20 Dispersion relation of the coupled magnetoelastic system. (a) The curves were obtained from the magnetization and elastic displacement FFT in the numerical simulation. Due to the magnetoelastic interaction, several crossing points are separated by a gap into two branches, e.g., point "2", but also with several gapless crossing, as points "1" and "3". (b) Identification of the modes, obtained by calculation of analytical dispersion curves from theory. . . . . 83

4.21 Uncoupled magnetic and elastic eigenmodes obtained from micromagnetic simulations with null coupling constants, $B_1 = B_2 = 0$. The finite width of the waveguide creates modes with quantized wave vector values in the y-direction. (a) The out-of-plane elastic waves, P-waves with null $\Delta u_x$ and $\Delta u_y$. (b) The two types of in-plane elastic waves, A-waves and S-waves, which have, respectively antisymmetric and symmetric $\Delta u_x$, the opposite for $\Delta u_y$, and null $\Delta u_z$ values. (c) The magnetic modes for the Néel wall, first the domain-wall confined mode, $\mathrm{SW}_{Neel}$, then the modes of the uniform domains, $\mathrm{n}_1$ and $\mathrm{n}_2$. The red and blue colors represent, respectively, positive and negative values. . . . . 85

4.22 Point "1" in the dispersion relation: the gapless crossing between $\mathrm{SW}_{Neel}$ and $\mathrm{A}_0$. Starting from the top left image, we show for the results of the numerical simulation of the magnetoelastic coupled system, in clockwise direction, the magnetization $\Delta m$, the body force $F_{mel}$ [$\mathrm{N/m^3}$], the elastic displacement $\Delta u$ [m], and the magnetoelastic magnetic field $H_{mel}$ [A/m]. This is a gapless crossing point in the dispersion relation as $\mathrm{F}_{mel}$ generated by $\Delta m$, confined to the wall-width, is not located in the same region as the displacement $\Delta u$ of elastic eigenmode, which is spread in the domains. Thus, the elastic and the magnetic systems are uncoupled at that point. . . 89

4.23 Point "2" in the dispersion relation: The coupled crossing of $n_1$ and $A_0$ modes. The numeric simulations at this point show a strong coupling between the magnetic and elastic systems as the $F_{mel}$ generated from the magnetization dynamics $\Delta m$ not only presents a high overlap to the displacement $\Delta u$ of the $A_0$ elastic mode, but also they both carry the same symmetry, antisymmetric for the $\hat{x}$ and $\hat{z}$ components, and symmetric in $\hat{y}$. The same happens between the effective magnetic field $H_{mel}$ and the magnetization $\Delta m$, effectively closing the magnetoelastic feedback cycle, creating an anticrossing gap in the dispersion curve. . . . . 91

4.24 Point "3" in the dispersion relation: the gapless crossing of $n_1$ and $S_1$ modes. In this crossing point, the simulations show that $F_{mel}$ does overlap with $\Delta u$ and $H_{mel}$ overlaps $\Delta m$, but the elastic eigenmode generated by $F_{mel}$ is not equivalent to $S_1$, which the resonant elastic mode at that point. For instance, the $\Delta u$ mode has opposite symmetry from what we would expect for the $S_1$ eigenmode, which would be symmetric in $\Delta u_x$ and antisymmetric in $\Delta u_y$. This way, the elastic and the magnetic systems behave as independent oscillators, and no magnetoelastic gap is formed in the dispersion. . . . . 93

A.1 Wave-vector-resolved Brillouin light scattering (BLS) spectroscopy experimental setup. . . . . 122

A.2 XRD spectra of ZnO films deposited at room temperature (RT) without annealing at 100 W power for different Ar/O2 proportion atmospheres. The film deposited without oxygen (50/0) was the only one not to show the c-axis (002) orientation. . . . . 123

A.3 XRD spectra of ZnO films deposited at room temperature after thermal treatment at (a) 400C and (b) at 600C for one hour at 100 W power for different $Ar/O_2$ proportion atmospheres. . . . . 124

A.4 These FWHM of the (002) peak as a function of the $0_2$ fraction and the annealing temperature are summarized. . . . . 124

A.5 SEM images of the cross section of the $ZnO/SiO_2$ film at different deposition conditions. . . . . 126

A.6 (a) XRD spectra of the ZnO deposited on $SiO_2$ substrates with a 50/10 $Ar/O_2$ atmosphere ratio and thermal treatment for one hour at 600C under different RF power and deposition temperature. (b) XRD spectra of the final ZnO films. The FWHM were, respectively, 0.44 and 0.42 for $SiO_2$ and YIG/GGG substrates. . . . . 127

A.7 Au interdigital transducers fabricated by electron-beam lithography and lift-off. The fingers were designed to have 500 nm width, with 4 $\mu$m separation. 128

A.8 Final sample model. Interdigital transducers (IdTs) on top of two ZnO islands deposited on a YIG/GGG substrate. . . . . 129

A.9 The experimental IdTs electrical transmission setup. The input IdT is connected to a RF signal generator, and the output IdT, to a rectifying diode and a DC voltmeter. . . . . 129

A.10 The rectified DC electrical voltage measured at the output IdT without a bias magnetic field for several input amplitudes for (a) the thick YIG-LPE sample and (b) for the thin YIG-sputtering sample. . . . . 130

A.11 The rectified DC electrical voltage measured at the output IdT with an applied bias magnetic field for the thin YIG-sputtering sample for several frequencies. . . . . 131

A.12 The external magnetic field with maximum absorption measured at the output IdT for the YIG-sputtering sample plotted as a function of the input frequency in the regions with significant transmission. The data is compared to Kittel's equation for ferromagnetic resonance. . . . . 132

A.13 Brillouin light scattering (BLS) spectrum of the sample for a microwave input of 3.4 GHz under three different external magnetic field values. The sample was measured with an incidence angle of $\alpha = 22$ degrees (k = 19.5 $\mu m^{-1}$). . . . . 133

A.14 BLS amplitude, Stokes and Anti-Stokes, at the corresponding microwave frequency for a fixed angle of $\alpha = 22$ degrees (k = 19.5 $\mu m^{-1}$) under different magnetic bias field intensities. . . . . 134

A.15 The BLS peak positions as a function of the external magnetic field for a fixed incidence angle of $\alpha = 22^o$. The dashed lines correspond to the analytical model for magnetostatic surface spin waves for $k = 19.5\mu m^{-1}$, and the dotted lines for $k = 0$ (FMR). . . . . 135

# List of Tables

A.1 Final ZnO magnetron sputtering deposition conditions to optimize the (002) grain orientation. . . . . 127

# Chapter 1

# Introduction

The present thesis aims to investigate the physics of spin wave propagation in ferromagnetic materials and the magnetoelastic interaction, through numerical simulations, which can be useful for both fundamental physics research and information technology applications. In this chapter, we will provide a comprehensive review of the state of the art related to the research topic. Finally, an overview of the structure of the subsequent chapters will be provided.

## 1.1 State of the art

Spin waves, and their quanta magnons, are collective excitations of electron spins in magnetic materials. Introduced by Bloch in 1932 [1], they possess a range of characteristics that are influenced by various parameters, including the direction and intensity of the applied magnetic field, the geometry of the sample, and the choice of magnetic material [2].

The fundamental properties of spin waves, such as their linear and nonlinear wave properties, have attracted considerable interest, particularly with regard to parametric instabilities [3], wavefront reversal [4, 5], soliton formation [6, 7] , and Bose-Einstein condensation [8–10]. In addition to their fundamental properties, spin waves in the GHz and THz frequency ranges have garnered particular interest for potential applications in telecommunications and novel computing devices [11].

The potential applications of spin waves in telecommunications and novel computing devices have sparked a growing interest in the so-called field of magnonics or magnon spintronics [2, 11, 12]. The objective of this research area is to utilize spin waves as a means for the transport and processing of information in logic devices due to their high-speed, efficiency, and low-power consuming properties. This research field has a significant advantage that it shares fabrication techniques with typical CMOS (complementary metal-oxide-semiconductor) technology, which makes it highly compatible and integrable with existing technology. Furthermore, the shorter wavelength of spin waves compared to light in the same frequency range offers the possibility of obtaining wave-like computing devices even in micro and nano-scale, which is highly desirable for the development of future computing technologies.

Moreover, the unique properties of magnons make them an attractive option for the development of novel logic devices. The non-reciprocity property, which describes the different behaviors of magnons in opposite directions of propagation, has been explored in various studies [13–15], and they can also exhibit negative group velocities [16, 17]. Magnons are also anisotropic, meaning that they behave differently in different directions [18, 19], and they can be tuned by external stimuli such as an electric field [20–23], magnetic field [11, 24], and elastic strain [25–27].

In recent years, numerous magnonic devices have been proposed that take advantage of these unique properties. Spin-wave memories, which use magnons to store and retrieve information, have been proposed [28, 29]. Magnon transistors, which can be used to amplify and switch magnonic signals, have also been developed [30–32]. Magnonic diodes have also been proposed, which allow the passage of magnonic signals in one direction while blocking them in the opposite direction [33, 34]. Logic gates that use magnons have been proposed, including AND, OR, and XOR gates [35–37]. Magnonic transducers, which convert magnonic signals into electrical signals, and vice versa, have also been developed [38, 39]. Finally, magnons have been used to develop other radio frequency (RF) components, such as filters [40–42] and circulators [43].

Magnonics encompasses all stages required for the design and operation of logic devices [12]: the excitation of spin waves, their transmission along a waveguide, controlling their properties for performing logic operations, and detecting the output. The control of spin waves can be achieved using patterned magnetic properties [44–47], spin textures [48–50], or through external electric or magnetic fields [28, 51, 52]. However, the two main

challenges in magnonics are efficiently exciting and detecting magnons and overcoming their limited propagation distances, which are typically less than 1 $\mu$m due to intrinsic magnetic damping.

The most common method of excitation of spin waves is using an AC electric current passing through a strip-line antenna [51]. This method generates a non-uniform AC magnetic field, inducing a torque in the magnetic moments, resulting in the generation of spin excitations. However, this inductive method is power-consuming due to ohmic losses. In addition, the discrepancy in wavelength between the excitation electromagnetic wave and the generated spin wave highly affects the amplitude of magnetization oscillation over longer distances. Furthermore, the intrinsic magnetic losses limit their propagation, and even in low-damping materials, such as $Y_3Fe_5O_{12}$ (YIG), the propagation length of spin waves is in the micrometer range [53], thereby limiting their potential applications.

To overcome these challenges, a promising approach is to couple spin waves with propagating surface acoustic waves (SAWs) via the magnetoelastic effect [54]. SAWs are elastic waves, which are quantized as phonons, that propagate on the surface of piezoelectric materials and can be excited using interdigital transducers (IDTs) [55]. SAW devices have become a standard technology in telecommunication systems, owing to their slow propagation velocity, which is five orders of magnitude less than electromagnetic waves, and their propagation lengths up to the millimeter range.

Therefore, the magnon-phonon interaction has been increasingly attracting interest since the last decade, from fundamental aspects of their hybridization [56–58], the transfer of spin angular momentum between the quasiparticles [59], for switching the magnetization state for memory device applications [60–63], up to the prospective of applying propagating SAWs to magnetoelastic films to excite spin dynamics [26, 64, 65] in a less power-consuming manner, as the voltage-driven IDT excitation avoids ohmic dissipations, more efficiently and with less attenuation.

The possibility of exciting spin dynamics in a magnetoelastic film from SAW propagation has been observed from IDT experiments, where the absorption in the transmitted signal can be linked to the acoustically-driven ferromagnetic resonance, mostly in Ni devices [25, 66–71], but also in other magnetoelastic metals [72] and in semiconductors [73, 74]. SAW-driven magnetization oscillations have also been imaged using magnetic-contrast techniques [75–77], which sheds light on the promising application of elastic waves in magnonic devices.

By exploiting the magnetoelastic coupling between the magnetic moments and the acoustic strain field, the SAWs can efficiently generate and detect spin waves in magnetic films [64, 77]. The magnetoelastic coupling is a two-way street: the spin waves, in turn, can couple with the SAWs, thus creating an efficient and tunable magnetoelastic interaction. This approach not only allows the possibility of the efficient excitation and detection of spin waves, but also provides a means of propagating them over longer distances with low losses.

Magnonics is a field that has gained significant attention in recent years, both for its fundamental aspects and potential technological applications. The interaction between magnons and phonons has emerged as a promising possibility for magnonics to become competitive with current information technology. In particular, the magnetoelastic interaction shows great potential for exciting spin dynamics in a less power-consuming manner, making it an attractive approach for memory devices and other applications. Therefore, further research is necessary to fully understand the fundamental aspects of the magnon-phonon interaction and its potential applications. Overall, the study of magnon-phonon interactions provides a promising avenue for advancing the field of magnonics and developing new technologies that could have significant impact in various fields.

## 1.2 Objectives

The objectives of this thesis are to perform finite-differences numerical simulations using the open-source software MuMax3 [78] to investigate the magnetization dynamics of ferromagnetic materials by solving the Landau-Lifshitz-Gilbert (LLG) equation. The main focus is to simulate the propagation of spin waves in materials that contain magnetoelastic interaction. First, we aim to study the effective magnetic field on nanostructures due to the excitation of elastic waves via the magnetoelastic effect. Another objective is to analyze the dispersion characteristics of the elastic and magnetic waves and their coupling and interconversion by solving the coupled LLG and elastodynamics equations, taking into account the magnetoelastic feedback. These simulations will be carried out under various geometries and external magnetic field configurations to study the effect of different parameters on the magnetic and magnetoelastic properties of the system.

Specifically, the main results of this thesis consist of three finite-difference numerical simulations. Firstly, an external elastic wave will propagate in the magnetoelastic material,

driving its spin dynamics, and we will calculate the spin modes that are elastically excited. The possibility of electrically measuring this effect will be evaluated by using the spin pumping phenomena associated with the inverse spin hall effect (ISHE). Secondly, we will solve the coupled LLG and elastodynamics in a stripe under a spatially varying magnetic field. The aim is to convert the excitation from the quasi-magnetic region to the quasi-elastic, utilizing the changes in the dispersion relation of the magnetoelastic interaction due to the magnetic field intensity, and obtaining a magnon-phonon conversion. Finally, we will study the propagation of magnetoelastic waves in a complex magnetic domain pattern, the Néel-type domain wall, in a thin film stripe. This simulation will calculate the elastic and magnetic eigenmodes and discuss the hybridization between these two modes based on their symmetry.

## 1.3 Overview of the thesis

This thesis is structured into five chapters. Chapter 1 is the introduction, providing a brief overview of the motivation and objectives of the research. Chapter 2 is dedicated to providing the theoretical background necessary to understand the simulations carried out in the subsequent chapters. This includes an overview of the micromagnetic model, magnetization dynamics, and a detailed discussion of resonant phenomena such as ferromagnetic resonance (FMR) and spin waves. Additionally, elastic waves, magnetoelastic interactions, and coupled magnetoelastic waves are described.

In Chapter 3, the numerical simulation methods used in the thesis are presented, along with an explanation of how the data were processed to obtain the results. This sets the stage for Chapter 4, which presents the results of the three main simulations in the thesis. The first simulation, section 4.1, involves the excitation of spin dynamics in a stripe through an external elastic excitation, simulating the excitation of a magnetoelastic field from a IDT on a piezoelectric substrate. Here, we have also calculated the ISHE voltage that could be measured in an adjacent metallic stripe. The second simulation, section 4.2, focuses on the conversion of magnons into phonons by using a spatially-varying magnetic field, taking advantage of the characteristics of the hybrid magnetoelastic dispersion relation. The third simulation, section 4.3, examines the elastic and magnetic wave modes that propagate in a Néel domain wall structure, with a discussion of the coupling between those modes based on their symmetry.

Finally, Chapter 5 presents the conclusions and perspectives of the thesis, summarizing the main findings and highlighting their significance. This chapter also identifies possible directions for future research in the field.

This thesis also included experimental work that was not fully completed, but the results are included in appendix A as a guide for future experiments. The experiments involved the deposition and characterization of piezoelectric thin film ZnO using electron microscopy and X-ray experiments, as well as the fabrication of interdigital transducers (IdTs) on a magnetic substrate YIG using electron beam lithography and laser lithography. The aim was to use the IdTs to excite surface acoustic waves (SAWs) to drive YIG magnetization dynamics and perform magnon-phonon experiments. Electric transport measurements in the IdTs and Brillouin light scattering experiments were also carried out.

# Chapter 2

# Theoretical Background

## 2.1 Magnetization dynamics

The physical properties of magnetic materials can be understood as the interaction between its microscopic magnetic moments and both external magnetic fields and each other. This interaction determines the magnetic behavior of the material, which includes its magnetic susceptibility, magnetic anisotropy, and magnetic hysteresis, among others. In this section, we will discuss the dynamics of the magnetization vector and the magnetic energy terms that determine its equilibrium position.

### 2.1.1 Landau-Lifshitz-Gilbert (LLG) equation

The magnetic moment of an atom or an ion $\vec{\mu}$ can be written as

$$\vec{\mu} = -g\mu_B \vec{J}, \tag{2.1}$$

where g is the spectroscopic splitting factor, $\mu_B$ is the Bohr magneton and $\vec{J}$ is its total angular momentum, including its orbital and spin components.

A magnetic moment $\vec{\mu}$ under a magnetic field induction $\vec{B}$ has energy $U = -\vec{\mu}\cdot\vec{B}$, which is minimum when they are parallel to each other. When deflected from $\vec{B}$ the magnetic moment becomes subject to a torque $\vec{\tau} = \vec{\mu} \times \vec{B}$. Considering its angular momentum $\hbar\vec{J}$

and Newton's second law, we obtain the equation of motion [79]

$$\frac{d\vec{\mu}}{dt} = -\gamma\vec{\mu} \times \vec{B}, \tag{2.2}$$

with $\gamma = g\mu_B/\hbar$ known as the gyromagnetic ratio.

In the macroscopic scale it is worth defining the magnetization vector $\vec{M}$ as the total magnetic moment of the sample per unit volume,

$$\vec{M} = \frac{1}{V}\sum_i \vec{\mu}_i. \tag{2.3}$$

This way, using the equation $\vec{B} = \mu_0(\vec{M} + \vec{H})$, where $\mu_0$ is the vacuum permeability and $\vec{H}$ the magnetic field intensity, we can obtain the Landau-Lifshitz equation,

$$\frac{d\vec{M}}{dt} = -\gamma\mu_0\vec{M} \times \vec{H}, \tag{2.4}$$

that describes the dynamics of the magnetization when subject to a magnetic field in the absence of damping.

When the magnetization is parallel to the magnetic field, the cross product is null and the derivative is zero, hence the magnetization is in the equilibrium position. If the magnetization is deflected from the magnetic field, the derivative becomes non-zero and an effective torque acts on the $\vec{M}$.

Let us consider that the magnetic field is in the z-direction, that is $\vec{H} = H\hat{z}$, and the magnetization is slightly deflected from that direction, $\vec{M} = m_x\hat{x} + m_y\hat{y} + M_z\hat{z}$ with $M_z \gg m_x, m_y$. From equation 2.4 we obtain

$$\frac{dm_x}{dt} = -\gamma\mu_0 m_y H \quad \text{and} \quad \frac{dm_y}{dt} = \gamma\mu_0 m_x H. \tag{2.5}$$

One solution for that system is

$$m_x(t) = m_0\cos(\omega_0 t) \quad \text{and} \quad m_y(t) = m_0\sin(\omega_0 t), \tag{2.6}$$

where $\omega_0 = \gamma\mu_0 H$. The magnetization components transverse to the magnetic field, $m_x$ and $m_y$, present a circular motion with constant amplitude, see Figure 2.1a. From that, we can see that the magnetization starts a precession motion around $\vec{H}$ with frequency $\omega_0$, which is the magnetic resonance frequency.

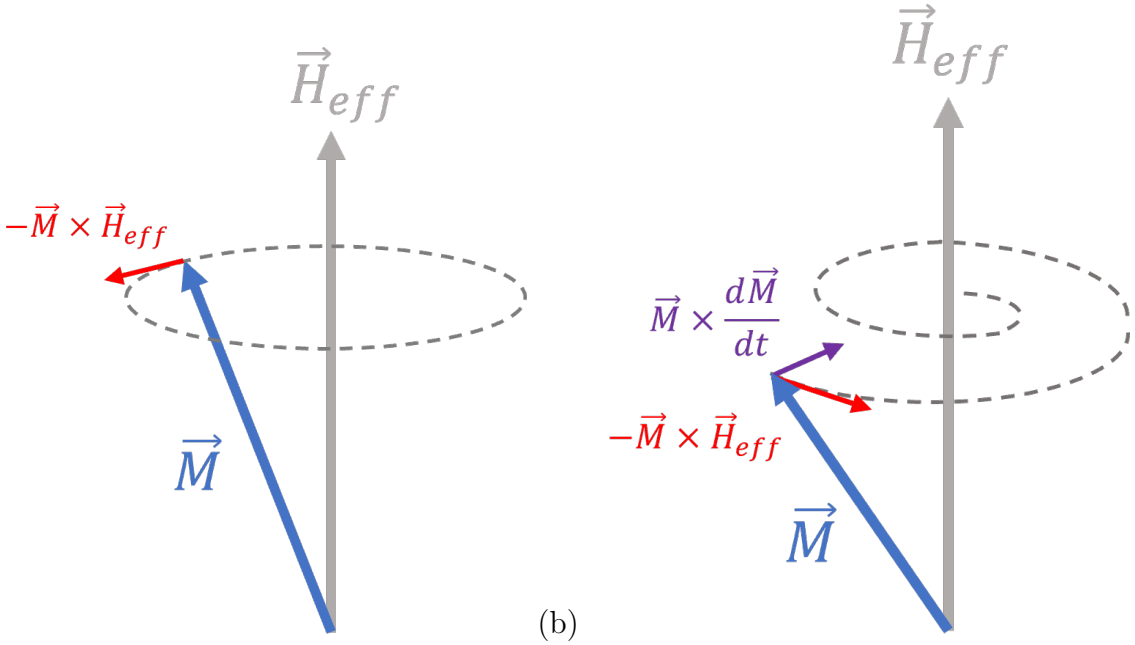


Figure 2.1: Schematic representation of the magnetization dynamics, as described by the Landau-Lifshitz-Gilbert equation. In (a), the magnetization undergoes a precession motion around the effective field direction in the absence of damping. In (b), the dynamics with damping is shown, resulting in a gradual reduction of the amplitude over time.

The magnetization, however, relaxes towards the equilibrium direction and the relaxation is driven by several atomic spin interactions. Regardless of the details of its underlying mechanisms, the phenomenon of relaxation can be incorporated into the dynamics through a phenomenological approach. This can be achieved by *ad hoc* inclusion of a damping term to the Landau-Lifshitz equation, the Gilbert damping, representing a torque that drives the magnetization towards its equilibrium direction. Then the Landau-Lifshitz-Gilbert (LLG) equation is

$$\frac{d\vec{M}}{dt} = -\gamma\mu_0 \vec{M} \times \vec{H} - \frac{\alpha}{M} \vec{M} \times \frac{d\vec{M}}{dt}, \tag{2.7}$$

where $\alpha$ is a phenomenological dimensionless quantity known as Gilbert damping parameter, see Figure 2.1b.

### 2.1.2 Magnetic energy terms

The equilibrium direction of the magnetization can be defined by an effective field $\vec{H}_{eff}$, which is obtained from the sum of all magnetic interaction energies, as $\delta E = -\mu_0 \delta \vec{M} \cdot \vec{H}_{eff}$, thus,

$$\vec{H}_{eff} = -\frac{1}{\mu_0} \nabla_{\vec{M}} E, \tag{2.8}$$

where $\nabla_{\vec{M}}$ is the gradient operator relative to the magnetization components, and E is the total magnetic energy per volume. In ferro- and ferrimagnetic materials the effective field includes several terms, as the exchange interaction, the dipolar field, the Zeeman energy and the magnetocrystalline anisotropy.

The **Zeeman energy** is the interaction between the spins with an external magnetic field $H_0$, with energy density

$$E_Z = -\mu_0 \vec{M} \cdot \vec{H}_0, \tag{2.9}$$

which is minimum when the magnetization is aligned with the external field.

The **dipolar** or **magnetostatic field** $\vec{H}_d$ is the magnetic field created by the magnetization itself. Inside the magnetic material it opposes the magnetization, and is known as demagnetizing field, and outside the material it is called the stray field.

We can evaluate the dipolar field from Maxwell's equation that

$$\nabla \cdot \vec{B} = \mu_0 \nabla \cdot (\vec{H}_d + \vec{M}) = 0, \tag{2.10}$$

and, if we consider the magnetostatic limit ($\nabla \times \vec{H}_d = 0$), it allows the definition of a magnetic scalar potential,

$$\vec{H}_d = -\nabla \phi. \tag{2.11}$$

Combining these equations we obtain a magnetic Poisson equation,

$$\nabla^2 \phi = \nabla \cdot \vec{M}. \tag{2.12}$$

where it can be seen that the dipolar field arises from the divergence of the magnetization, known as magnetic charges.

A general expression for the demagnetizing field can be obtained from the magnetic Poisson equation as [80].

$$\vec{H}_d = \frac{1}{4\pi} \int_V' \widetilde{D}(\vec{r} - \vec{r'}) \vec{M}(\vec{r'}) dV', \tag{2.13}$$

where V' is the sample volume and $\widetilde{D}$, given by the equation,

$$\widetilde{D}(\vec{r}-\vec{r'}) = \nabla_{\vec{r}}\nabla_{\vec{r'}}\frac{1}{|\vec{r}-\vec{r'}|}, \tag{2.14}$$

is the tensorial magnetostatic Green's function.

By choosing the Cartesian coordinates as the symmetry axes of the sample, the tensor becomes diagonal, and it satisfies $N_x + N_y + N_z = 1$. In this case, we can readily obtain the demagnetizing factor for simple geometries. For a spherical sample, the symmetry implies that $N_x = N_y = N_z = 1/3$. For a thin film in the xy-plane, the poles in x and y are widely separated, resulting in no surface charges in those directions, hence $N_x = N_y = 0$, and consequently, $N_z = 1$ perpendicular to the plane. Similarly to an infinite cylinder placed along the y-direction, it has no surface changes along its length, $N_y = 0$, and is symmetric in x and z thus $N_x = N_z = 1/2$. These results are summarized in Figure 2.2.

In the case of a sample with uniform magnetization, the demagnetizing field is solely produced by surface charges and the demagnetizing field can be simplified to [79]

$$\vec{H}_d = -\widetilde{N} \cdot \vec{M} \tag{2.15}$$

where $\widetilde{N}$ is the demagnetizing tensor, which only depends on the shape of the sample, hence the dipolar interaction is also known as shape anisotropy.

The **exchange energy** arises from the interaction between neighbouring spins due to the overlap of their orbital wave functions. From the Pauli exclusion principle, the total wave function with both orbital and spin components must be antisymmetric. If the spins are parallel, the orbital wave function, which represents the charge distribution, must be antisymmetric in space, while if the spins are antiparallel, the orbital wave function becomes symmetric. The exchange energy reflects the difference in energy between the two relative orientation of the spins [79].

The exchange energy between the two spins $\vec{S}_i$ and $\vec{S}_j$, below the Curie temperature $T_C$, can be described by the Heisenberg energy,

$$E_{ex} = -2J\vec{S}_i \cdot \vec{S}_j, \tag{2.16}$$

where J is the exchange constant. For $J > 0$, the state with the lowest energy is achieved when neighboring spins are parallel, which is a characteristic of ferromagnetic materials

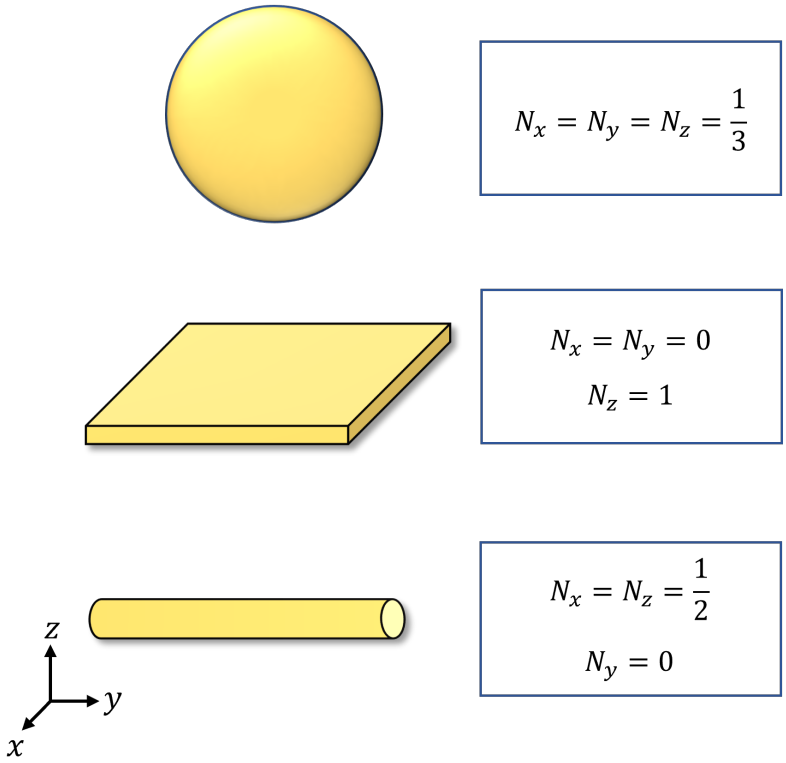


Figure 2.2: Demagnetizing tensor components for simple geometries, respectively, a sphere, an infinite film and an infinitely long cylinder.

and for $J < 0$, the minimum energy state is obtained when the spins are antiparallel, a property seen in both ferri- and antiferromagnets, see Figure 2.3.

For distances much larger than the atomic dimensions, we can introduce a continuous approximation for $\vec{M}$ and derive the total exchange energy density of a sample as

$$E_{ex} = \frac{A_{ex}}{M_s^2}(\nabla \vec{M})^2, \tag{2.17}$$

where $A_{ex}$ is the exchange stiffness of the sample and the corresponding exchange field is

$$\vec{H}_{ex} = \frac{2A_{ex}}{\mu_0 M_s^2}\nabla^2 \vec{M} = l_{ex}^2 \nabla^2 \vec{M}, \tag{2.18}$$

where $l_{ex}$ is called the exchange length, typically in the order of nm.

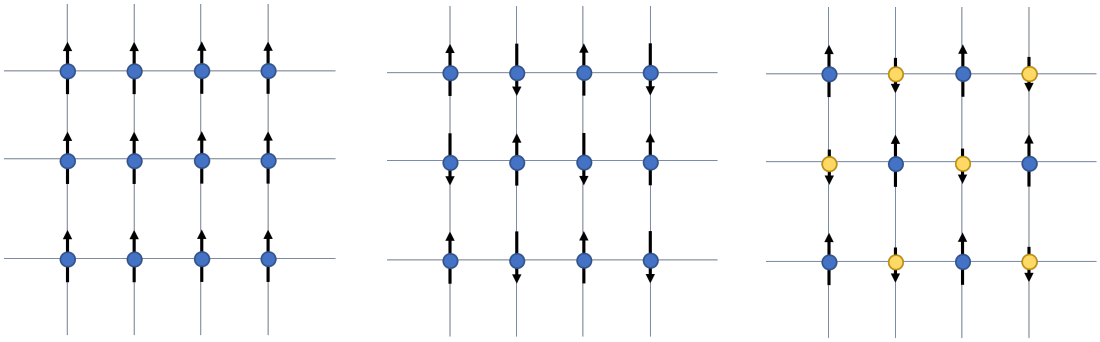


Figure 2.3: Spins equilibrium position due to the exchange interaction in different magnetic materials. In panel (a), a ferromagnetic material is presented where the spins are parallel to each other. Panel (b) shows an antiferromagnetic material where the spins are antiparallel. Similarly, panel (c) shows a ferrimagnetic material, but unlike the antiferromagnetic case, the opposite spins do not cancel each other, leading to a net magnetic moment in the ferrimagnetic material.

In ferromagnetic materials, the exchange interaction tries to keep the magnetic moments parallel. The exchange length defines the competition between the dipolar and exchange interactions. On length scales smaller than the exchange length, the exchange interaction dominates and the magnetization is uniform. On length scales larger than $l_{ex}$, the dipolar interaction becomes increasingly important, allowing for the formation of magnetic domains.

The **magnetocrystalline anisotropy energy** arises from the interaction between the magnetic momenta and the crystal structure of the material from the spin-orbit coupling. Therefore, the minimum energy state is obtained when the magnetization is parallel to a preferred orientation of the crystal structure. A phenomenological representation of the anisotropy energy can be used to study its effect on the magnetization dynamics.

In a crystal with uniaxial symmetry, the magnetocrystalline anisotropy energy can be expressed as the power series

$$E_u = -K_{u1}cos^2\theta - K_{u2}cos^4\theta, \tag{2.19}$$

where $K_{u1}$ and $K_{u2}$ are the first and second order uniaxial anisotropy constants and $\theta$

is the angle between the symmetry axis and the magnetization. Only even powers of the cosine are present as the anisotropy energy does not change with the inversion of the magnetization. When $K_{u1}$ and $K_{u2}$ are both positive, the minimum energy is achieved when the magnetization is aligned with the symmetry axis, called the easy axis. Yet, if they are both negative, the minimum energy is achieved with the magnetization perpendicular to the symmetry axis, defining an easy plane for the magnetization.

Now, for a crystal with cubic symmetry, multiple equivalent directions exist, requiring the use of several angles. The orientation of the magnetization with respect to the crystal axes can be expressed using the direction cosines $\alpha_1$, $\alpha_2$, and $\alpha_3$. Again the inversion symmetry results in only even powers being present and, due to the cubic symmetry, the energy must be invariant under interchange of $\alpha_i$ values. The cubic energy density can be written as

$$E_c = K_{c1}(\alpha_1^2\alpha_2^2 + \alpha_2^2\alpha_3^2 + \alpha_3^2\alpha_1^2) + K_{c2}\alpha_1^2\alpha_2^2\alpha_3^2, \tag{2.20}$$

where $K_{c1}$ and $K_{c2}$ are the first and second order cubic anisotropy constants. It can be shown that for energy minimization, the easy and hard axes of the magnetization are along the principal symmetry axes of the crystal [79].

In conclusion, the magnetization dynamics of magnetic materials can be understood by considering the interplay of several key magnetic free energy terms. The Zeemann energy accounts for the interaction of the magnetic moment with an external magnetic field. In a ferromagnetic material, the exchange interaction drives the alignment of individual magnetic moments parallel, while the magnetostatic interaction takes into account the interaction between magnetic moments due to their spatial arrangement. Finally, the magnetocrystalline anisotropy represents the energy associated with the preferred orientation of magnetic moments with respect to the crystal symmetry.

## 2.2 Ferromagnetic Resonance (FMR)

In this section, we will discuss the ferromagnetic resonance (FMR), which is a phenomenon that occurs in ferromagnetic materials when subjected to an alternating magnetic field. It involves the uniform resonant excitation of magnetic moments within the whole material. The frequency of the magnetic field at which this resonance occurs is known as the ferromagnetic resonance frequency, and is dependent on various material parameters such as the shape of the sample, the magnetic anisotropy, and the strength of the magnetic field.

### 2.2.1 Magnetic resonance driven by alternating field

We now want to explore the dynamic behaviour of the magnetization. Let us start with a material with negligible interaction between spins, e.g. a paramagnet. For this, consider a magnetic material that is subject to both a static magnetic field in the z-direction and a dynamic alternating field in the xy-plane with frequency $\omega$,

$$\vec{H} = (h_x\hat{x} + h_y\hat{y})e^{-i\omega t} + H_0\hat{z}, \tag{2.21}$$

with $H_0 \gg h_x, h_y$. Again, the magnetization is in the form of

$$\vec{M} = m_x\hat{x} + m_y\hat{y} + M_z\hat{z} \tag{2.22}$$

with $M_z \gg m_x, m_y$. In the absence of damping, using equation 2.4, we obtain

$$\frac{dm_x}{dt} = -\gamma\mu_0 m_y H_0 + \gamma\mu_0 M_z h_y e^{-i\omega t}, \tag{2.23}$$

$$\frac{dm_y}{dt} = \gamma\mu_0 m_x H_0 - \gamma\mu_0 M_z h_x e^{-i\omega t}. \tag{2.24}$$

Those equations can be linearized when looking at steady-state solutions, that is $m_x(t) = m_x e^{-i\omega t}$ and $m_y(t) = m_y e^{-i\omega t}$. Considering $\omega_0 = \gamma\mu_0 H_0$ we obtain

$$-i\omega m_x = -\omega_0 m_y + \gamma\mu_0 M_z h_y, \tag{2.25}$$

$$-i\omega m_y = \omega_0 m_x - \gamma\mu_0 M_z h_x. \tag{2.26}$$

Now, solving for $m_x$ and $m_y$, considering $M_z \approx M$ and $\omega_M = \gamma\mu_0 M$, we obtain

$$m_x = \frac{\omega_M\omega_0}{\omega_0^2 - \omega^2}h_x - i\frac{\omega_M\omega}{\omega_0^2 - \omega^2}h_y, \tag{2.27}$$

$$m_y = i\frac{\omega_M\omega}{\omega_0^2 - \omega^2}h_x + \frac{\omega_M\omega_0}{\omega_0^2 - \omega^2}h_y. \tag{2.28}$$

Note that when the rf-field is applied in any direction, the magnetization components in both the x and y directions are produced due to the precession around the z-axis with frequency $\omega$. The precession reaches its resonance frequency at $\omega = \omega_0$ and its amplitude diverges in that frequency in the absence of damping.

### 2.2.2 Magnetic resonance in ferromagnets

Now, to expand the analysis to a ferro- or ferrimagnetic material we shall include the exchange and dipolar interactions. In the uniform precession mode, the magnetization does not vary across the space and all spins can be considered as being parallel. So, as the exchange effective field is dependent on the divergence of $\vec{M}$, see equation 2.18, it is null for this uniform mode and does not affect its resonance frequency. It is important to highlight that the exchange interaction strongly affects the non-uniform ($k \neq 0$) precession modes, the spin waves, which will be treated in the next section.

The dipolar interaction, however, strongly alters the resonance frequencies. Let us consider a sample with simple geometry, an ellipsoidal shape, which has an uniform demagnetizing field, equation 2.15, under an static external field $\vec{H}_0$. The total internal field is

$$\vec{H}_{int} = \vec{H}_0 - \widetilde{N} \cdot \vec{M}. \tag{2.29}$$

Considering that the x, y and z directions are along the symmetry axes of the tensor, and the external field is in the z-direction, the internal field can be written as

$$\vec{H}_{int} = N_x m_x \hat{x} - N_y m_y \hat{y} + (H_0 - N_z M_z)\hat{z}, \tag{2.30}$$

where $m_x, m_y \ll M_z \approx M$. Using the Landau-Lifshitz equation, equation 2.4, the magnetization equations become

$$\frac{dm_x}{dt} = -\gamma\mu_0 m_y [H_0 + (N_y - N_z)M], \tag{2.31}$$

$$\frac{dm_y}{dt} = \gamma\mu_0 m_x [H_0 + (N_x - N_z)M]. \tag{2.32}$$

These equations have the same solution as equations 2.6 but with resonant frequency

$$\omega_0 = \gamma\mu_0 \sqrt{[H_0 + (N_x - N_z)M][H_0 + (N_y - N_z)M]}, \tag{2.33}$$

which is known as Kittel formula for the ferromagnetic resonance (FMR), and it determines the frequency of uniform precession mode for a ferromagnetic material as a function of the external field intensity $H_0$. For simple geometries the demagnetizing factors can be easily obtained, and the FMR equation, for example, for a sphere ($N_x = N_y = N_z = 1/3$) becomes

$$\omega_0 = \gamma\mu_0 H_0, \tag{2.34}$$

and for a thin film ($N_x = N_y = 0$ and $N_z = 1$) is

$$\omega_0 = \gamma\mu_0\sqrt{H_0(H_0 + M)}. \tag{2.35}$$

Finally, let us now consider the effect of the damping in the equations. Assuming, for the sake of simplicity, an uniform magnetization in an infinite sample, where the magnetostatic field is negligible, that is subjected to an external field $H_0\hat{z}$.

Using $\vec{M} = m_x\hat{x} + m_y\hat{y} + M\hat{z}$, now in the LLG equation, equation 2.7, we obtain, after considering $m_x(t) = m_x e^{-i\omega t}$ and $m_y(t) = m_y e^{-i\omega t}$ the equations

$$-i\omega m_x = (-\omega_0 + i\alpha\omega)m_y, \tag{2.36}$$

$$-i\omega m_y = (\omega_0 - i\alpha\omega)m_x, \tag{2.37}$$

with $\omega_0 = \gamma\mu_0 H_0$. A solution for this system is $m_x = im_y$ and $\omega = \omega_0 - i\alpha\omega$, thus the magnetization also precesses around the equilibrium position, but the amplitude of the transverse components decay exponentially in time with the factor $e^{-\alpha\omega t}$.

We can write these solutions in the tensorial form

$$\vec{m} = \widetilde{\chi}\vec{h}, \tag{2.38}$$

where the vectors $\vec{m}$ and $\vec{h}$ are the dynamic components of the magnetization and of the external field,

$$\vec{m} = \begin{bmatrix} m_x \\ m_y \end{bmatrix} \quad \text{and} \quad \vec{h} = \begin{bmatrix} h_y \\ h_y \end{bmatrix}, \tag{2.39}$$

and $\widetilde{\chi}$ is the magnetic susceptibility tensor,

$$\widetilde{\chi} = \begin{bmatrix} \chi_{xx} & \chi_{xy} \\ \chi_{yx} & \chi_{yy} \end{bmatrix}. \tag{2.40}$$

Considering a small damping, $\alpha\omega \ll \omega_0$, the susceptibility tensor components become

$$\chi_{xx}(\omega) = \chi_{yy}(\omega) = \frac{\omega_M\omega_0}{\omega_0^2 - \omega^2 - 2i\omega_0\alpha\omega}, \tag{2.41}$$

$$\chi_{yx} = -\chi_{xy} = i\frac{\omega_M\omega}{\omega_0^2 - \omega^2 - 2i\omega_0\alpha\omega}. \tag{2.42}$$

Observe that now, when $\omega = \omega_0$, the amplitude of $\vec{m}$ does not diverge with time. Near the resonance $\omega \approx \omega_0$, we can obtain separate the diagonal components in its real and imaginary parts as

$$Re[\chi_{xx}] = \frac{\omega_M(\omega_0 - \omega)/2}{(\omega_0 - \omega)^2 + \alpha^2\omega^2}, \tag{2.43}$$

$$Im[\chi_{xx}] = \frac{(\omega_M\alpha\omega)/2}{(\omega_0 - \omega)^2 + \alpha^2\omega^2}, \tag{2.44}$$

see Figure 2.4. From these equations, as the imaginary part takes the form of a Lorentzian function, it can be used experimentally to determine the damping characteristics of the sample from its full width at half maximum (FWHM), $2\Delta H$, using the relation

$$\Delta H = \alpha\omega_0/\gamma. \tag{2.45}$$

Determining the FWHM in experiments provides important information about the damping of the magnetic resonance, thus it is a critical parameter for understanding the energy dissipation mechanisms in magnetic materials. Additionally, the FWHM can provide insights into the magnetic properties of the material, such as the magnetic anisotropy, the magnetic domain size, and the magnetocrystalline anisotropy.

### 2.2.3 Spin pumping and inverse spin Hall effect (ISHE)

The conversion of spin current to electrical charge current is an interesting phenomenon for spintronics devices, and in this section, we will discuss the detection of FMR via the spin pumping phenomenon coupled to the inverse spin Hall effect (ISHE).

Specifically, the magnetization dynamics of a ferromagnet can generate a spin current in an adjacent non-magnetic material through the spin pumping phenomenon, and this spin current can be converted to a charge current, and thus, to an electric voltage difference, through the ISHE [81], see Figure 2.5.

The detection of magnetic excitations such as FMR or spin waves through voltage measurements can be a more accessible option for experimentalists compared to other techniques such as Brillouin light scattering, time-dependent magneto-optical or X-ray absorption measurements. With this in mind, we will now explore the generation of spin currents and their subsequent conversion to charge currents.

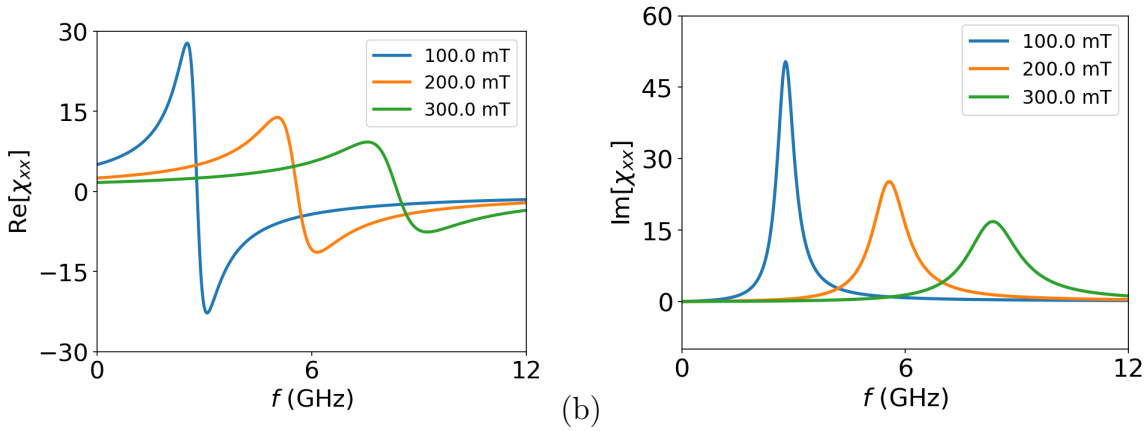


Figure 2.4: (a) Real and (b) imaginary parts of magnetic susceptibility as a function of the frequency for different external magnetic field intensities calculated from equations 2.43 and 2.44 for a 14 nm Permalloy thin film ($M_s = 800kA/m$ and $A_{ex} = 13pJ/m$).The imaginary part exhibits a Lorentzian curve with a peak at the FMR frequency, and the damping of the material can be calculated from its width at half maximum.

Considering a ferromagnetic/non-magnetic (FM/NM) thin film bilayer, in the xy-plane, with the interface being at $z = 0$. The dynamics of the magnetic layer ($\vec{m}$) generates a spin current $J_s$ (in units of angular momentum / (area $\cdot$ time)) across the FM/NM interface, given by [82, 83],

$$\vec{J}_s(z=0) = \frac{\hbar g_{eff}^{\uparrow\downarrow}}{4\pi}\left(\vec{m} \times \frac{\partial \vec{m}}{\partial t}\right), \tag{2.46}$$

where $g_{eff}^{\uparrow\downarrow}$ is the real part of the effective spin mixing conductance, which is a parameter that characterizes the strength of the spin transfer. It is a measure of the efficiency with which the spin angular momentum of the ferromagnet is transferred to the non-magnetic material.

It is important to highlight that equation 2.46 does not completely describe the spin current, which presents a tensorial nature [84]. It requires one index for its transport direction ($\hat{z}$ in this case) and a second one for the spin current polarization direction ($\vec{\sigma}$). Only the last is being represented in the vectorial notation of Equation 2.46 and it is implicit that $\vec{J}_s = J_s(\vec{\sigma})\ \hat{z}$.

We will now consider that the equilibrium magnetization is in the film plane, at an

arbitrary direction $\hat{u}$, where the versors $\hat{u}$ and $\hat{v}$ are obtained from a rotation of $\hat{x}$ and $\hat{y}$ by $\theta$ about the $z$ axis. Under excitation, the magnetization goes in a simple precessional motion, $\vec{m} = m_u\hat{u} + m_{0v}cos(\omega t)\hat{v} + m_{0z}sin(\omega t)\hat{z}$, with a small amplitude ($m_{0v}$,$m_{0z} \ll m_u$).

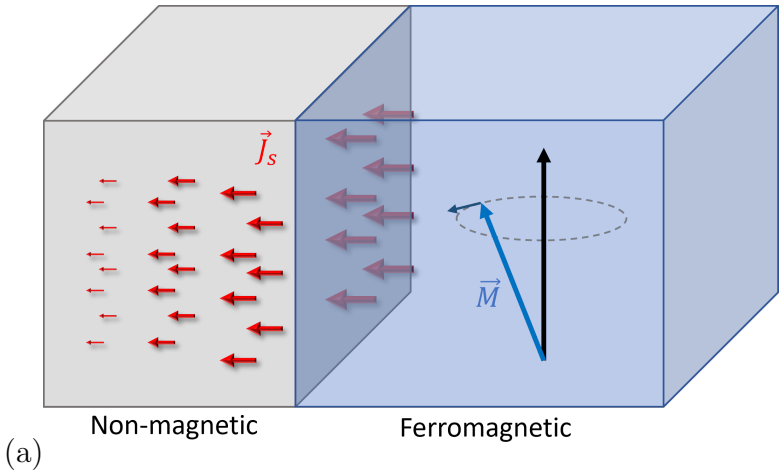


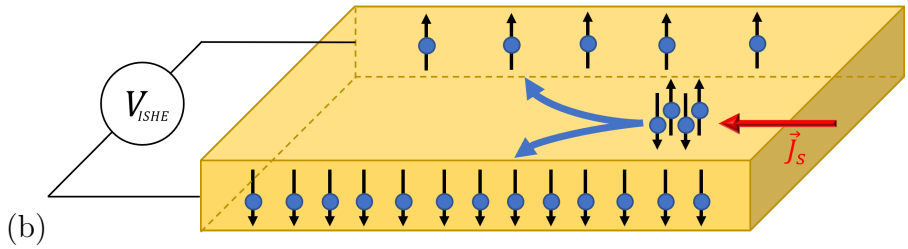


Figure 2.5: The figure illustrates (a) spin pumping and (b) the inverse spin hall effects (ISHE). The magnetization dynamics of a ferromagnet can induce a spin current in a neighboring non-magnetic material through the spin pumping phenomenon, as shown in (a). On the other hand, in a non-magnetic material with strong spin-orbit coupling, spins with opposite orientation are deflected to opposite directions, which is known as the ISHE, as depicted in (b). When the incoming current is spin polarized, the spin accumulation in the opposite directions will not be equal, and this will result in a potential difference between them, leading to the ISHE voltage ($V_{ISHE}$).

We can estimate the equilibrium component as approximately constant ($m_u \approx m_{0u}$), and one obtains $\partial\vec{m}/\partial t = -\omega m_{0v}sin(\omega t)\hat{v} + \omega m_{0z}cos(\omega t)\hat{z}$, and, from Equation 2.46, we

obtain,

$$\begin{cases} J_s^{z=0}(\sigma_u) = (\hbar\omega g_{eff}^{\uparrow\downarrow}/4\pi) m_{0v} m_{0z}, \\ J_s^{z=0}(\sigma_v) = (\hbar\omega g_{eff}^{\uparrow\downarrow}/4\pi) m_{0u} m_{0z} cos(\omega t), \\ J_s^{z=0}(\sigma_z) = (\hbar\omega g_{eff}^{\uparrow\downarrow}/4\pi) m_{0u} m_{0v} sin(\omega t), \end{cases} \tag{2.47}$$

where $J_s^{z=0}(\sigma_i)$ is the spin current that flows across the FM/NM interface ($uv$-plane, z=0) with spin current polarization in the $i$-direction.

The spin current undergoes relaxation and diffusion into the non-magnetic material, so the spin current at a distance $z$ from the interface becomes [81, 85]:

$$\vec{J}_s(z) = J_s^{z=0}(\vec{\sigma}) \frac{sinh[(z - t_N)/\lambda_{SD}]}{sinh(t_N/\lambda_{SD})} \hat{z}, \tag{2.48}$$

where $\lambda_{SD}$ is the spin diffusion length in the non-magnetic material and $t_N$ is its thickness.

The spin current can then be converted to electrical current through the Inverse Spin Hall Effect (ISHE) [86, 87] or through the Inverse Edelstein Effect (IEE) [88, 89]. So, due to ISHE, the spin current induces a charge current ($\vec{J}_c$) into the non-magnetic material, that is described by [85, 90]

$$\vec{J}_c = \theta_{SH} \frac{2e}{\hbar} [J_S \hat{z} \times \vec{\sigma}], \tag{2.49}$$

$$\vec{J}_c(z) = \left( \theta_{SH} \frac{e g_{eff}^{\uparrow\downarrow}}{2\pi} \right) \frac{sinh[(z - t_N)/\lambda_{SD}]}{sinh(t_N/\lambda_{SD})} \Big[ - m_{0u} m_{0z} cos(\omega t) \hat{u} + m_{0v} m_{oz} \hat{v} \Big]. \tag{2.50}$$

The charge current is given as a potential difference $\Delta V_{ISHE}$ between two contact pads placed along an arbitrary direction $\hat{\ell}$ on the non-magnetic layer surface. The voltage difference can be calculated as $\Delta V_{ISHE} = R_\ell \int \vec{J}_C \cdot d\vec{A}$, where $R_\ell$ is the resistance across the pads and A is the area of its cross-section. Considering $\ell$ the distance between pads, W their width, and $t_N$ and $\sigma_N$ the non-magnetic material thickness and conductivity, respectively, then $R_\ell = \ell/(\sigma_N W)$ and $\vec{A} = W t_N \hat{\ell}$, resulting in

$$\Delta V_{ISHE} = \frac{\ell}{\sigma_N t_N} \int_{z=0}^{z=t_N} (\vec{J}_C \cdot \hat{\ell}) dz, \tag{2.51}$$

$$\Delta V_{ISHE} = \frac{\lambda_{SD}\ell}{\sigma_N t_N} tanh\left(\frac{t_N}{2\lambda_{SD}}\right)(\vec{J}_C^{z=0} \cdot \hat{\ell}). \tag{2.52}$$

Thus, two components of the charge current are obtained: one in the $\hat{u}$ direction, with constant amplitude, called $J_C^{DC}$, and another in the $\hat{v}$ direction that oscillates with frequency $\omega$, called $J_C^{AC}$ [91]. To maximize the strength, the natural choice for the direction of the contact pads, are either $\hat{\ell} = \hat{u}$ or $\hat{\ell} = \hat{v}$, and from Equation 2.52 one obtains the AC and a DC component of the potential difference:

$$\Delta V_{\hat{\ell}=\hat{u}}^{AC} = \theta_{SH}\frac{e\ell\lambda_{SD}\omega g_{eff}^{\uparrow\downarrow}}{2\pi\sigma_N t_N} tanh\left(\frac{t_N}{2\lambda_{SD}}\right) m_{0u} m_{0z} cos(\omega t). \tag{2.53}$$

$$\Delta V_{\hat{\ell}=\hat{v}}^{DC} = \theta_{SH}\frac{e\ell\lambda_{SD}\omega g_{eff}^{\uparrow\downarrow}}{2\pi\sigma_N t_N} tanh\left(\frac{t_N}{2\lambda_{SD}}\right) m_{0v} m_{0z}, \tag{2.54}$$

It is worth noting that the DC voltage component is maximum when the line between contact pads is perpendicular to the magnetization direction. On the other hand, the AC component is maximum when the contact pads are aligned parallel to the magnetization direction.

## 2.3 Spin waves

In the previous section, we have considered the uniform motion of magnetization (k=0) along the entire sample, the ferromagnetic resonance (FMR). Now, we will expand to a more general situation, in which the magnetization displays a spatially-varying dynamics, the spin waves.

### 2.3.1 Linear chain of classical spins

Let us start with the simplest case of spin waves, a linear chain of evenly spaced classical spins. Consider a chain with N spins S, separated by a distance $a$, coupled to the near

neighbours through the exchange interaction. Considering the Heisenberg interaction we obtain the energy

$$U_{ex} = -2J \sum_i \vec{S}_i \cdot \vec{S}_{i+1}, \tag{2.55}$$

where $\vec{S}_i$ is the classical spin at the position $x_i = ia$. In the ground state, all spins are parallel to each other, and the total exchange energy is $U_0 = -2JNS^2$.

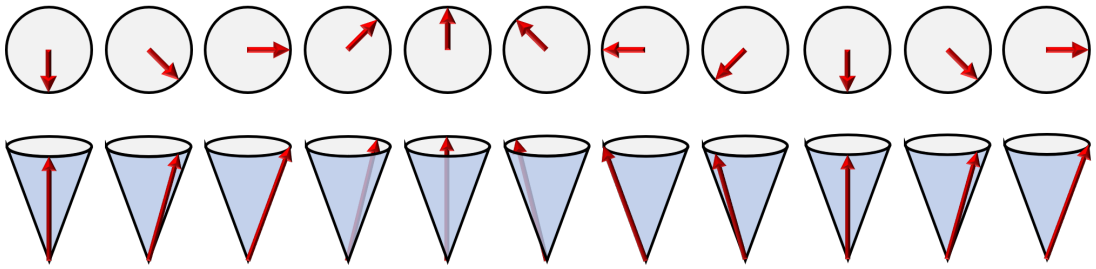

Figure 2.6: A schematic representation of a spin wave in a linear chain of spins coupled by the exchange interaction. As the spins precess, they present a phase difference that results in the formation of a spin wave with a constant wavevector.

The effective field corresponding to the Heisenberg interaction can be written as

$$\vec{H}_{ex} = -\frac{2J}{g\mu_B\mu_0}(\vec{S}_{i-1} + \vec{S}_{i+1}). \tag{2.56}$$

Considering that, besides the exchange field, the spins are also subject to an external field $H_0$, using the torque equation $\vec{\tau} = \hbar d\vec{S}/dt$, we obtain the equation of motion

$$\frac{d\vec{S}_i}{dt} = \gamma\mu_0 \vec{S}_i \times (\vec{H}_0 + \vec{H}_{ex}). \tag{2.57}$$

Considering that the external field is $\vec{H}_0 = -H_0\hat{z}$, and that $S_i^x, S_i^y \ll S_i^z \approx S$, we obtain the equations

$$\frac{dS_i^x}{dt} = \gamma\mu_0 H_0 S_i^y + \frac{2JS}{\hbar}(2S_i^y - S_{i-1}^y - S_{i+1}^y), \tag{2.58}$$

$$\frac{dS_i^y}{dt} = -\gamma\mu_0 H_0 S_i^x - \frac{2JS}{\hbar}(2S_i^x - S_{i-1}^x - S_{i+1}^x), \tag{2.59}$$

which show that the motion of any spin is coupled to its neighbours motion, and thus these are collective excitations. Now, looking for wave-like solutions in the form of $S_i^x = A_x e^{i(kx_i - \omega t)}$ and $S_i^y = A_y e^{i(kx_i - \omega t)}$, we are able to linearize the equations in the form

$$-i\omega A_x = A_y[\gamma\mu_0 H_0 + \frac{4JS}{\hbar}(1 - \cos ka)], \tag{2.60}$$

$$-i\omega A_y = -A_x[\gamma\mu_0 H_0 + \frac{4JS}{\hbar}(1 - \cos ka)]. \tag{2.61}$$

We can find a solution to the system as

$$\omega_k = \gamma\mu_0 H_0 + \frac{4JS}{\hbar}(1 - \cos ka), \tag{2.62}$$

known as the dispersion relation, that is it relates the spin wave frequency to its wave number. Besides, we can also obtain that $A_y = -iA_x$, and thus, the real parts of the dynamic components of the spins become $S_i^x = A_x \cos(kx_i - \omega_k t)$ and $S_i^y = A_x \sin(kx_i - \omega_k t)$. This corresponds to the spins precessing in a circular motion around the equilibrium position, but this time there is a phase difference between adjacent spins, $\phi_i = kx_i$, generating a wavelength $\lambda = 2\pi/k$.

From equation 2.62, we can see that for the FMR (k=0), we obtain $\omega = \gamma\mu_0 H_0$ as seen in the last section. And, in the limit of small wave numbers, $ka \ll 1$, which is a typical case in experiments, using binomial expansion we obtain

$$\omega_k = \gamma\mu_0 H_0 + \frac{2JSa^2}{\hbar}k^2, \tag{2.63}$$

a quadratic dispersion relation with an energy gap of $E = \hbar\gamma\mu_0 H_0$.

### 2.3.2 Spin waves in a bulk ferromagnet

Now we will consider a 3-dimensional ferromagnetic material, under an external field $\vec{H}_0 = H_0\hat{z}$. We will be looking for wave-like solutions described by weak perturbations from the equilibrium magnetization, $\vec{M} = \vec{M}_0 + \vec{m}(\vec{r}, t)$ in the form of

$$\vec{M}(\vec{r}, t) = m_x e^{i(\omega t + \vec{k}\cdot\vec{r})}\hat{x} + m_y e^{i(\omega t + \vec{k}\cdot\vec{r})}\hat{y} + M_z\hat{z}, \tag{2.64}$$

where $m_x, m_y \ll M_z \approx M_0$. Let us now include the exchange and dipolar energies in the effective field. We can readily obtain the exchange field from equation 2.18 as

$$\vec{h}_{ex} = -l_{ex}^2 k^2 \vec{m}, \tag{2.65}$$

which depends only on the dynamic components of the magnetization, as expected.

The dipolar field presents two terms, one arising from the sample shape, which is null in the case of an infinite bulk material, and a dynamic one coming from the spatially-variant magnetization dynamics. This second can be quite complex to calculate from equation 2.13 in a general nonuniform magnetization. This can be simplified for simple harmonic travelling spin waves.

Considering the magnetic field is in the form of $\vec{H} = H_0\hat{z} + \vec{h}_{dip}(\vec{r}, t)$, from Maxwell's equations we obtain

$$\nabla \cdot (\vec{h}_{dip} + \vec{m}) = 0 \quad \text{and} \quad \nabla \times \vec{h}_{dip} = 0. \tag{2.66}$$

Substituting the harmonic travelling magnetization, we get

$$\vec{k} \cdot (\vec{h}_{dip} + \vec{m}) = 0 \quad \text{and} \quad \vec{k} \times \vec{h}_{dip} = 0. \tag{2.67}$$

This way, after some manipulations using vector identities, we obtain the relation

$$\vec{h}_{dip} = -\frac{\vec{k} \cdot \vec{m}}{k^2}\vec{k}, \tag{2.68}$$

which is the volume dipolar field created by the travelling harmonic spin wave.

We can now use the axial symmetry of the bulk uniform material around the magnetization vector to choose a coordinate system where the wavevector $\vec{k}$ is in the xz-plane, that is $\vec{k} = k(sin\theta\hat{x} + cos\theta\hat{z})$, where $\theta$ is the angle between the magnetization and the propagation direction. This way, the dipolar field becomes

$$\vec{h}_{dip} = -\frac{k_x^2}{k^2} m_x = -m_x sin^2\theta\hat{x}. \tag{2.69}$$

By solving the LLG equation, equation 2.7 without the damping term, we obtain

$$\frac{d(\vec{M}_0 + \vec{m})}{dt} = -\gamma\mu_0[(\vec{M}_0 + \vec{m}) \times (\vec{H}_0 + \vec{h}_{dip} + \vec{h}_{ex})], \tag{2.70}$$

and, after linearization using the steady-state solutions we obtain the two coupled equations:

$$[\omega_0 + \omega_M(l_{ex}^2 k^2 + sin^2\theta)]m_x - i\omega m_y = 0, \tag{2.71}$$

$$i\omega m_x + (\omega_0 + \omega_M l_{ex}^2 k^2)m_y = 0, \tag{2.72}$$

where $\omega_0 = \gamma\mu_0 H_0$ and $\omega_M = \gamma\mu_0 M_s$.

Finally, from the non-trivial eigenvalues of the previous equations, we can obtain the spin wave dispersion relation for a bulk material, called the Herring-Kittel equation,

$$\omega_k = \sqrt{(\omega_0 + \omega_M l_{ex}^2 k^2)[\omega_0 + \omega_M(l_{ex}^2 k^2 + sin^2\theta)]}. \tag{2.73}$$

From this equation, we can see that there is a minimum frequency in which the magnetic resonance can be obtained, below that only evanescent waves are generated. Also, note that the ratio between the two transverse magnetization components is now

$$\frac{m_y}{m_x} = -i\frac{\omega_0 + \omega_M(l_{ex}^2 k^2 + sin^2\theta)}{\omega_k}, \tag{2.74}$$

which shows that the magnetization precession is elliptical, and not circular as before.

In the limit of small values of k, $l_{ex}^2 k^2 \ll 1$, the relation simplifies to $\omega = \sqrt{\omega_0(\omega_0 + \omega_M sin^2\theta)}$, which is called the dipolar spin waves limit, where the exchange interaction is negligible and the magnetostatic interaction dominates. On the other hand, for large values of k, $l_{ex}^2 k^2 \gg 1$, the exchange spin waves are obtained, with a quadratic dispersion $\omega = \omega_M l_{ex}^2 k^2$. Note that the exchange spin wave are isotropic with respect to the propagation direction, but the same is not true for the dipolar spin waves, which is dependent on $\theta$.

### 2.3.3 Spin waves in thin films

We shall now consider the magnetization dynamics in ferromagnetic thin films. Consider a thin film with thickness $d$, placed in the xz-plane under an in-plane external field in the z-direction, $\vec{H}_0 = H_0\hat{z}$. We will consider the dynamic magnetization components and the fields as uniform along the thickness as $kd \ll 1$. Again the dynamic components of the magnetization are in both the x and y-axes.

Since the exchange field is not affected by the thin film geometry equation 2.65 is still valid. On the other hand, the film boundaries create magnetic surface charges that strongly

influence the dipolar field. An approximation for the dynamic dipolar field in a thin film can be obtained in the form of [92]

$$\vec{h}_{dip} = -\Big[P\frac{\vec{k}\cdot\vec{m}}{k^2}\vec{k} + (1-P)(\vec{n}\cdot\vec{m})\vec{n}\Big], \tag{2.75}$$

where $\vec{n}$ is the normal vector to the plane, in this case $\vec{n} = \hat{y}$, and

$$P = 1 - \frac{1-e^{-kd}}{kd}. \tag{2.76}$$

Assuming that $\theta$ is the angle between $\vec{M}_0$ and $\vec{k}$, and that we are looking for in-plane travelling waves, that is $\vec{k} = k_x\hat{x} + k_z\hat{z}$, we can obtain for the dipolar field

$$\vec{h}_{dip} = -\begin{bmatrix} P\sin^2\theta & 0 & P\sin\theta\cos\theta \\ 0 & 1-P & 0 \\ P\sin\theta\cos\theta & 0 & P\cos^2\theta \end{bmatrix}\vec{m} \tag{2.77}$$

Now, applying in the LLG equation and linearizing by looking for harmonic travelling solutions we obtain the equations

$$[\omega_0 + \omega_M(l_{ex}^2k^2 + P\sin^2\theta)]m_x - i\omega m_y = 0, \tag{2.78}$$

$$i\omega m_x + [\omega_0 + \omega_M(l_{ex}^2k^2 + 1 - P)]m_y = 0. \tag{2.79}$$

And from this, we can obtain the dispersion relation of spin waves in ferromagnetic thin films as [80, 92]

$$\omega = \sqrt{(\omega_0 + \omega_M l_{ex}^2k^2)(\omega_0 + \omega_M l_{ex}^2k^2 + \omega_M F_M)}, \tag{2.80}$$

where

$$F_M = 1 - P\cos^2\theta + \frac{\omega_M P(1-P)\sin^2\theta}{\omega_0 + \omega_M l_{ex}^2k^2}, \tag{2.81}$$

see the plot in Figure 2.7.

Here, in the exchange limit, that is for small wavelengths, $l_{ex}^2k^2 \gg 1$, we obtain the same result as for the bulk sample, $\omega = \omega_M l_{ex}^2k^2$. On the other hand, in the dipole limit, $l_{ex}^2k^2 \ll 1$, the results are quite different from the bulk case. Let us check the two limiting cases from dipole spin waves in thin films, for $\theta = 0$ and $\theta = \pi/2$.

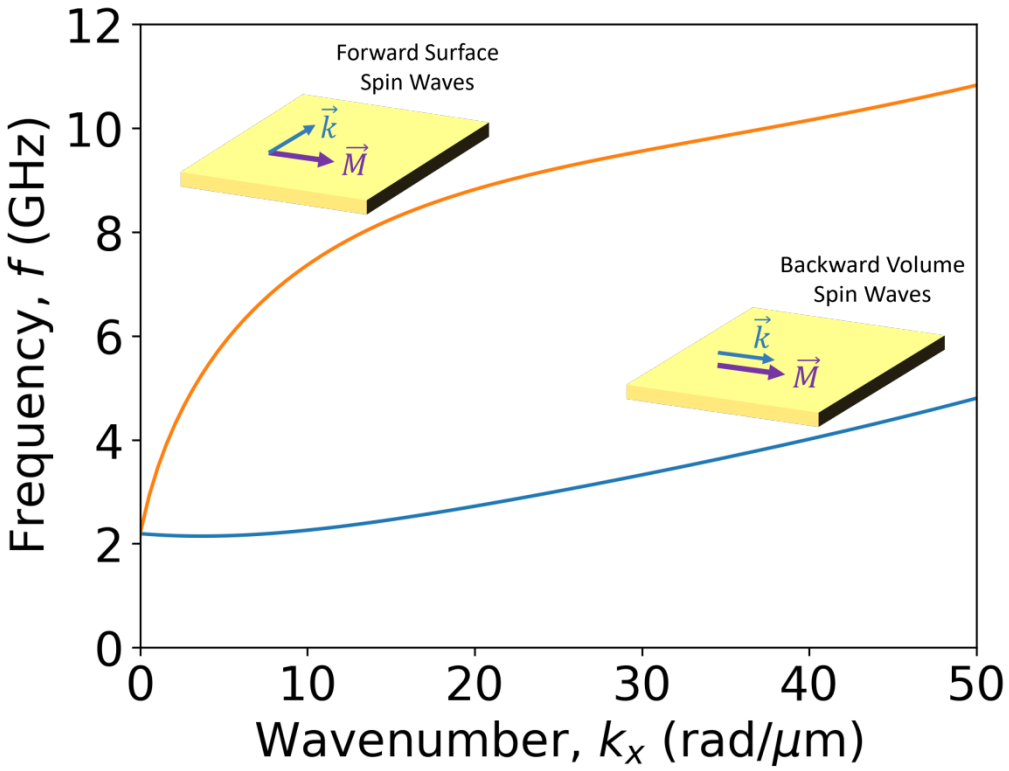


Figure 2.7: The dispersion relation for propagating spin waves in a 50 nm-tick Ni film ($M_s = 480kA/m$ and $A_{ex} = 8pJ/m$) under a 10 mT external magnetic field, taking into account both exchange and dipolar interactions from equation 2.80. The two curves plotted represent the backward volume spin waves, which are generated when the magnetization is parallel to the wavevector, and the forward surface waves, which occur when the magnetization is perpendicular to the wavevector.

First, for $\theta = 0$, that is the wave vector parallel to the static magnetization ($\vec{k} \parallel \vec{M}_0$), the dispersion relation in the dipolar limit becomes

$$\omega_{BVSW} = \sqrt{\omega_0\left(\omega_0 + \omega_M \frac{1 - e^{-kd}}{kd}\right)}. \tag{2.82}$$

In this mode, the frequency decreases with increasing wave vector and thus, we have a negative group velocity $v_g = \partial\omega/\partial k$ with a positive phase velocity $v_p = \omega/k$. For this reason these dipolar waves are known as Backward Volume Spin waves (BVSW).

Now for $\theta = \pi/2$, that is, for the wave vector perpendicular to the static magnetization ($\vec{k} \perp \vec{M}_0$), the dispersion relation in the dipolar limit is

$$\omega_{FSSW} = \sqrt{\omega_0(\omega_0 + \omega_M) + \omega_M\Big(1 - \frac{1 - e^{-kd}}{kd}\Big)\Big(\frac{1 - e^{-kd}}{kd}\Big)}. \tag{2.83}$$

Here, both the phase and group velocities are positive, and the amplitude of the magnetization decays exponentially from the surface, thus this dipolar wave is known as Forward Surface Spin wave (FSSW).

In conclusion, in this section we have discussed spin waves in ferromagnets, both in bulk materials and thin films. We obtained the dispersion relations, which provide valuable insights into the behavior of these waves. In thin films, the spin waves in the exchange limit are isotropic with respect to the magnetization and have a similar behavior as in the bulk sample. On the other hand, in the dipole limit, the waves are strongly anisotropic, and very different behaviors are obtained, such as the group velocity that is positive when $\vec{k} \perp \vec{M}_0$ and negative for $\vec{k} \parallel \vec{M}_0$.

## 2.4 Elastic waves

Similar to the spin waves, the elastic deformations in a material can also propagate as elastic waves. In this section we shall briefly introduce the physics of the elasticity in solids, the elastodynamics equation of motion and discuss its wave-like solutions, the elastic waves.

### 2.4.1 Elastodynamics

Consider a continuous and isotropic solid material with mass density $\rho$. The elastic deformations in it can be expressed by the displacement vector $\vec{u} = \vec{r} - \vec{r'}$, where $\vec{r}$ is the initial position of the volume element and $\vec{r'}$ is its position after deformation. The solid deformations can also be described by the second-order strain tensor[79, 93, 94]

$$\varepsilon_{ij} = \frac{1}{2}\left(\frac{\partial u_i}{\partial x_j}\frac{\partial u_j}{\partial x_i}\right), \tag{2.84}$$

where $i, j = 1, 2, 3$ are, respectively, the x, y and z coordinates.

The deformations in the volume elements are generated by forces acting on it, both from external agents and from the neighbouring elements, the elastic forces. The elastic forces per unit volume can be evaluated as

$$\vec{F}_{el} = \sum_{i=1}^{3} \hat{x}_i \sum_{j=1}^{3} \frac{\partial \sigma_{ij}}{\partial x_j} \quad \text{or} \quad \vec{F}_{el} = \nabla \cdot \overline{\sigma}, \tag{2.85}$$

where $\nabla$ is the differential vector operator and $\overline{\sigma}$ is the second-order stress tensor, where its components $\sigma_{ij}$ represent the forces per unit area acting normal to the direction of $\hat{x}_i$.

For small displacements, we obtain from Hooke's law that the displacement is proportional to the stress as

$$\sigma_{ij} = \sum_{l=1}^{3} \sum_{m=1}^{3} C_{ijkl} \varepsilon_{kl} \quad \text{or} \quad \overline{\sigma} = \overline{\overline{C}} \overline{\varepsilon}, \tag{2.86}$$

where $\overline{\overline{C}}$ is the fourth-rank stiffness tensor and $C_{ijkl}$ are the elastic constants. It can be shown that there are 21 independent elastic constants due to the symmetry of the strain and stress tensors [79]. Also, the higher the symmetry of the crystal structure, the less nonzero elastic constant values will be present. For example, in a cubic crystal only three nonzero elastic constants are found, $C_{iiii} = C_{11}$, $C_{iijj} = C_{12}$ and $C_{ijij} = C_{44}$. It can be also shown that if the cubic material is isotropic we obtain the relation $C_{11} - C_{12} = 2C_{44}$, thus only two independent elastic constants will be present.

The equation of motion for the displacement, obtained from Newton's second law, is

$$\rho \frac{d^2 \vec{u}}{dt^2} = \nabla \cdot \overline{\sigma} + \vec{F}_{ext} \tag{2.87}$$

where $F_{ext}$ are the external forces per unit volume acting on the material and $\nabla \cdot \overline{\sigma}$ is the elastic force per unit volume. In the absence of external forces, the equation of motion can be written as

$$\rho \frac{\partial^2 u_i}{\partial t^2} = \frac{\partial}{\partial x_j} \Big( C_{ijkl} \frac{\partial u_k}{\partial x_l} \Big). \tag{2.88}$$

Note that in this equation repeated subscripts imply summation of these values.

Now, considering a cubic crystal, which only has three non-null elastic constants, we get the equation of motion

$$\rho \frac{\partial^2 u_i}{\partial t^2} = C_{11} \frac{\partial^2 u_i}{\partial x_i^2} + C_{12} \frac{\partial^2 u_i}{\partial x_i x_j} + C_{44} \frac{\partial^2 u_i}{\partial x_j^2}. \tag{2.89}$$

### 2.4.2 Elastic waves in thin films

Let us now consider the equation of motion for a thin film, placed in the xz-plane, with free surface boundary conditions. In this case, the displacement along the normal direction is negligible in relation to the in-plane ones, that is $\partial u/\partial y \ll \partial u/\partial x, \partial u/\partial z$. We obtain from equation 2.89, the relations

$$\rho\frac{\partial^2 u_x}{\partial t^2} = C_{11}\frac{\partial^2 u_x}{\partial x^2} + C_{44}\frac{\partial^2 u_x}{\partial z^2} + (C_{12}+C_{44})\frac{\partial^2 u_z}{\partial x \partial z}, \tag{2.90}$$

$$\rho\frac{\partial^2 u_y}{\partial t^2} = C_{44}\Big(\frac{\partial^2 u_y}{\partial x^2} + \frac{\partial^2 u_y}{\partial z^2}\Big), \tag{2.91}$$

$$\rho\frac{\partial^2 u_z}{\partial t^2} = C_{11}\frac{\partial^2 u_z}{\partial z^2} + C_{44}\frac{\partial^2 u_z}{\partial x^2} + (C_{12}+C_{44})\frac{\partial^2 u_x}{\partial x \partial z}. \tag{2.92}$$

Now, let us linearize the equations by looking for the plane wave solutions $\vec{u}(\vec{r},t) = \vec{u}e^{i(\vec{k}\cdot\vec{r}-\omega t)}$. Let us also let us consider that the wave vector points along the in-plane x-direction, $\vec{k} = k\hat{x}$, resulting in

$$\Big(\omega^2 - \frac{C_{11}}{\rho}k^2\Big)u_x = 0, \quad \Big(\omega^2 - \frac{C_{44}}{\rho}k^2\Big)u_y = 0, \quad \text{and} \quad \Big(\omega^2 - \frac{C_{44}}{\rho}k^2\Big)u_z = 0. \tag{2.93}$$

Observe that the solutions for these equations are given by linear dispersion relations in the form of

$$\omega_\mu = v_\mu k, \tag{2.94}$$

where $v_\mu$ is the sound wave velocity. For the transverse y and z directions, we obtain shear or transverse elastic waves with velocity $v_t = \sqrt{C_{44}/\rho}$, and for the x direction ($\vec{u} \parallel \vec{k}$) we obtain longitudinal waves with velocity $v_l = \sqrt{C_{11}/\rho}$. From that, we can see that the phase and group velocities are equal to each other and they are independent of the frequency. Also, as $C_{11} > C_{44}$, the velocity of the longitudinal waves is always larger than the velocity of the shear waves.

### 2.4.3 Elastic waves in waveguides

Now, we will consider the effect of lateral boundaries in the equations for the elastic waves. Consider a plate placed in the xy-plane with infinite length along the x-direction, with width $2b$ in the y-direction. For an elastic wave propagating the x-axis, $\vec{k} = k\hat{x}$, the two

in-plane modes are coupled to each other, but the out-of-plane modes are uncoupled from the others [93, 95]. We will start with the out-of-plane modes, then we will check the results for the in-plane modes.

For the out-of-plane modes, we will consider the wave equation of the z-displacement,

$$\nabla^2 u_z = \frac{1}{v_{perp}^2}\frac{\partial^2 u_z}{\partial t^2}, \tag{2.95}$$

where is uniform along the thickness of the plate, that is $u_z = u_z(x, y, t)$. Note that $u_z$ propagates along the x-direction and its amplitude can vary along the width (y-direction). We will consider solutions in the form of $u_z = h(y)e^{i(kx-\omega t)}$. From that we obtain

$$\frac{d^2h}{dy^2} + \kappa_y^2 h = 0 \quad \text{where} \quad \kappa_y^2 = \frac{\omega^2}{v_\perp^2} - k^2, \tag{2.96}$$

which accepts $h(y) = A_1 \sin(\kappa_y y) + A_2 \cos(\kappa_y y)$ as a solution.

Considering the boundary conditions, at $y = \pm b$ we have $\sigma_{xy} = \sigma_{yy} = \sigma_{zy} = 0$, which results in

$$\left.\frac{\partial u_z}{\partial y}\right|_{y=\pm b} = 0. \tag{2.97}$$

From that we can obtain the equations

$$A_1 \cos(\kappa_y b) - A_2 \sin(\kappa_y b) = 0, \tag{2.98}$$

$$A_1 \cos(\kappa_y b) + A_2 \sin(\kappa_y b) = 0. \tag{2.99}$$

That results in $\cos(\kappa_y b)\sin(\kappa_y b) = 0$, and that is satisfied by

$$\kappa_y = \frac{n\pi}{2b} \quad (n = 0, 1, 2, ...). \tag{2.100}$$

where $n$ is the mode order, which is a consequence of the formation of standing waves across the y-direction.

Note that, from these conditions, if $n$ is even, then $A_1 = 0$, so the amplitude along the y-direction is only composed of the sin part, that is $u_z = A_2 \cos(\kappa_y y)e^{i(kx-\omega t)}$, so the displacement is symmetric in relation to y=0. Similarly, if $n$ is odd, then $A_2 = 0$ and $u_z = A_1 \sin(\kappa_y y)e^{i(kx-\omega t)}$, we have an antisymmetric elastic wave.

Thus, the dispersion relation for the harmonic out-of-plane elastic waves, also called P-waves, is

$$\omega = v_{\perp}\sqrt{k^2 + \frac{n\pi}{2b}} \quad (n = 0, 1, 2, 3, ...). \tag{2.101}$$

The infinite number of modes yields an infinite number of branches as solutions in the dispersion curve, see Figure 2.8. Also, this elastic wave is either symmetric or antisymmetric in relation to $y = 0$ if the mode order $n$ is even or odd, respectively.

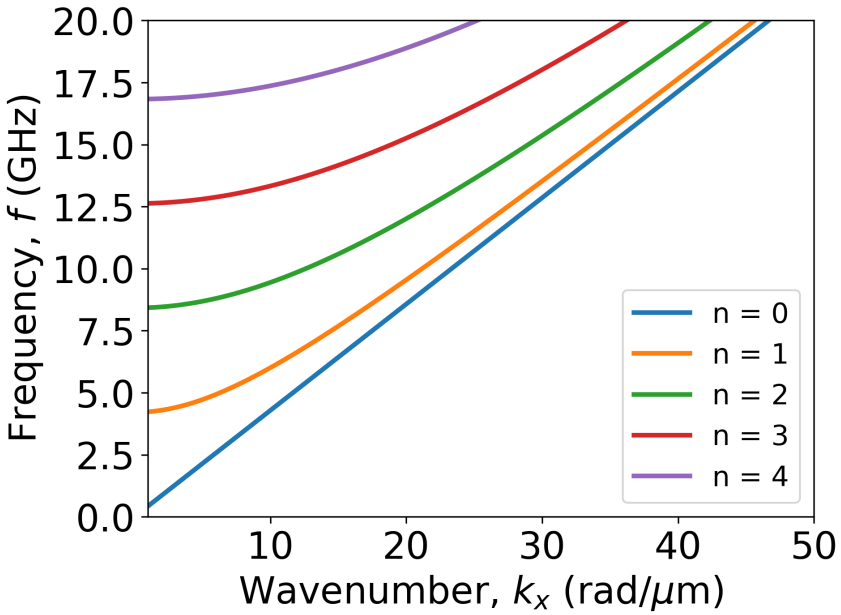


Figure 2.8: Dispersion relation of elastic P-waves propagating in a 20 nm thick, 320 nm wide CoFeB waveguide ($\rho = 8000kg/m^3$, $C_{11} = 283GPa$, $C_{12} = 166GPa$, and $C_{44} = 58GPa$), obtained from equation 2.101.

Now, let us focus in the in-plane elastic waves. Here, we will also consider the formation of a standing wave in the y-direction with a propagating wave in the x-direction. To do this, it is convenient to use Helmholtz's theorem and decompose the displacement field by the use of scalar and vector potentials [93, 95],

$$\vec{u} = \nabla\varphi + \nabla \times \vec{\psi}, \tag{2.102}$$

where $\phi$ is the scalar potential and $\psi$ is the vector potential.

In this case, for the motion in the xy-plane we have $u_z = 0$ and any derivative in relation to z also zero, reducing the equations to

$$u_x = \frac{\partial \varphi}{\partial x} + \frac{\partial \psi_z}{\partial y} \quad \text{and} \quad u_y = \frac{\partial \varphi}{\partial y} + \frac{\partial \psi_z}{\partial x}. \tag{2.103}$$

The potentials $\varphi$ and $\psi_z$ must satisfy wave equations, which are two-dimensional in this case,

$$\frac{\partial^2 \varphi}{\partial x^2} + \frac{\partial^2 \varphi}{\partial y^2} = \frac{1}{v_\parallel^2}\frac{\partial^2 \varphi}{\partial t^2} \quad \text{and} \quad \frac{\partial^2 \psi_z}{\partial x^2} + \frac{\partial^2 \psi_z}{\partial y^2} = \frac{1}{v_\perp^2}\frac{\partial^2 \psi_z}{\partial t^2}. \tag{2.104}$$

Let us now consider harmonic plane wave solutions as $\varphi = \Phi(y)e^{i(kx-\omega t)}$ and $\psi_z = \Psi(y)e^{i(kx-\omega t)}$ in the differential equations to obtain

$$\Phi(y) = A_1 \sin(py) + A_2 \cos(py), \tag{2.105}$$

$$\Psi(y) = B_1 \sin(qy) + B_2 \cos(qy), \tag{2.106}$$

where

$$p^2 = \frac{\omega^2}{v_\parallel^2} - k^2 \quad \text{and} \quad q^2 = \frac{\omega^2}{v_\perp^2} - k^2. \tag{2.107}$$

From those, we can obtain the displacements as

$$u_x = ik\Phi + \frac{d\Psi}{dy} \quad \text{and} \quad u_y = \frac{d\Phi}{dy} - ik\Psi, \tag{2.108}$$

or more explicitly,

$$u_x = ik[A_1 \sin(py) + A_2 \cos(py)] + q[B_1 \cos(qy) - B_2 \sin(qy)], \tag{2.109}$$

$$u_y = p[A_1 \cos(py) - A_2 \sin(py)] - ik[B_1 \sin(qy) + B_2 \cos(qy)]. \tag{2.110}$$

Note that $u_x$ is symmetric in relation to $y = 0$ if it is described only by cosines, which would require $A_1 = B_2 = 0$, and that would imply in $u_y$ being described only by sines. The opposite is also true, an antisymmetric $u_x$ must be described by the sines, then $A_2 = B_1 = 0$, which implies that $u_y$ is described by cosines. We can then split the in-plane elastic waves in symmetric, where $\Phi = A_2 \cos(py)$ and $\Psi = B_1 \sin(qy)$ and antisymmetric modes, with $\Phi = A_1 \sin(py)$ and $\Psi = B_2 \cos(qy)$, which we will call, respectively S-waves and A-waves.

Now, we can apply the free boundary condition, at $y = \pm b$ we have $\sigma_{yx} = \sigma_{yy} = 0$, to obtain

$$\frac{\tan(qb)}{\tan(pb)} = -\frac{4k^2pq}{(q^2-k^2)^2} \tag{2.111}$$

for S-waves, and

$$\frac{\tan(qb)}{\tan(pb)} = -\frac{(q^2-k^2)^2}{4k^2pq} \tag{2.112}$$

for A-waves. These are known as the Rayleigh-Lamb frequency equations, see Figure 2.9.

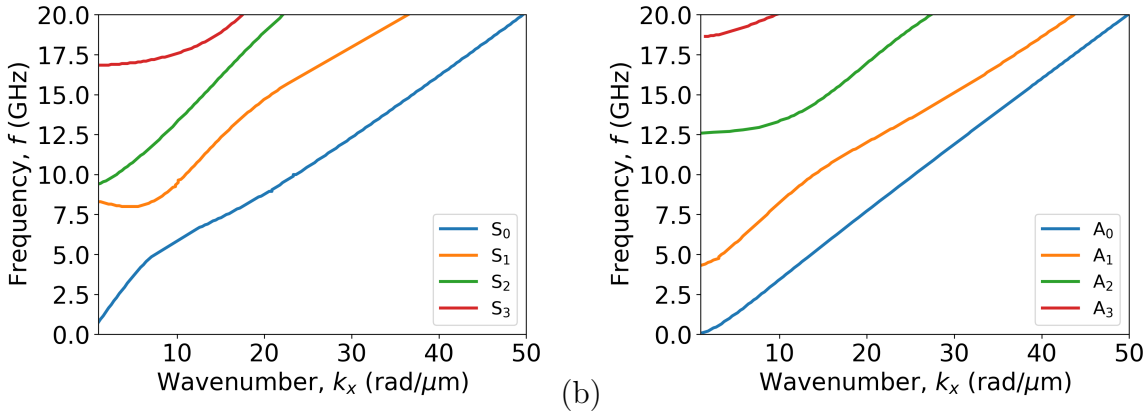


(a) (b)

Figure 2.9: Dispersion relation of elastic (a) S-waves and (b) A-waves propagating in a 20 nm thick, 320 nm wide CoFeB waveguide ($\rho = 8000 kg/m^3$, $C_{11} = 283 GPa$, $C_{12} = 166 GPa$, and $C_{44} = 58 GPa$), obtained from equations 2.111 and 2.112.

Finally, there are three modes of elastic waves propagating in a waveguide with finite width, the out-of-plane P-waves, and the in-plane S-waves and A-waves. The P-wave modes present alternating $u_z$ symmetry, according to the evenness of the mode order. The S-waves present $u_x$ displacements symmetric in relation to $y = 0$ and antisymmetric $u_y$, whereas the A-waves present antisymmetric $u_x$ with symmetric $u_y$.

## 2.5 Magnetoelastic waves

In this section, we will present a phenomenological description of the magnetoelastic interaction. Specifically, we will examine the free energy term that connects the magnetization

and strain components of magnetoelastic materials and its impact on the solutions of wave propagation in both the elastodynamic equation of motion and the Landau-Lifshitz-Gilbert equation.

### 2.5.1 Magnetoelastic interaction

The magnetoelastic interaction is a phenomenon that describes the relationship between magnetic and elastic degrees of freedom in a material. This coupling results from the exchange interaction dependence on the distance between magnetic moments, which is affected by deformations, as well as the dipolar interaction dependence on these distances, but over longer ranges. However, the spin-orbit interaction is the primary cause of the magnetoelastic interaction. [94].

The magnetoelastic interaction comprises two distinct phenomena: the magnetostrictive effect, which refers to the influence of magnetization on a magnetic material internal strains, and the Villari effect, which describes the impact of strain on the magnetization state of the material [80].

The magnetoelastic free energy density can be described phenomenologically as

$$E_{me} = B_{ijkl} M_i M_j \varepsilon_{kl}, \tag{2.113}$$

where the summations are implicit, $B_{ijkl}$ are the magnetoelastic constant fourth-rank tensor components and $\varepsilon_{kl}$, the strain components.

For a cubic crystal there are only two non-zero constants, $B_{iiii} = B_1$ and $B_{ijij} = B_2$, so the magnetoelastic energy density becomes

$$E_{me} = \frac{B_1}{M_s^2}\left[\varepsilon_{xx}(M_x^2 - 1/3) + \varepsilon_{yy}(M_y^2 - 1/3) + \varepsilon_{zz}(M_z^2 - 1/3)\right] + 2\frac{B_2}{M_s^2}(\varepsilon_{xy}M_xM_y + \varepsilon_{yz}M_yM_z + \varepsilon_{xz}M_xM_z), \tag{2.114}$$

.

For the magnetostrictive effect, we will now obtain the elastic body force that arises from the magnetoelastic interaction energy by using the expression

$$\vec{F}_{me} = \nabla \cdot \overline{\sigma}_{me} = \nabla \cdot \left(\frac{dE_{me}}{d\varepsilon_{ij}}\right), \tag{2.115}$$

from which we obtain, for a cubic material,

$$\vec{F}_{me} = 2\frac{B_1}{M_s^2}\begin{bmatrix} M_x\frac{\partial M_x}{\partial x} \\ M_y\frac{\partial M_y}{\partial y} \\ M_z\frac{\partial M_z}{\partial z} \end{bmatrix} + \frac{B_2}{M_s^2}\begin{bmatrix} M_x(\frac{\partial M_y}{\partial y}+\frac{\partial M_z}{\partial z}) + M_y\frac{\partial M_x}{\partial y} + M_z\frac{\partial M_x}{\partial z} \\ M_y(\frac{\partial M_x}{\partial x}+\frac{\partial M_z}{\partial z}) + M_x\frac{\partial M_y}{\partial x} + M_z\frac{\partial M_y}{\partial z} \\ M_z(\frac{\partial M_x}{\partial x}+\frac{\partial M_y}{\partial y}) + M_x\frac{\partial M_z}{\partial x} + M_y\frac{\partial M_y}{\partial y} \end{bmatrix}. \tag{2.116}$$

Note that there are three important parameters that influence the strength of the magnetostriction, the magnetoelastic constants, the magnetization direction, and its gradient.

Now, for the Villari effect, we can obtain the effective magnetic field from the magnetoelastic free energy using $\vec{H}_{me} = -\nabla_{\vec{M}} E_{me}/\mu_0$, from which we obtain

$$\vec{H}_{me} = -\frac{2}{\mu_0 M_s^2}\begin{bmatrix} B_1\varepsilon_{xx}M_x + B_2(\varepsilon_{xy}M_y + \varepsilon_{xz}M_z) \\ B_1\varepsilon_{yy}M_y + B_2(\varepsilon_{xy}M_x + \varepsilon_{yz}M_z) \\ B_1\varepsilon_{zz}M_z + B_2(\varepsilon_{xz}M_x + \varepsilon_{yz}M_y) \end{bmatrix}. \tag{2.117}$$

Now, in order to describe the dynamics of materials with magnetoelastic coupling, we should include the magnetoelastic energy both in the elastodynamic equation of motion, equation 2.87, in the form of an effective body force, as equation 2.116 for cubic materials, and in the LLG equation, equation 2.7, for the magnetization dynamics, in the form of an effective magnetic field, as in equation 2.117. These two equations become coupled to each other due to the magnetoelastic energy, and should be solved simultaneously.

### 2.5.2 Magnetoelastic waves in bullk ferromagnet

Now we want to look for wave-like solutions to solve simultaneously the equations 2.87 and 2.7 for a cubic bulk material including the magnetoelastic energy, equation 2.114.

Consider a bulk material, with a static magnetic field applied in the z-direction, so that $\vec{M} = m_x\hat{x} + m_y\hat{y} + M_z\hat{z}$, where $m_x, m_y \ll M_z \approx M_s$. From this we can simplify the magnetoelastic energy equation to only include first-order magnetization terms as

$$E_{me} = 2\frac{B_2}{M_s^2}(m_y\varepsilon_{yz} + m_x\varepsilon_{zx}). \tag{2.118}$$

The equation of motion can be obtained by the two differential equations as a magnetoelastic effective magnetic field,

$$\vec{h}_{me} = -\frac{2B_2}{\mu_0 M_s}(\varepsilon_{zx}\hat{x} + \varepsilon_{yz}\hat{y}). \tag{2.119}$$

So, we can write the LLG equation, without considering the damping, as

$$\frac{\partial \vec{m}}{\partial t} = -\gamma\mu_0 \vec{M} \times (\vec{H}_0 + \vec{h}_{ex} + \vec{h}_{dip} + \vec{h}_{me}). \tag{2.120}$$

And also, the elastodynamic equation of motion, including the elastic term and the magnetoelastic one, becomes

$$\rho\frac{\partial^2 u_i}{\partial t^2} = \frac{\partial}{\partial x_j}\left(C_{ijkl}\frac{\partial u_k}{\partial x_l}\right) + \frac{\partial}{\partial x_j}\left[\frac{\partial E_{me}}{\partial \varepsilon_{ij}}\right]. \tag{2.121}$$

From these coupled equations, considering small signal magnetization and elastic components, we obtain

$$\frac{\partial m_x}{\partial t} = \gamma\mu_0(-H_0 + D\nabla^2)m_y + \gamma\mu_0 M_s h_y^{dip} - \gamma B_2\Big(\frac{\partial u_y}{\partial z} + \frac{\partial u_z}{\partial y}\Big), \tag{2.122}$$

$$\frac{\partial m_y}{\partial t} = \gamma\mu_0(H_0 - D\nabla^2)m_x - \gamma\mu_0 M_s h_x^{dip} - \gamma B_2\Big(\frac{\partial u_z}{\partial x} + \frac{\partial u_x}{\partial z}\Big), \tag{2.123}$$

$$\rho\frac{\partial^2 u_x}{\partial t^2} = C_{44}\nabla^2 u_x + C_{11}\frac{\partial}{\partial x}\nabla\cdot\vec{u} + \frac{B_2}{M_s}\frac{\partial m_x}{\partial z}, \tag{2.124}$$

$$\rho\frac{\partial^2 u_y}{\partial t^2} = C_{44}\nabla^2 u_y + C_{11}\frac{\partial}{\partial y}\nabla\cdot\vec{u} + \frac{B_2}{M_s}\frac{\partial m_y}{\partial z}, \tag{2.125}$$

$$\rho\frac{\partial^2 u_z}{\partial t^2} = C_{44}\nabla^2 u_z + C_{11}\frac{\partial}{\partial z}\nabla\cdot\vec{u} + \frac{B_2}{M_s}\left(\frac{\partial m_x}{\partial x} + \frac{\partial m_y}{\partial y}\right), \tag{2.126}$$

where $D$ is the exchange parameter, $D = A_{ex}/M_s$.

Now, we will look at wave-like solutions for these coupled equations, which involve all five variables $m_x$, $m_y$, $u_x$, $u_y$ and $u_z$. For simplicity, let us consider the case in which the waves propagate parallel to the magnetization direction, $\vec{k} = k\hat{z}$. First, note that in that case $\partial/\partial x = \partial/\partial y = 0$, and that applied to equation 2.126 for $u_z$ eliminates all the magnetization components. Thus, we have a longitudinal elastic wave $u_z$ that does not couple to the spin waves.

Now, for the other four equations, let us consider harmonic solutions $\vec{u}(\vec{r}, t) = \vec{u}e^{i(kz-\omega t)}$

and $\vec{m}(\vec{r},t) = \vec{m}e^{i(kz-\omega t)}$. We obtain

$$-i\omega m_x = -\gamma\mu_0(H_0 + Dk^2)m_y - i\gamma B_2 k u_y, \tag{2.127}$$
$$-i\omega m_y = \gamma\mu_0(H_0 + Dk^2)m_y + i\gamma B_2 k u_x, \tag{2.128}$$
$$-\rho\omega^2 u_x = -C_{44}k^2 u_x + iB_2 k m_x/M_s, \tag{2.129}$$
$$-\rho\omega^2 u_y = -C_{44}k^2 u_y + iB_2 k m_y/M_s. \tag{2.130}$$

We can introduce circularly polarized variables $m^- = m_x - im_y$ and $u^- = u_x - iu_y$ and obtain

$$(\omega - \omega_k)m^- = i\gamma B_2 k u^-, \tag{2.131}$$
$$(\omega - \omega_t)u^- = i\frac{B_2}{M\rho}B_2 k m^-, \tag{2.132}$$

where

$$\omega_k = \gamma\mu_0(H_0 + Dk^2) \quad \text{and} \quad \omega_t = \sqrt{C_{44}/\rho}k = v_\perp k \tag{2.133}$$

are respectively the dispersion relations to the spin waves in an unbounded media and the transverse elastic waves, both without considering the magnetoelastic interaction.

Combining these two equations, we obtain the dispersion relation for the magnetoelastic wave in unbounded media as [79]

$$(\omega - \omega_k)(\omega^2 - \omega_t^2) - \frac{1}{2}J_k\omega_t = 0, \tag{2.134}$$

where $J_k$ is a parameter that expresses the strength of the magnetoelastic coupling,

$$J_k = \frac{2\gamma k B_2^2}{\rho v_\perp M_s}. \tag{2.135}$$

This dispersion equation admits three roots, which comes from the interaction between the spin wave and the two transverse elastic waves. For a null magnetoelastic coupling, $B_2 = 0$ and $J_k = 0$, the roots for equation 2.134 are $\omega_k$ and $\pm\omega_t$, that is, respectively, the magnetic and the (+) and (-) circularly polarized elastic waves, uncoupled from each other.

With non-zero $B_2$, the results are coupled magnetoelastic waves. As the magnetic wave always presents a (+) circular polarization, the elastic wave with (-) polarization presents a

negligible coupling, and we can approximate one negative root as $\omega \approx -\omega_t$. Thus, equation 2.134 reduces to

$$(\omega - \omega_k)(\omega - \omega_t) - J_k/4\omega_t = 0, \tag{2.136}$$

which has the two solutions

$$\omega = \frac{\omega_t + \omega_k}{2} \pm \frac{1}{2}\sqrt{(\omega_t - \omega_k)^2 + J_k}, \tag{2.137}$$

that correspond, respectively to the upper and lower branches of the dispersion curves, see Figure 2.10.

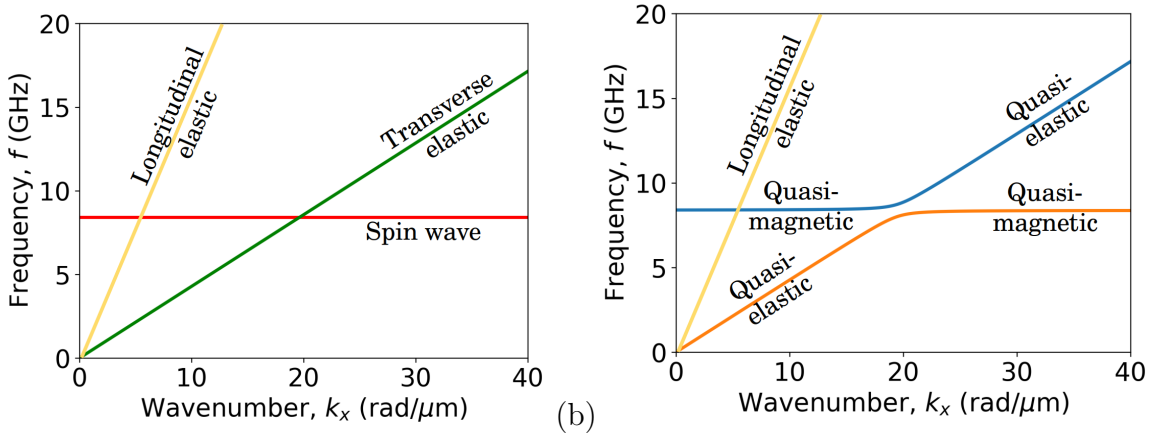


Figure 2.10: Dispersion curves for elastic waves and spin waves in a bulk CoFeB sample ($M_S = 1.2MA/m$, $A_{ex} = 18pJ/m$, $\rho = 8000kg/m^3$, $C_{11} = 283GPa$, $C_{12} = 166GPa$, $C_{44} = 58GPa$, and $B_1 = B_2 = -8.8MJ/m^3$), obtained from equation 2.137. Panel (a) represents the uncoupled waves, while panel (b) includes the coupling between them, resulting in the hybridization of the curves and the formation of an anticrossing gap between the transverse elastic and the spin wave. The upper branch of the hybridized curves transitions from quasi-magnetic to quasi-elastic behavior, while the lower branch transitions from quasi-elastic to quasi-magnetic.

A distinct characteristic of the magnetoelastic hybridization is the splitting between the curves at their meeting point, a small frequency gap is present between the branches, forming an anticrossing region. Far from the crossing point the curves correspond to almost pure magnetic or pure elastic characters. Hence, the lower branch transits from a almost pure elastic character for low values of k to an almost pure magnetic character at high

values of k, and the opposite happens for the upper branch. Near the crossing point, the normal modes are mixed and they present a coupled magnetoelastic character.

We can also obtain energy and momentum conservation relations for this system. The total energy ($E$) of the system can be evaluated as the sum of the magnetic ($E_m$), elastic ($E_e$) and magnetoelastic ($E_{me}$) components, $E = E_m + E_e + E_{me}$. By using Poynting's theorem and the small signal approximation from equations 2.122, 2.124 and 2.126, that the conservation can be expressed as [79]

$$\nabla \cdot \vec{\mathcal{S}} + \frac{\partial E}{\partial t} = \frac{1}{2}\mu_0 \frac{|\vec{m}|^2}{M}\frac{\partial H_z}{\partial t} - p_T, \tag{2.138}$$

where $\vec{\mathcal{S}}$ is the power flow vector and $p_T$ is the power per unit volume that is dissipated.

Also, for the small-signal approximation, the momentum density can be expressed as a magnetic and elastic components as, respectively, for the i-th component:

$$g_m^i = \frac{1}{2\gamma M}\left(\vec{m} \times \frac{\partial \vec{m}}{\partial x_i}\right) \cdot \hat{z}, \tag{2.139}$$

$$g_e^i = \frac{1}{2}\rho\left(\frac{\partial^2 \vec{u}}{\partial x_i \partial t} \cdot \vec{u} - \frac{\partial \vec{u}}{\partial t}\frac{\partial \vec{u}}{\partial x_i}\right). \tag{2.140}$$

If the magnetic field and all parameters are spatially invariant, then the total momentum is conserved

$$\frac{\partial}{\partial t}(\vec{g_m} + \vec{g_e}) = 0. \tag{2.141}$$

### 2.5.3 Magnetoelastic waves in thin films

Now, let us consider a thin film placed in the xz-plane, normal to the y-direction, with thickness $d$. Consider the external field $\vec{H_0}$ and the static magnetization in the in-plane z-direction. We will follow the same procedures as before, considering $\vec{M} = m_x\hat{x} + m_y\hat{y} + M_z\hat{z}$ with $m_x, m_y \ll M_z \approx M_s$ in both the elastodynamics equation of motion and the LLG equation with only first-order terms, we obtain the coupled differential equations as 2.122-2.126.

Then, looking for harmonic wave-like solutions to these equations, and considering the wave propagates in plane that is $\vec{k} = k_x\hat{x} + k_y\hat{y}$, we can obtain the linear equations as [80]

$$i\omega m_x = -\omega_{m2} m_y - i\gamma B_2 k_z u_y, \tag{2.142}$$
$$i\omega m_y = -\omega_{m1} m_x + i\gamma B_2 (k_z u_x + k_y u_z), \tag{2.143}$$
$$-\rho\omega^2 u_x = -C_{11} k_x u_x - C_{44} k_z u_x - (C_{12} + C_{44}) k_x k_z u_z + i B_2 k_z m_x / M_s, \tag{2.144}$$
$$-\rho\omega^2 u_y = -C_{44}(k_x u_y + k_z u_y) + i B_2 k_z m_y / M_s, \tag{2.145}$$
$$-\rho\omega^2 u_z = -C_{11} k_z u_z - C_{44} k_x u_z - (C_{12} + C_{44}) k_x k_z u_x + i B_2 k_x m_x / M_s, \tag{2.146}$$

where

$$\omega_{m1} = \omega_0 + \omega_M (l_{ex}^2 k^2 + P \sin^2\theta), \tag{2.147}$$
$$\omega_{m2} = \omega_0 + \omega_M (l_{ex}^2 k^2 + 1 - P), \tag{2.148}$$

with $\theta$ being the angle between $\vec{M}_0$ and $\vec{k}$, $\omega_0 = \gamma\mu_0 H_0$, $\omega_M = \gamma\mu_0 M_s$ and

$$P = 1 - \frac{1 - e^{-kd}}{kd}. \tag{2.149}$$

Now, we will consider an isotropic material, so that $C_{12} = C_{11} - 2C_{44}$. The waves can propagate in any direction in-plane, but it is convenient to describe the elastic waves as a function of their longitudinal ($u_l \parallel k$) and transverse ($u_t \perp k$) components as

$$u_x = u_l \sin\theta + u_t \cos\theta \quad \text{and} \quad u_z = u_l \cos\theta + u_t \sin\theta, \tag{2.150}$$

where $\theta$ is the angle between $\vec{M}_0$ and $\vec{k}$. Thus, we obtain

$$(\omega^2 - \omega_l^2) \sin\theta u_l + (\omega^2 - \omega_h^2) \cos\theta u_t + i \frac{B_2 k \cos\theta}{\rho M_s} m_x = 0, \tag{2.151}$$
$$(\omega^2 - \omega_v^2) u_y + i \frac{B_2 k \cos\theta}{\rho M_s} m_y = 0, \tag{2.152}$$
$$(\omega^2 - \omega_l^2) \cos\theta u_l + (\omega^2 - \omega_h^2) \sin\theta u_t + i \frac{B_2 k \sin\theta}{\rho M_s} m_x = 0, \tag{2.153}$$
$$i\gamma B_2 k \cos\theta u_y + i\omega m_x + \omega_{m2} m_y = 0, \tag{2.154}$$
$$i\gamma B_2 \sin(2\theta) u_l + i\gamma B_2 k \cos(2\theta) u_t + \omega_{m1} m_x - i\omega m_y = 0, \tag{2.155}$$

where $\omega_l = v_\parallel k$, which is the dispersion of the longitudinal elastic waves, and $\omega_h = \omega_v = v_\perp k$, respectively the horizontal and vertically-polarized transverse elastic waves.

Now, we will analyze two special cases of the magnetoelastic waves in thin films, first, the magnetization perpendicular to the propagation direction, and then the magnetization parallel to $\vec{k}$.

### Wave propagation perpendicular to magnetization

First, for the propagation direction perpendicular to the magnetization, $\vec{k} \perp \vec{M}_0$, that is $\theta = \pi/2$. In this case, the uncoupled waves would give rise to the magnetic Forward Surface Spin waves (FSSW), with dispersion relation shown in equation 2.83. As $\vec{M}_0 = M_0\hat{z}$, we obtain $\vec{k} = k\hat{x}$ and $u_l = u_x$ and $u_t = u_z$ for the in-plane components of the magnetization, and $u_y$, the out-of-plane component.

For this case, the linearized equations become [80]

$$(\omega^2 - \omega_l^2)u_l = 0, \tag{2.156}$$
$$(\omega^2 - \omega_v^2)u_y = 0, \tag{2.157}$$
$$(\omega^2 - \omega_h^2)\sin\theta u_t + i\frac{B_2 k}{\rho M_s}m_x = 0, \tag{2.158}$$
$$i\omega m_x + \omega_{m2}m_y = 0, \tag{2.159}$$
$$-i\gamma B_2 k u_t + \omega_{m1}m_x - i\omega m_y = 0. \tag{2.160}$$

Note that longitudinal ($u_l$) and out-of-plane ($u_y$) components of the elastic wave are not coupled to the magnetization, so their dispersion relations remain unchanged from the uncoupled case, that is $\omega = \omega_l = v_\parallel k$ for $u_l$ and $\omega = \omega_v = v_\perp k$ for $u_y$.

The in-plane transverse elastic component ($u_t$) does couple to the forward surface spin waves. The set of coupled equations becomes, in matrix notation,

$$\begin{bmatrix} -i\gamma B_2 k & \omega_{m1} & -i\omega \\ 0 & i\omega & \omega_{m2} \\ \omega^2 - \omega_h^2 & i\frac{B_2 k}{\rho M_s} & 0 \end{bmatrix} \begin{bmatrix} m_x \\ m_y \\ u_t \end{bmatrix} = 0. \tag{2.161}$$

Now, to obtain the non-trivial solutions, the determinant must be zero, and we obtain

$$(\omega^2 - \omega_h^2)(\omega^2 - \omega_m^2) - J\omega_{m2}k^2 = 0, \tag{2.162}$$

where

$$J = \frac{\gamma B_2^2}{\rho M_s}, \tag{2.163}$$

$\omega_h = v_\perp k$, which is the dispersion of the uncoupled in-plane transverse elastic wave, and $\omega_m = \sqrt{\omega_{m1}\omega_{m2}}$ is the dispersion relation for the uncoupled forward surface spin waves.

Note that in the absence of magnetoelastic interaction, $J = 0$ and equation 2.162 presents the two solutions $\omega = \omega_h$ for the elastic wave and $\omega = \omega_m$ for the spin wave. Now, considering the magnetoelastic interaction, equation 2.162 presents two physically meaningful solutions,

$$\omega_\pm^2 = \frac{\omega_h^2 + \omega_m^2}{2} \pm \sqrt{\left(\frac{\omega_m^2 - \omega_h^2}{2}\right)^2 + J\omega_{m2}k^2}. \tag{2.164}$$

These two solutions refer to the two branches that are formed in the dispersion relation. If there was no coupling, the curves of the transverse elastic waves and the spin waves would cross each other. This does not happen when the magnetoelastic interaction is present, a gap is formed between the two curves generating an anticrossing behaviour. The frequency gap is proportional to the strength of the magnetoelastic interaction and can be evaluated as $\Delta\omega = 2J\omega_{m2}k_{cross}^2$, where $k_{cross}$ is the value where $\omega_h(k_{cross}) = \omega_m(k_{cross})$.

From these equations, we obtain two eigenstates as [80]

$$\begin{bmatrix} m_x \\ m_y \\ u_t \end{bmatrix} = N \begin{bmatrix} i\rho M_s(\omega_\pm^2 - \omega_h^2)/(kB_2) \\ \rho M_s \omega_{pm}(\omega_\pm^2 - \omega_h^2)/(kB_2\omega_{m2}) \\ 1 \end{bmatrix} = N \begin{bmatrix} i\gamma B_2 \omega_{m2} k/(\omega_\pm^2 - \omega_m^2) \\ \gamma B_2 \omega_\pm k/(\omega_\pm^2 - \omega_m^2) \\ 1 \end{bmatrix}, \tag{2.165}$$

where N is a normalization constant.

Finally, we can identify three different behaviours of equation 2.164, away from the crossing points we have either quasi-elastic or quasi-magnetic regions, and near the crossing points, a magnetoelastic region. In the quasi-elastic region $\omega_\pm \approx \omega_h$, so from equation 2.165, we obtain that $m_x, m_y \approx 0$, and the total energy of the system is dominated by the elastic energy. On the other hand, in the quasi-magnetic region, $u_t \approx 0$, and the total energy is basically the magnetic energy. Near the crossing points, the total energy oscillates between the magnetic and elastic systems.

### Wave propagation parallel to magnetization

Now, for the case in which $\vec{k} \parallel \vec{M}_0$. Here, $\vec{k} = k\hat{z}$, $\theta = 0$, $u_t = u_x$ and $u_l = u_z$. In the absence of magnetoelastic coupling, we would obtain backward volume spin waves

(BVSW), which have dispersion following equation 2.82. In this geometry, we obtain the linearized equations

$$(\omega^2 - \omega_h^2)u_t + i\frac{B_2 k}{\rho M_s}m_x = 0, \tag{2.166}$$

$$(\omega^2 - \omega_v^2)u_y + i\frac{B_2 k}{\rho M_s}m_y = 0, \tag{2.167}$$

$$(\omega^2 - \omega_l^2)u_l = 0, \tag{2.168}$$

$$i\gamma B_2 k u_y + i\omega m_x + \omega_{m2} m_y = 0, \tag{2.169}$$

$$i\gamma B_2 k u_t + \omega_{m1} m_x - i\omega m_y = 0. \tag{2.170}$$

Observe that the longitudinal elastic wave ($u_l$) is not coupled to the magnetization components, and its dispersion relation is simply $\omega = \omega_l = v_\parallel k$. Here, both the transverse in-plane ($u_l$) and out-of-plane ($u_l$) elastic waves are coupled to the magnetic system. The coupled equations can be written as [80]

$$\begin{bmatrix} i\gamma B_2 k & 0 & \omega_{m1} & -i\omega \\ 0 & i\gamma B_2 k & i\omega & \omega_{m2} \\ \omega^2 - \omega_h^2 & 0 & iB_2 k/(\rho M_s) & \\ 0 & \omega^2 - \omega_v^2 & 0 & iB_2 k/(\rho M_s) \end{bmatrix} \begin{bmatrix} m_x \\ m_y \\ u_t \\ u_y \end{bmatrix} = 0. \tag{2.171}$$

Again, the non-trivial solutions are found by obtaining the determinant and equating it to zero. From that we obtain

$$(\omega^2 - \omega_m^2)(\omega^2 - \omega_h^2)(\omega^2 - \omega_v^2) - Jk^2[\omega_{m1}(\omega^2 - \omega_h^2) + \omega_{m2}(\omega^2 - \omega_v^2) + Jk^2] = 0, \tag{2.172}$$

see Figure 2.11. From this equation, we can see that for $J = 0$, we obtain the uncoupled dispersion relations, $\omega = \omega_m, \omega_h$ or $\omega_v$, where $\omega_m = \sqrt{\omega_{m1}\omega_{m2}}$ and $\omega_h = \omega_v = v_\perp k$. Now, for $J \neq 0$, we can see three interaction terms. In the first, $Jk^2\omega_{m1}(\omega^2 - \omega_h^2)$, we can see an interaction between the in-plane transverse elastic wave with the spin wave, which will generate an anticrossing gap between these two curves. The second, $Jk^2\omega_{m2}(\omega^2 - \omega_v^2)$, shows an interaction between the spin wave and the transverse out-of-plane elastic mode, also creating an anticrossing gap. And finally, the third interaction term, $J^2k^4$, couples all the three different waves, generating an interaction among the spin wave and the two transverse components of the elastic wave.

The corresponding eigenstate can be evaluated as [80]

$$\begin{bmatrix} m_x \\ m_y \\ u_t \\ u_y \end{bmatrix} = N \begin{bmatrix} -\rho M_s[\omega_{m2}(\omega^2 - \omega_v^2) + Jk^2]/(B_2 k\omega) \\ i\rho M_s(\omega^2 - \omega_v^2)/(B_2 k) \\ -i[\omega_{m2}(\omega^2 - \omega_v^2) + Jk^2]/(\omega(\omega^2 - \omega_h^2)) \\ 1 \end{bmatrix}. \tag{2.173}$$

Here, the dispersion also generates an anticrossing gap between the two branches, $\omega_+$ and $\omega_-$, where we can identify the three regions: quasi-elastic, quasi-magnetic and magnetoelastic. However, a third magnetoelastic eigenstate is found, $\omega_\sim$, with a dispersion that is almost linear and falls slightly below the uncoupled transverse elastic wave curve.

In conclusion, the total energy of a magnetoelastic system consists of various contributions from the magnetic, elastic, and magnetoelastic interactions. The magnetic energy contribution is determined by dynamic components and can be affected by various magnetic interactions, including Zeeman, dipolar, exchange, and magnetocrystalline interactions. Meanwhile, the elastic wave energy is determined by the displacement components and their time derivatives. The magnetoelastic interaction also contributes to the total energy of the wave, and generates an anticrossing gap in the dispersion relation. During the propagation, the energy oscillates between the different components. Far from the crossing points, the energy is mainly in either the elastic or in the magnetic system. Near the crossing points, it resonantly oscillates between the two systems.

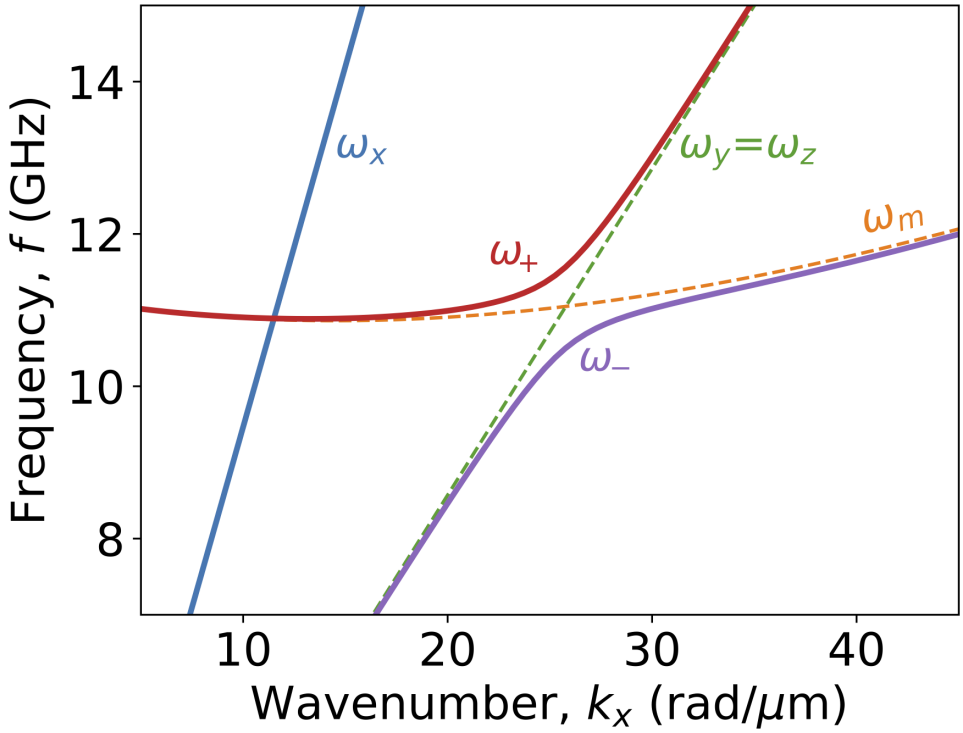


Figure 2.11: The dispersion curves for magnetoelastic waves with magnetization parallel to the wave vector in a 20 nm thick CoFeB film ($M_S = 1.2MA/m$, $A_{ex} = 18pJ/m$, $\rho = 8000kg/m^3$, $C_{11} = 283GPa$, $C_{12} = 166GPa$, $C_{44} = 58GPa$, and $B_1 = B_2 = -8.8MJ/m^3$), obtained from equation 2.172. The plot reveals that the longitudinal elastic wave ($\omega_x$) does not couple to spin waves ($\omega_m$), whereas the transverse elastic waves ($\omega_y$ and $\omega_z$) hybridize and form an anticrossing gap with two branches ($\omega_-$ and $\omega_+$).

# Chapter 3

# Methods

In this section, we will discuss the numerical simulations and the data processing employed in this thesis.

We will start describing the micromagnetic tool employed to numerically solve the magnetization dynamics, the LLG equation, MuMax3 [78], with several magnetic energy terms. This tool supports the inclusion of the magnetoelastic effective magnetic field in the equation, allowing us to determine the spin wave dynamics generated from external elastic strains. However, it does not solve the elastodynamic equation of motion for the material.

To simultaneously compute the coupled elastodynamic and LLG equations we employed the magnetoelastic extension of MuMax3 [96]. In this package we are able to include the elastic properties of the material, along with the magnetic, elastic and magnetoelastic energy terms. This package allows us to calculate the internal elastic modes of the material and also to calculate the magnetoelastic waves, with all the dispersion relations.

## 3.1 Micromagnetic simulations

In this thesis, we employed the open-software GPU-accelerated MuMax3 software [78]. This computational tool utilizes finite-difference discretization to calculate the space- and time-dependent magnetization dynamics in ferromagnets ranging in size from nano- to micro-scale. It obtains the ground state of the magnetic sample by an energy and torque

minimization, as shown in equation 2.8. It also calculates the magnetization dynamics by numerically solving the LLG equation, equation 2.7.

The first step in the simulation is to define the size of the universe to be simulated. To ensure reliable results, it is important that the size of the cells used in the simulation is not larger than the exchange length of the material, $l_{ex} = \sqrt{2A_{ex}/(\mu_0 M_S^2)}$, for example, it is 5.7 nm for permalloy and 7.7 nm for nickel. However, it is worth noting that in thin films, the magnetization can be considered constant along the thickness direction. This allows for the use of cells that are larger than the exchange length in that direction, without compromising the accuracy of the simulation results.

The second step of the simulation involves defining the magnetic parameters of the material, including the saturation magnetization ($M_S$), exchange stiffness ($A_{ex}$), and Gilbert damping constant ($\alpha$). Following this, initial conditions are specified, such as the initial magnetization configuration and the applied external magnetic field vector, which might be time-dependent.

The final step in the simulation code involves specifying the desired output, which can either be the minimum energy magnetic state or the magnetization dynamics. If the minimum energy state is the desired output, the code employs the *relax()* command, which generates a single magnetization file. On the other hand, if the magnetization dynamics are of interest, we use the *run()* command, and the code calculates the dynamics over a specified time interval and outputs a magnetization file for each time-step of the simulation.

In the energy minimization mode of the simulation, the precession term of the LLG equation is disabled. The code first minimizes the energy until the total energy cuts into the numerical noise floor. Then, it begins monitoring the magnitude of the torque instead of the energy, since close to equilibrium the torque will decrease monotonically and is less noisy than the energy. In the dynamic simulation, the LLG equation is solved using Range-Kutta methods with adaptive time steps.

## 3.2 Magnetoelastic extension

The MuMax3 software has been extended to include the physics of elasticity in addition to magnetization [96]. This new feature enables the calculation of both the magnetic and elastic degrees of freedom of the material and the coupling of the two through the

magnetoelastic interaction. By integrating magnetoelastic effects into the simulations, the software offers a more comprehensive model for studying the behavior of ferromagnetic materials under the influence of external fields and mechanical stresses. Moreover, this extension opens up the possibility of investigating magnetoelastic waves.

In this extension, in addition to the magnetic parameters, the elastic properties of the material must also be declared. This includes the stiffness constants, such as $c_{11}$, $c_{12}$, and $c_{44}$, which are relevant for cubic crystal structures, the mass density $\rho$, and a viscoelastic damping parameter $\eta$.

With the addition of the elasticity module in the MuMax3 software, the initial elastic displacement of the material must also be defined in addition to the magnetization. Excitations in the system can be introduced by defining a time- and space-variant body force or strain components. The simulation outputs both the magnetization and elastic displacement for each step, providing a complete picture of the behavior of the material under the influence of external fields and mechanical stresses.

If non-zero magnetoelastic constants are included in the simulation, the software will solve the now coupled equations of motion for both the magnetization dynamics and elastodynamics. Any change in the elastic strains will influence the magnetoelastic effective field, which in turn will affect the magnetization dynamics. Similarly, any change in the magnetization will influence the magnetoelastic body force, which will affect the elastic properties, thus generating a magnetoelastic feedback system.

## 3.3 Processing simulation data

In order to obtain the dynamic properties of either the magnetic or the elastic system, an external pulse can be used as a perturbation to excite the system. This perturbation can take the form of a magnetic field or a body force, which takes the magnetization and/or the elastic displacements out of equilibrium. The dynamics of the system are then saved until it returns to its equilibrium position.

In order to perform the pulsed excitation, we utilize a sinc function, e.g. $H_{ext} = \mathrm{sinc}(\omega_0 t) = \sin(\omega_0 t)/(\omega_0 t)$ with $\omega_0 = 2\pi f_0$, which takes on the form of a step function with cut-off frequency $f_0$ in the frequency domain. This allows for a homogeneous excitation of all eigenfrequencies of the system below $f_0$ when a Fast Fourier Transform (FFT) is

performed. By utilizing this method, we can efficiently and effectively excite the system and analyze the resulting dynamics.

The magnetization dynamics is recorded as $m(x, y, z)$ at each time step. By stacking the time variations for each cell, we obtain $m(t, x_0, y_0, z_0)$, where $(x_0, y_0, z_0)$ is the position of the cell in the sample. We then analyze the dynamics of the system by performing the FFT of the time-domain signal for each cell of the sample, resulting in the frequency-domain signal $\tilde{m}(f, x_0, y_0, z_0)$, where $\tilde{m}$ is the amplitude of the magnetization at the corresponding frequency. Summing the results from every cell, we obtain the frequency spectrum, $\tilde{m}(f)$, which contains the amplitude of the magnetization for the whole sample as a function of the frequency. The peaks that appear in the frequency spectrum correspond to the eigenfrequencies of the system. These peaks are typically Lorentzian in shape and provide information about the resonant frequencies of the system.

In the study of wave phenomena, such as spin waves, it is useful to analyze the spatial propagation of waves in addition to their temporal behavior. To achieve this, we stack the magnetization time variations for each line, rather than each cell, e.g. in the x-direction, resulting in the expression $m(t, x, y_0, z_0)$. A 2D FFT is then performed along both the x and t axes. The resulting graph in the Fourier domain shows both the frequency and the wavenumber along x, expressed as $\tilde{m}(f, k_x, y_0, z_0)$. Summing all signals, we obtain $\tilde{m}(f, k_x)$, which displays the amplitude for each $(f, k_x)$ point. The amplitude peaks in the $f$ vs. $k_x$ plot correspond to several resonance peaks that form continuous curves. These curves correspond to the dispersion relations, and they provide crucial information on the propagation of waves in the material.

# Chapter 4

# Results and Discussion

In this chapter, we will present the main results and discussions of our thesis, which is focused on the dynamics of magnetoelastic coupling. This area of research has gained considerable interest in recent years due to its potential applications in spintronic and magnonic devices. Specifically, we explore three different scenarios in which the magnetoelastic interaction plays a crucial role in determining the dynamics of the system.

Firstly, we present the simulation results of spin wave excitation and spin pumping that is driven by external elastic waves [97]. The simulation is performed in MuMax3 [78] by applying an external wave-like strain and solving the Landau-Lifshitz-Gilbert equation, considering the magnetoelastic effective field that arises from the strain.

Secondly, we aimed to replicate the experimental findings reported by Holanda et. al 2018 [59]. Using the magnetoelastic extension [96] of MuMax3, we simulated the magnon-phonon interconversion under a spatially varying magnetic field. Specifically, the wave was excited in the quasi-magnetic region of the dispersion, and as it propagated in the varying field, it continuously changed its wavenumber until reaching the magnetoelastic regime, and then eventually entering the quasi-elastic regime. The simulation results reveal a similar conversion of the quasi-magnetic wave to a quasi-elastic wave, similar to what was observed in the experimental study.

Finally, we investigate the elastic and magnetic waves that propagate in a complex magnetic structure, the Néel domain walls, again by solving the coupled LLG equation and the elastodynamics [98]. We obtain the dispersion relation and compare it with analytical

equations. We discuss the formation of an anticrossing gap in the dispersion relation based on the symmetry of the modes.

## 4.1 Spin waves and spin pumping driven by elastic waves

This first simulation aims to investigate the spin-wave propagation across long Ni stripes under the influence of an external elastic wave. To perform this analysis, micromagnetic simulations using MuMax3 [78] software were carried out. The external elastic waves were modelled as propagating wave-like strains, which were included in the LLG equation as effective magnetoelastic fields. In addition, the acoustically-driven spin pumping was also studied in this simulation by calculating the spin and charge current maps at a Ni/Pt interface and in the Pt layer, respectively, and the AC and DC voltages on the Pt layer using the Inverse Spin-Hall effect (ISHE). The simulation results have been previously published and are available in [97].

In this simulation, the aim is to replicate an experimental setup where surface acoustic waves are generated by interdigital transducers (IdTs) on a piezoelectric substrate with a magnetoelastic stripe deposited on top [66–71]. Specifically, the acoustic wave is generated in the piezoelectric material by applying an alternate tension to the IdTs. The elastic wave then propagates towards the magnetic strip, driving its magnetization dynamics, which can be electrically detected in a Pt layer deposited on top of the magnetic material by means of the inverse spin Hall effect (ISHE) voltage [81, 85, 86, 89].

### 4.1.1 Introduction

In magnon spintronics, the propagation of magnons over large distances is critical to enable the processing of spin flux or information. In this study, we investigate the spin-wave propagation in narrow Ni stripes driven by acoustic excitation, by means of micromagnetic simulations.

We have considered different cases depending on the extension of the acoustic wave propagation, which is generated on the left end of the stripe. When acoustic waves are confined at the origin, the spin waves are free to propagate but vanish after the decay

length, that is dependent on the dissipation. On the other hand, when the acoustic waves are present in the whole stripe, spin and acoustic waves propagate together with the spin-wave maintaining the amplitude constant. Images of the spin-wave propagation modes and the dispersion relations are discussed for different acoustic wave attenuation lengths.

To investigate the acoustic-driven spin pumping effect, we also consider a Pt line over and crossing the Ni stripe, as in recent experiments. We calculate the spin and charge current maps at the Ni/Pt interface and in the Pt layer, respectively, as well as the AC and DC components of the inverse spin Hall effect voltage.

Although significant efforts have been made to develop experimental procedures for obtaining high-quality IDTs, micromagnetic simulations provide a reliable tool for a deeper understanding of the dynamics involved in spin-wave propagation driven by acoustic waves. Through our simulations, we have gained insight into the magnetization dynamics and spin-wave propagation on long Ni stripes and the acoustic-driven spin pumping effect.

### 4.1.2 Simulation setup

We considered stripes as 8192 nm long, 512 nm wide and 10 nm thick. The following parameters were used to match Ni parameters: saturation magnetization $M_S = 490$ kA/m, exchange stiffness $A_{ex} = 5$ pJ/m, and the magnetoelastic coupling constants $B_1 = 6.2$ MJ/m and $B_2 = 4.3$ MJ/m. The cell size is $4 \times 4 \times 10$ nm$^3$. The Gilbert damping $\alpha$ was set to 0.001. To avoid spin-wave reflection by the edges one considers a narrow area near the edge as an absorbing boundary condition, $\alpha$ is gradually increased from 0.001 to 1. The magnetocrystalline anisotropy was disregarded for simplicity.

The acoustic and spin-wave propagation on a ferromagnetic Ni stripe were modelled in three different attenuation scenarios. In the first, the strain excitation is strongly attenuated being produced and restricted at one end of the stripe (on the left). In the second, the acoustic waves are not attenuated and propagate along the whole stripe. In the last, the acoustic waves are partially attenuated with an exponentially-decaying amplitude along the propagation length to simulate a real situation. Figure 4.1 illustrates these three scenarios, respectively.

The magnetization dynamics and spin waves are induced by applying a propagating non-uniform longitudinal strain $\varepsilon_{xx} = \varepsilon_0 sin(kx - \omega t)$ where $\omega = vk$, with $v$ being the

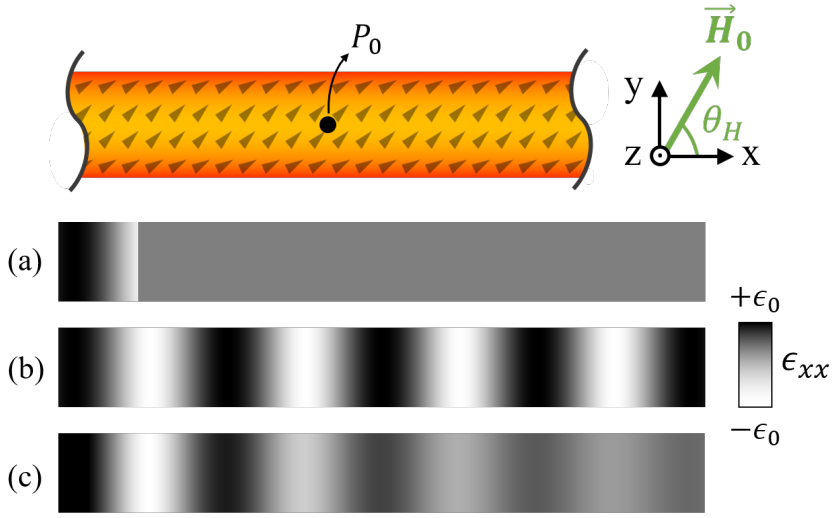


Figure 4.1: The simulation setup. A Ni stripe with a equilibrium magnetization at $\theta = 45^0$ with the $\hat{x}$-axis under a magnetic field $\vec{H}_0$ applied at a $\theta_H$ angle. Below, we show the elastic excitation applied for three cases: (a) high attenuation, (b) no attenuation, and (c) intermediate attenuation.

acoustic wave Rayleigh velocity, which we assumed to be $v = 4000$ m/s in our simulations. Thus, the magnetoelastic term reduces to the $x$-component, $\vec{H}_{ME} = -2B_1 m_x \varepsilon_{xx}/(\mu_0 M_S)\hat{x}$.

### 4.1.3 Results: Spin wave propagation modes

First, a static 31.5 mT magnetic field is applied at the angle $\theta_H$, and the magnetization relaxes to the minimum energy at the angle $\theta$, both angles are defined relative to the $\hat{x}$-axis. An acoustic excitation $\varepsilon_{xx} = \varepsilon_0 sin(kx - \omega t)$, with $\varepsilon_0 = 10^{-5}$, $f = 2GHz$ ($\omega = 2\pi f$), and $k = 6.28\mu m^{-1}$ ($\lambda = 1\mu m$), is applied to the whole stripe during 25 ns, and the magnetization is saved. A spatial FFT of the magnetization is calculated, and then, the FFT amplitude as a function of the magnetization angle $\theta$ is obtained, as can be seen from Figure 4.2a.

Note that the spin wave amplitude ($\delta m_z$) vanishes when the magnetization is either parallel or perpendicular to the acoustic wave propagation direction ($\hat{k} = \hat{x}$), and reaches a maximum when the magnetization is at $45^o$, 135, $225^o$, and $315^o$. This can be understood

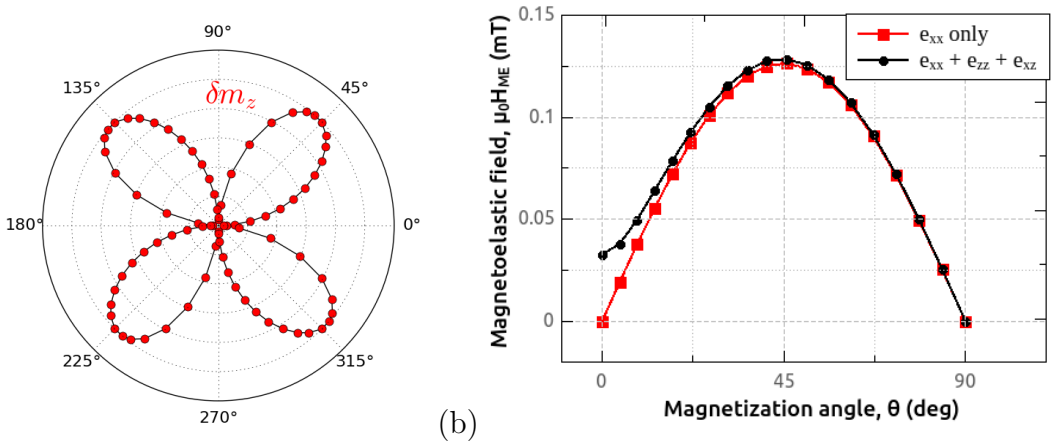


Figure 4.2: (a) Polar plot of the spatial-FFT amplitude of the spin waves at the wave vector of the acoustic wave as a function of the magnetization angle ($\theta$) under a longitudinal strain excitation ($\varepsilon_{xx}$). (b) The AC magnetoelastic field intensity perpendicular to the static magnetization ($\mu_0 H_{ME}$) under different $\theta$ values for the pure longitudinal strain ($\varepsilon_{xx}$) and for the more complete SAW excitation ($\varepsilon_{xx}$+$\varepsilon_{zz}$+$\varepsilon_{xz}$). They both have a maximum at $45^o$, with similar amplitudes, and only significantly differ at $\theta = 0$.

by applying the rotated coordinate system (u,v,z) in the magnetoelastic effective field (Equation 2.117) to the magnetization $\vec{m_0} = m_u\hat{u}$ using the coordinate transformation $m_x = m_u cos\theta$ and $\hat{x} = cos\theta\hat{u} - sin\theta\hat{v}$. One obtains, thus, $\vec{H}_{ME} \propto (m_u cos\theta)(cos\theta\hat{u} - sin\theta\hat{v})$, and the dynamical part of the the magnetoelastic field ($\vec{h}_{RF}$) is,

$$\vec{h}_{RF} = \frac{2B_1 m_u \varepsilon_{xx}}{\mu_0 M_S} sin\theta cos\theta\ \hat{v}, \tag{4.1}$$

which is zero at $\theta = n\pi$, and is at its maximum amplitude for $\theta = 45^o + 90^o n$ ($n$ is an integer), as obtained in Figure 4.2a. So, in order to maximize the magnetoelastic excitation of spin waves we have fixed the magnetization angle at $\theta = 45^o$ in all simulations.

However, a more realistic description of a Rayleigh-type SAW should contain the components $\varepsilon_{xx} = \varepsilon_0 sin(kx - \omega t)$, $\varepsilon_{zz} = -\varepsilon_0 sin(kx - \omega t)$ and $\varepsilon_{xz} = (3/8)\varepsilon_0 sin(kx - \omega t)$ [99]. As the strain acts as an AC excitation this provides an out-of-plane component for the RF magnetic field but keeping almost the same angular dependence to the magnetic oscillation, see Figure 4.2b. It exhibits a maximum at $45^o$ and at this angle the simulations produce the same results as taking all components. Thus, for the sake of simplicity, we have used

only the $\varepsilon_{xx}$ component of the strain without any loss to the results and discussion, as also considered in references [64, 67].

### Strongly attenuated acoustic wave

Next, we investigate the role played by the elastic excitation in the magnetization dynamics considering that the acoustic waves are confined to a small region of the Ni stripe (see Figure 4.1a). In experiments it should correspond to strongly attenuated SAWs, propagating along the stripe long direction (x), that vanish nearby the excitation area.

Keeping the magnetization of the Ni stripe at $45^o$, pointing to the $\hat{u}$ direction, the acoustic waves with a given wave number $k_x$ and frequency $f = vk_x/2\pi$ give rise to spin waves. Figure 4.3a shows a snapshot of the spin-wave at a given instant, the wave front is tilted and propagates towards the $\hat{x}$ direction.

The spin-wave propagates with the same frequency but not with the same wave number as the acoustic excitation. In the excitation area they have the same wave number but when the spin-wave enters in the Ni stripe it changes to its natural propagation mode, according to the frequency and the total effective field. For the sake of example, in the snapshot shown in Figure 4.3a the wave number of the spin-wave obtained from the fast Fourier transform (FFT) is 23.8 $rad\ \mu m^{-1}$ ($\lambda = 264$ nm) while for the acoustic excitation it is 9.4 $rad\ \mu m^{-1}$ ($\lambda = 667$ nm).

To understand this behaviour, we simulated the wave propagation varying the frequency and maintaining fixed the excitation wave number at $k = 2\pi f/v$. As can be seen from Figure 4.3b, the dashed line represents the excitation $k$ but the generated spin-wave has a different $k$ according to the field, like a dispersion relation. A minimum threshold value for the frequency close to 5.5 GHz is observed, below it there is no spin-wave and for high $k$-values the dispersion relation exhibits a quadratic behaviour. The presence of several modes are justified by the lateral wave confinement.

The dispersion relation of free spin waves in magnetic lines [92, 100–103] were calculated and compared with our simulations. They are shown in Figure 4.3b, see the blue dotted lines. The calculation that better correspond the simulation data was performed using $w_{eff} = 0.7w$, $\mu_0 H = 55$ mT and $\theta_M = 35^o$. The fact that $\mu_0 H$ and $\theta_M$ are not 60 mT and $45^o$, respectively, is probably due to the complex shape of the demagnetizing field, because the static magnetization is not at the symmetry axis of the magnetic slab. However, as

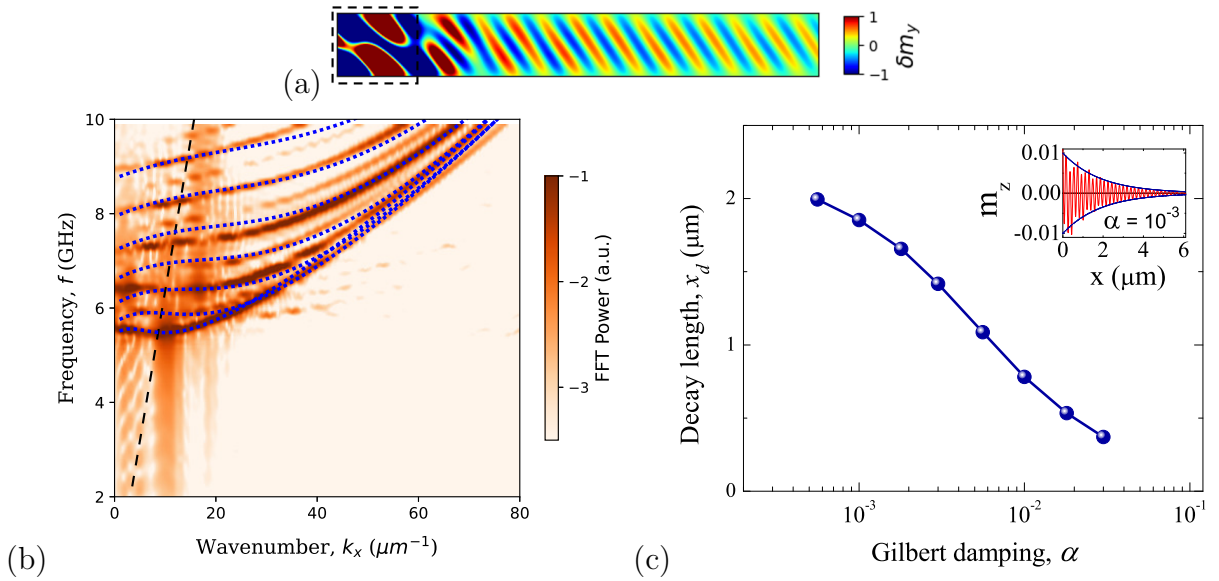


Figure 4.3: Strongly attenuated acoustic wave. (a) The magnetization profile of the spin-wave generated by a $f = 6$ GHz and $\lambda = 667$ nm acoustic excitation restricted to the dashed region under a 60 mT field. (b) The dispersion relation under a 60 mT field. The dashed line is the acoustic excitation wave number $k = 2\pi f/v$. The blue dotted lines represent data calculated from an analytical model. (c) The exponential decay length ($x_d$) of the spin-wave. The inset shows the z-magnetization along the x-axis with its exponential decaying amplitude for $\alpha = 10^{-3}$.

can be seen from Figure 4.3b, dotted lines are in good agreement with simulations for the small and large $k_x$ ranges, and it is still better for the first modes.

Now, taking in mind that dissipation is present on the magnetization dynamics, a central question is how long can the spin waves propagate. From images like the one in Figure 4.3a, taking the amplitude along the stripe is possible to probe the amplitude attenuation. As shown in the inset of Figure 4.3c, the magnetization decay can be fitted by an exponential dependence $m_y = m_0 cos(kx)e^{-x/x_d}$, where $x_d$ is the decay length. Figure 4.3c shows the decay length as a function of the Gilbert damping, which follows a logarithm decay [104].

For low $\alpha$, say, below 0.001, the wave decay length is close to 2 $\mu m$ which is a length scale quite big to transport digital information in devices. Low values like this is found

in yttrium iron garnet ($Y_3Fe_5O_{12}$). On the other hand, for more dissipative materials with alpha reaching 0.01 the decay length becomes close to 1 $\mu m$, which still might be sufficiently large for practical applications.

### Non-attenuated acoustic wave

Now, we simulate the case in which the acoustic wave has no attenuation, so the strain $\varepsilon_{xx}$ propagates with constant amplitude along the whole stripe (see Figure 4.1b). This should correspond to the situation where the acoustic wave attenuation length is much larger than the stripe length [77], thus, acoustic and spin waves propagate together on the stripe.

Figure 4.4a shows a typical image of the spin-wave. As mentioned above, a bias magnetic field is applied to keep the magnetization at $45^o$. Nevertheless, different from the previous case where the wave front is tilted, here, the wave front is closer to the pattern of the strain excitation.

The generated spin-wave has the same frequency and wave number as the acoustic excitation (see Figure 4.4b). As can be seen from this figure, for a large range of frequencies the main peak for the spin-wave propagation is observed at $k = 2\pi f/v$ (dashed line). The dispersion relation modes are also present but in lower intensity. It is interesting to note that for free spin waves (previous case) an acoustic excitation at 1 GHz is not a natural mode for spin waves, as shown in the dispersion relation (see Figure 4.3b), however, here, the non-attenuated excitation drives and then matches the spin-wave propagation to its frequency, irrespective to the frequency, although, some dependence on frequency is observed.

Figure 4.4c highlights this behaviour in further details through the dispersion relation as a function of the external magnetic field ($\mu_0 H$). Non-zero FFT power modes are seen on all frequencies and fields, because the non-attenuated acoustic wave excites the corresponding spin-wave with same frequency and wave number. Nevertheless, some curves can be observed, meaning the existence of resonance propagation modes. This implies that although spin waves can be excited by SAW in practically any frequency and wavelength, their amplitude is resonantly enlarged when the acoustic wave matches the frequency and field of its natural dispersion modes.

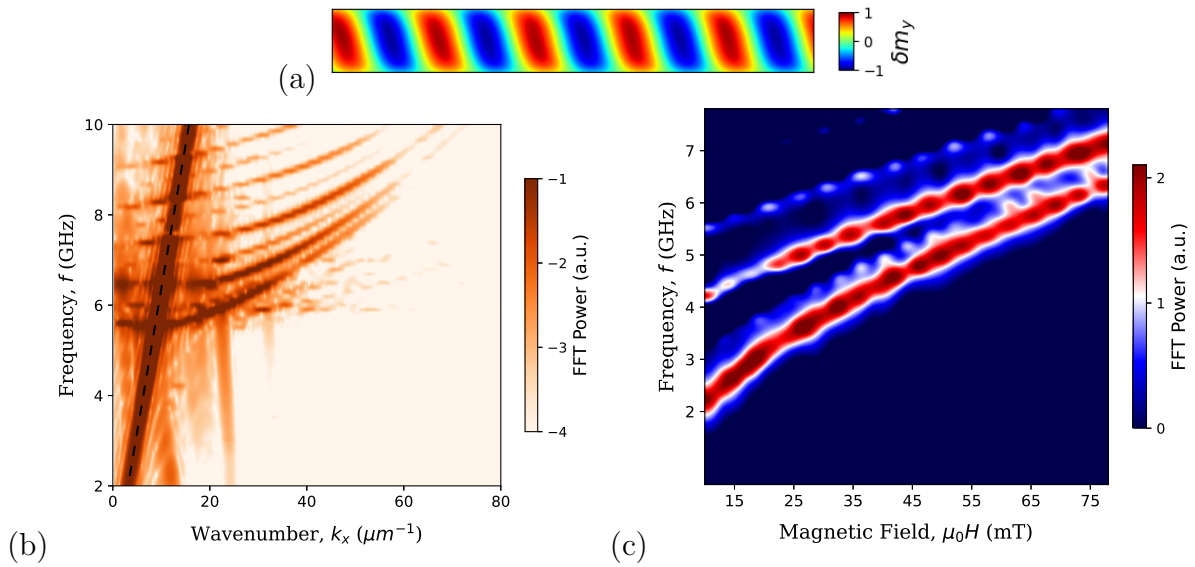


Figure 4.4: Non-attenuated acoustic wave. (a) Magnetization profile of spin waves excited by propagating acoustic waves with frequency and wavelength as 5 GHz and 800 nm, respectively. (b) The Fourier amplitude of the spin waves for different frequencies. In all cases the main peak coincides with the acoustic wave number (dashed line). (c) FFT power of the excited spin wave as a function of the external magnetic field for waves with frequency $f$ and wave number $k = 2\pi f/v$.

### Partially attenuated acoustic wave

Different from the two previous limit cases, we now consider acoustic waves with an intermediate attenuation. It means that the acoustic waves propagate the whole sample but their amplitude exponentially decay along the stripe, $\varepsilon_{xx} = \varepsilon_0 sin(kx - \omega t)e^{-x/x_d}$, where $x_d$ is the acoustic wave decay length.

Let us see what happens to the spin-wave propagation varying $x_d$, remembering that the stripe is 8.19 $\mu m$ long, see Figure 4.5b. We use the frequency and elastic wave number as $f = 4$ GHz and $k = 6.28$ $\mu m^{-1}$ ($\lambda = 1$ $\mu$m), respectively, under a 20 mT magnetic field. For $x_d = 2$ $\mu m$ the FFT of the spin-wave exhibits a peak at 6.28 $\mu m$, the same of the acoustic excitation, meaning that the acoustic excitation acts as dominant over the spin-wave propagation.

The same behaviour is observed for any $x_d$ larger than 2 $\mu m$. Decreasing $x_d$ to 1 $\mu m$ a

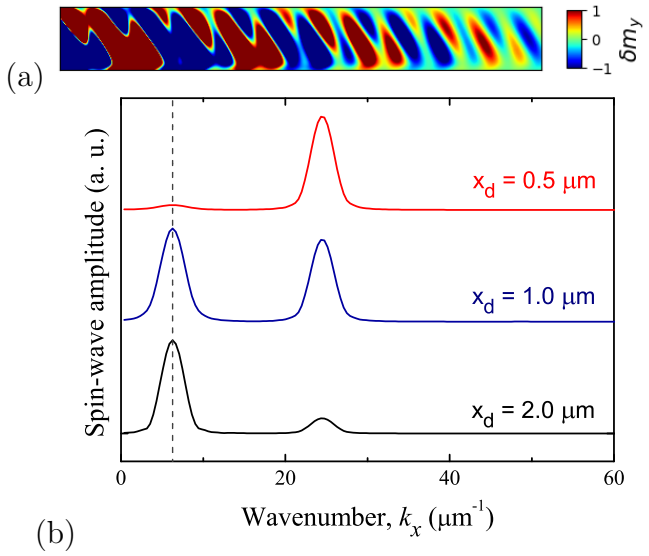


Figure 4.5: Partially attenuated acoustic wave. (a) The spatial magnetization profile for an exponentially attenuated acoustic excitation with decay length $x_d = 1\ \mu m$, $f = 4$ GHz and $\lambda = 1\ \mu m$ under a 20 mT magnetic field. The spin-wave transits between the excitation wavelength of 1 $\mu m$ (left) to its natural wavelength value of 256 nm at that field (right). (b) The spin-wave FFT amplitude for different attenuation decay length values $x_d$. The vertical dashed line corresponds to the excitation wave number ($k = 6.28\ \mu m^{-1}$).

second peak is observed (24.5 $\mu m^{-1}$), suggesting the coexistence of two waves. It is shown in Figure 4.5a, where two waves can be seen, one closer to the excitation origin and the other at the end of the stripe, but each one with a different wave number. Decreasing $x_d$ still further, say to 0.5 $\mu m$, only one peak is observed (Figure 4.5b). It turns out that a regime of spin waves propagation free of the acoustic excitation becomes dominant.

### 4.1.4 Results: Spin pumping and inverse spin Hall effect (ISHE)

So far we simulated the spin-wave propagation modes in Ni stripes induced by elastic excitation under different conditions. It is not a friendly task to measure spin waves in real experiments, so taking it in mind we simulate what should be easier for experimentalists, the measurement of voltage in narrow Pt lines crossing the Ni stripe through the ISHE, see section 2.2.3. To do that, we simulate the spin current map at Ni/Pt interface and

the charge current map in the Pt layer, and then the AC and DC ISHE voltages. We deal with the non-attenuated case only, but the results are qualitatively equivalent irrespective of the acoustic attenuation level.

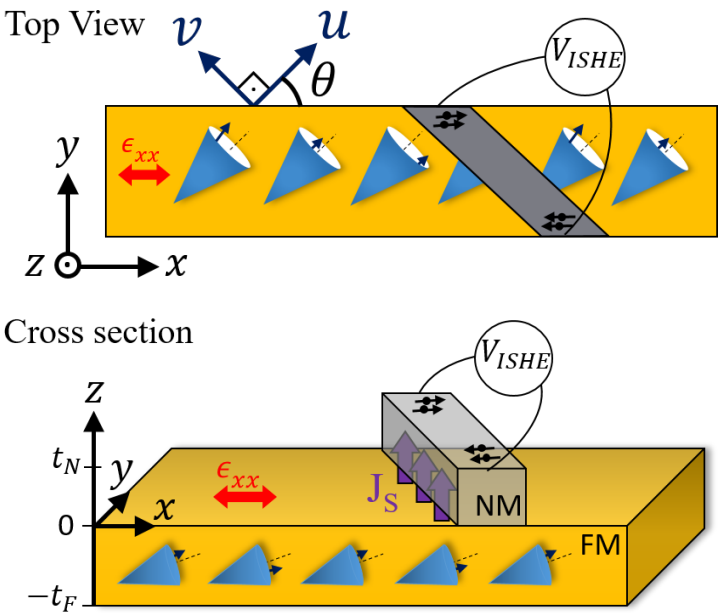


Figure 4.6: FM/NM (Ni/Pt) bilayer. The strain waves ($\varepsilon_{xx}$) excite the magnetization dynamics of the FM film which, in turn, leads to the generation of a spin current ($\vec{J}_S$) across the film plane. This acoustically driven spin current injected in the NM layer is converted into a charge current, $\vec{J}_C$, by the ISHE and can be detected as electric voltage ($\Delta$V) at the top of the NM line.

We simulate the time evolution of the reduced magnetization components ($m_x$, $m_y$, and $m_z$) for an elastic excitation with $f = 4$ GHz and $\lambda = 1$ $\mu$m under resonance condition. The applied field is $\mu_0 H_0 = 31.5$ mT, and the Gilbert damping was set to $\alpha = 0.004$, according to experimental values for the Ni/Pt bilayer [105].

Considering the magnetization is pointing to $45^o$ relative to $\hat{x}$-axis, to maximize the magnetoelastic effects, it is useful to use a $\theta = 45^o$ rotated coordinate system ($\hat{u}, \hat{v}, \hat{z}$) around the $\hat{z}$-axis, see Figure 4.6. As can be seen from Figure 4.7a, in this new coordinate system the $m_v$ and $m_z$ components exhibit sinusoidal behaviour, with a $90^o$ delay between them, following the dependence $m_u = m_{0v} cos(\omega t)$ and $m_z = m_{0z} sin(\omega t)$. This is highlighted in

the inset of Figure 4.7a showing the Lissajous curve with an elliptic motion with a factor $p = m_{0z}/m_{0v} = 0.256$. This curve is not circular because Ni layer is thin, 10 nm thick, forcing the in-plane magnetization.

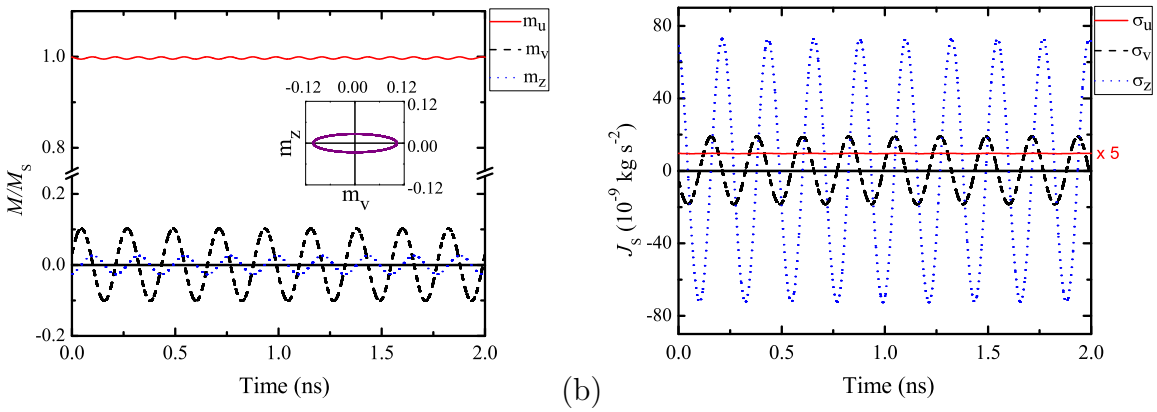


Figure 4.7: Spin-current in point $P_0$. (a) Time evolution of the rotated magnetization components. The inset shows the ellipsoidal motion of $m_v$ and $m_z$ around the equilibrium position. (b) The spin-current across the Ni/Pt interface generated by the spin-wave propagation. The components with v- and z-polarization are AC, with null average value, whereas the u-polarized component exhibit a constant value.

Next step is the spin current $J_s$ calculation at the Ni/Pt interface. It was evaluated from Equation 2.46 using the values extracted from Ref. [105]: $\theta_{SH} = 0.0067$, $g_{eff}^{\uparrow\downarrow} = 3{\times}10^{18}\mathrm{m}^{-2}$, $\sigma_N = 2.42{\times}10^{6}(\Omega m)^{-1}$ and $\lambda_{SD} = 10\mathrm{nm}$. Figure 4.7b shows the spin-current with $v$ and $z$ polarization oscillates whereas the $u$-polarized component exhibits a small but constant value.

We calculated the spatial profile of the spin-current $J_s$ along the stripe for a fixed instant of time by using Equation 2.46 in each point at the Ni/Pt interface (see Figure 4.8). Again, the u-polarized spin current strength exhibits a uniform level, whereas in $v$ polarization it oscillates with the same wavelength and frequency as the spin-wave. Using the $J_s$ map we calculate the $J_c$ map. Still in this Figure 4.8, it is shown in the black frame the charge current $J_c$ in the Pt line calculated by means of Equation 2.50. It illustrates the map of $J_c$ on the $u$ and $v$ components, which are AC and DC components, respectively.

With $J_c$, the voltage ($\Delta V_{ISHE}$) between the opposite ends of the Pt line is calculated, see Figure 4.6 by means of Equation 2.52. We have considered a Pt stripe with thickness

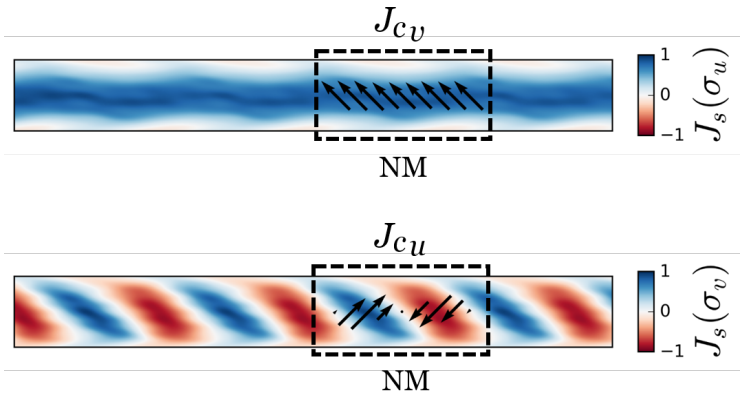


Figure 4.8: Spin and charge current maps. Spin-current ($J_s$) colormap across the ferromagnet for, respectively, the $\hat{u}$ and $\hat{v}$ spin-polarization directions at a given instant of time (for details see text). The charge current ($J_c$) components in the Pt line are shown as vectors inside the dashed frame.

$t_N = 10$ nm and length covering the Ni stripe as $\ell = 724$ nm, in the two different cases: when the Pt line is aligned to the magnetization direction ($\hat{\ell} = \hat{u}$), and perpendicular to it ($\hat{\ell} = \hat{v}$).

In Figure 4.9a it can be seen that when the Pt stripe is aligned perpendicular to the magnetization ($v$-direction) a DC component is observed, whereas an AC component is found when the stripe is parallel to it ($u$-direction), as expected from Equations 2.53 and 2.54. The DC voltage component value is 2.9 nV and the amplitude of the AC voltage component is 37.3 nV (see Figure 4.9a). From those equations we calculate the ratio between them as $V^{AC}/\Delta V^{DC} = m_{0v}/m_{0u} = 37.3/2.9 = 13$, where $m_{0v}$ and $m_{0u}$ are the amplitude of the AC voltage and the DC value, respectively. These AC and DC ISHE-voltage values including the ratio between them are in quite good agreement with experimental data recently reported [91]. Wei et al. have measured NiFe/Pt stripes 5 x 400 $\mu m^2$ large, and found 12 to the AC to DC ISHE-voltage ratio that is very close to our findings [91]. However, as we will see below this ratio actually depends on the $\varepsilon_{xx}$ strength.

Under the same acoustic excitation ($f = 4$ GHz and $\lambda = 1$ $\mu$m), the resonance on the spin-wave propagation mode also manifests itself by varying with the applied magnetic field (see Figure 4.9b). These resonance peaks can in experiments be measured in both AC

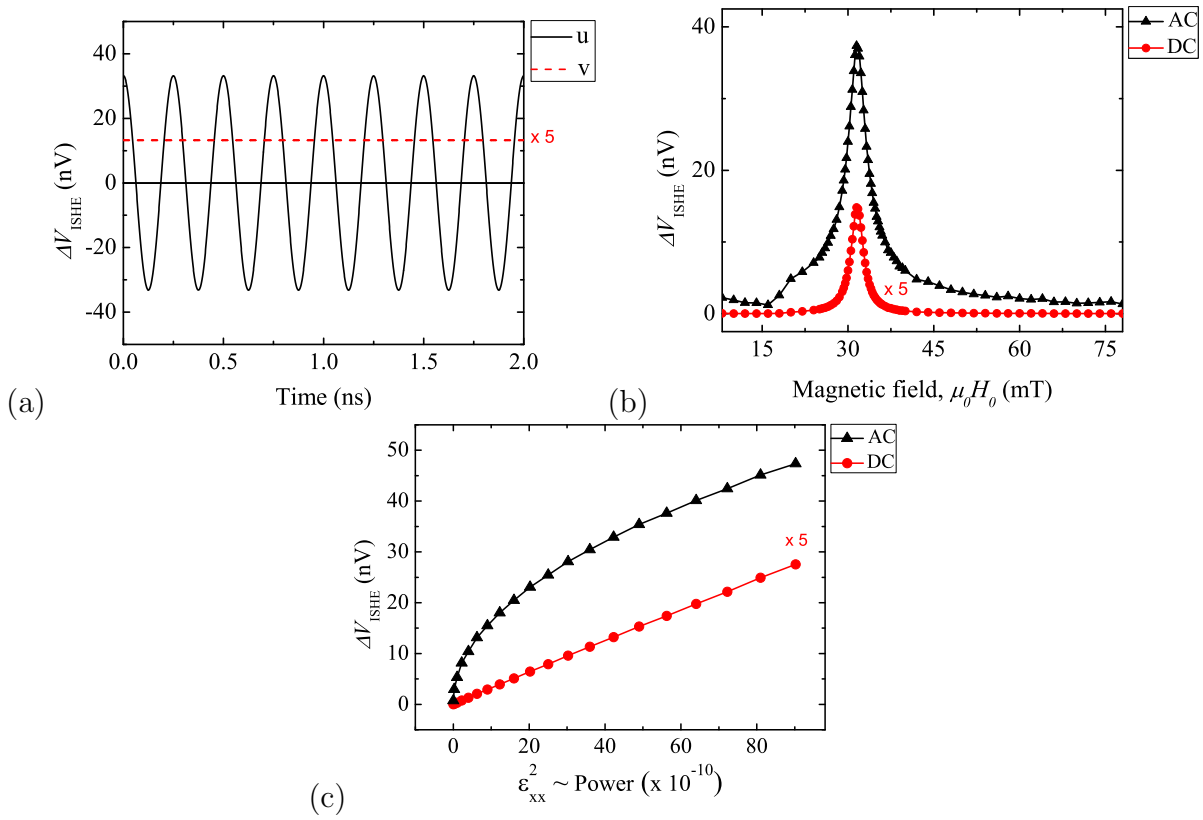


Figure 4.9: ISHE voltage in NM layer. (a) The AC and DC components of the ISHE voltage for a 4 GHz, 1 $\mu$m acoustic excitation. (b) The DC value and AC amplitude as a function of the external field, presenting a resonance peak around the natural dispersion eigenmode. (c) $\Delta V_{ISHE}$ as a function of the square of the strain amplitude ($\varepsilon^2_{xx}$), which is proportional to the acoustic wave excitation power (P), showing a linear behaviour for the DC component and a $\sqrt{P}$ behaviour for the AC amplitude (see text for details).

and DC geometries by tuning the applied field in ISHE-voltage measurements.

An interesting outcome from our simulations is the dependence of the ISHE-voltage with the amplitude of acoustic excitation $\varepsilon_{xx}$. As can be seen from Figure 4.9c, the AC and DC ISHE-voltages follow different behaviours, the DC component is proportional to the excitation power ($\varepsilon^2_{xx}$), i.e., $\Delta V^{DC} \propto P$, while the AC component is proportional to its square root, $\Delta V^{AC} \propto \sqrt{P}$. It can be explained by means of the relation between the magnetization amplitude components under precession and the dynamic effective field

($h_{RF}$), that acts on it using the Polder susceptibility tensor $\vec{m} = \hat{\chi}\vec{h}$. Thus, one obtains $m_{0v}, m_{0z} \propto \varepsilon_{xx}$ and $m_{0u} \approx cte$, that when inserted into Equations 2.53 and 2.54, we obtain $\Delta V^{DC} \propto \varepsilon_{xx}$ and $\Delta V^{AC} \propto \varepsilon_{xx}^2$. Indeed, the AC and DC ISHE-voltage ratio is then proportional to $\varepsilon_{xx}$, meaning that besides the fact that AC component is larger than the DC component, it becomes still more intense increasing the excitation amplitude. Such dependence of $\Delta V^{AC}$ and $\Delta V^{AC}$ with the input power is in full agreement with experimental data reported by Wei et al. (see Fig.3b of Ref. [91]).

### 4.1.5 Discussion

Experiments performed through synchrotron techniques in Ni films deposited on a piezoelectric substrate ($LiNbO_3$) were recently reported, where the elastic waves were probed by time and spatially resolved photoemission electron microscopy (PEEM), and the magnetic contrast by X-ray magnetic circular dichroism (XMCD) [77]. Two interdigital transducers distant 6 mm were employed to generate propagating and standing waves, when one or the two IDTs are used, respectively. According to the authors, firstly, as can be seen from Figure 2b of this reference, the acoustic and spin waves move together. Second, from Figure 2c, also from this reference, one sees that the spin-wave maintain its amplitude constant in a window 45 $\mu m$ wide, placed around 2.5 mm far from the one IDT. Taking it into account and the fact that stand waves can be formed, which is resulted from waves travelling from both IDTs, it is quite reasonable to suppose that the acoustic waves propagate over the whole 6 mm of the Ni film. Thus, one can state that their experiments correspond to the non-attenuated acoustic wave approximation in our simulations (see Figures 4.4a and 4.4b).

Concerning the angle dependence of acoustic spin pumping, Puebla et al. [89] have reported data showing that the voltage generated by the spin pumping follows a sinusoidal function with a maximum at $45^o + 90^o n$, where $n$ is an integer. This angle is defined by the magnetization and $\varepsilon_{xx}$ directions. Besides to verify it we showed that when the pad contacts are aligned at $135^o$ or $45^o$ one measures the DC or AC ISHE-voltages, respectively. The contacts are placed at a narrow Pt line crossing the Ni stripe. On the other hand, Puebla2020 placed the contacts along the $\hat{x}$ direction at the ends of the stripe. It provides directly $(V_{AC} + V_{DC})cos(45^o)$, mixing the AC and DC components. However, it has the advantage to increase a lot the signal level because the interception area between Ni and Pt (or other materials) is much larger than using a crossing narrow line. If we are dealing

with other shapes instead of stripes like big squares in millimeter scale, for example, we can always play with the contact pad orientation to obtain the best result.

### 4.1.6 Conclusions

In this study, we examined the spin-wave propagation in narrow Ni stripes driven by acoustic waves. Our simulations considered three different scenarios based on the propagation of the acoustic wave and its effect on the spin-wave decay length. We found that when the acoustic wave is concentrated at one end of the Ni stripe, the spin-wave is able to propagate freely, but not beyond a distance of 2 $\mu m$, even with a small $\alpha$ damping of $5 \times 10^{-4}$. Conversely, when the acoustic wave propagates over the whole Ni stripe, which can be several millimeters in real systems, the spin waves are carried by the acoustic waves with the same wavelength, also propagating over millimeter scales.

We also investigated the possibility of probing the spin-wave propagation through voltage measurements, specifically by the ISHE voltage. Our simulations provided insight into the optimal placement of contact pads to measure the AC and/or DC components in stripes and films. Additionally, we obtained spin and charge current maps at the Ni/Pt interface and on the Pt line, respectively, which help to further understand the AC and DC acoustic-driven spin pumping effect. Overall, our findings contribute to the understanding of the dynamics involved in the acoustic-driven spin pumping effect, and highlight the utility of micromagnetic simulations in this area.

## 4.2 Magnon-phonon interconversion in a spatially non-uniform field

This section aims to investigate the interconversion between spin waves and elastic waves in materials with magnetoelastic interaction, inspired by the experimental setup performed by Holanda et al. [59].

In materials exhibiting strong magnetoelastic coupling, a dispersion relation of spin waves and elastic waves forms an anticrossing gap, resulting in two branches, see Section 2.5. These branches contain distinct regions where either the spin wave (quasi-magnetic) or elastic wave (quasi-elastic) dominates, and an intermediate region, near the anticrossing gap, where both excitations are of the same magnitude (magnetoelastic).

If a spin wave is excited in the quasi-magnetic regime and the external magnetic field varies spatially during propagation, the wave number of the excitation gradually changes due to energy conservation. By choosing appropriate magnetic field values, it is possible to make the excitation passes through the magnetoelastic region and ends up in the quasi-elastic regime, effectively converting a spin wave (quantized as magnons) into elastic waves (phonons).

The results obtained from these simulations are not novel and are not intended for publication. However, this was our first time working with this extension, and we used it as a way of confirming that it agrees with the theoretical predictions and experimental results.

### 4.2.1 Introduction

The interaction between magnetic and elastic properties of materials has become an area of great interest in the field of magnon spintronics or magnonics [2, 11]. One area of particular interest is the coupling between spin waves and elastic waves, which has been explored from fundamental aspects of their hybridization [57, 58] to the development of memory devices [62, 63] and the potential use of propagating surface acoustic waves (SAWs) to excite spin dynamics in magnetoelastic films in a less power-consuming manner [26, 64, 65]. One of the most fascinating aspects of this coupling is the transfer of spin angular momentum between quasiparticles, which has been investigated in numerous studies, such as the work done in Holanda et al. [59].

We employ the magnetoelastic extension [96] of Mumax3 to study the interaction between elastic and magnetic waves in a CoFeB thin film. We calculate the magnetic and elastic dispersion curves and observe the variation of the wave number as a function of the external magnetic field. Using this information, we create a scenario where an excitation is generated in the quasi-magnetic regime and propagates to the quasi-elastic regime, gradually changing its wave number as the field decreases.

### 4.2.2 Simulation setup

A CoFeB stripe with dimensions 20.48 $\mu$m x 320 nm x 20 nm was discretized in 5 nm x 5 nm x 20 nm cells, with periodic boundary conditions applied in the x and y axes to simulate an infinite film, see figure 4.10. The following properties were defined for $Co_{20}Fe_{60}B_{20}$ [106, 107]: saturation magnetization $1.2 \times 10^6$ A/m, exchange stiffness $18 \times 10^{-12}$ J/m, stiffness constants $C_{11} = 283 \times 10^9$ N/m$^2$, $C_{12} = 166 \times 10^9$ N/m$^2$ and $C_{44} = 58 \times 10^9$ N/m$^2$, mass density $\rho = 8 \times 10^3$ kg/m$^3$ and magnetoelastic constants $B_1 = B_2 = -8.8 \times 10^6$ J/m$^3$. The magnetic damping parameter is set to $\alpha = 10^{-3}$ and the elastic damping $\eta$ is set to zero.

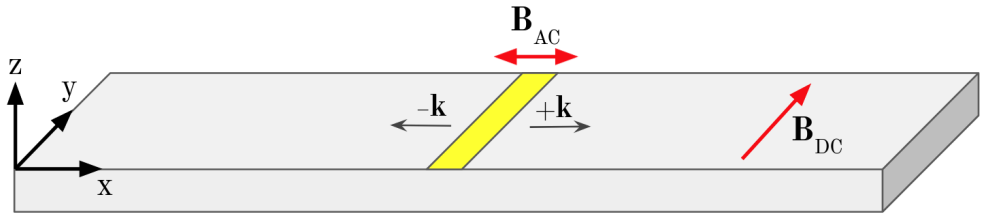


Figure 4.10: The simulation setup. A CoFeB stripe with periodic boundary conditions to simulate an infinite film with a static magnetic field ($\mathbf{B}_{DC}$) applied in the y-direction. An alternate magnetic field ($\mathbf{B}_{AC}$) is applied in the x-axis in yellow region in order to drive the spin dynamics. Plane spin waves are excited and propagate along the x-axis, perpendicular to the magnetization direction.

A static magnetic induction field is applied in the y-direction, $\vec{B}_{DC} = B_0\hat{y}$ and a 100 nm wide line, the yellow region in figure 4.10, is defined as an antenna in order to probe the spin dynamics. By applying either an alternate sinusoidal or a sinc-pulse external magnetic field perpendicular to the magnetization direction, $\vec{B}_{AC} = B_{AC}\hat{x}$ at the antenna, plane spin

waves are excited and propagate both in $+\hat{x}$ and $-\hat{x}$ directions. Absorbing boundaries were applied at the borders in order to avoid wave reflection. In these boundaries, in the last 5 $\mu$m of each side, the Gilbert damping ($\alpha$) is increased from $10^{-3}$ to 0.5 and the elastic damping ($\eta$) from zero to $5 \times 10^{13}$.

### 4.2.3 Results

In this section, we will begin by presenting the results of magnetoelastic waves under a constant magnetic field, in thin films with the wave vector geometry perpendicular to the static magnetization. We will examine how the elastic and magnetic eigenmodes, and the position of the anticrossing gap are modified by varying the external field intensity. Using this information, we will then determine the desired values for the spatially-varying field that would allow the excitation to start in a quasi-magnetic regime and end in a quasi-elastic one. Finally, we will present the results of pulse propagation using the spatially varying magnetic field.

#### Magnetoelastic waves under a uniform field

First, a uniform magnetization and zero displacement are set as initial conditions, and the system is allowed to relax to a minimium energy state under $\vec{B}_{DC} = 100$ mT $\hat{y}$. Then a sinc-pulse magnetic field, $\vec{B}_{AC} = [B_{AC}\ \sin(2\pi f_0 t)/(2\pi f_o t)]\hat{x}$, with $B_{AC} = 20$ mT and $f_0 = 50$ GHz was applied in the antenna region and both the magnetization $\vec{m}$ and the displacement $\vec{u}$ vector maps are saved as a function of time. These vector maps were fast-Fourier transformed in order to obtain the dispersion relation of the sample, see Figure 4.11.

Distinct behaviors can be observed in the FFT of different components of magnetization and elastic displacement. For example, the longitudinal displacement $u_x$ and out-of-plane transverse displacement $u_z$ (shown in Figures 4.11b and 4.11d) displayed only a single linear curve without any gap formed from magnetoelastic interaction. In this geometry, where the wave vector is perpendicular to the static magnetization ($\vec{k} \perp \vec{M}_0$), the theoretical prediction in Section 2.5.3 suggests that only the in-plane transverse component ($u_y$) of the elastic waves couples to the magnetization, which is in agreement with the simulation results.

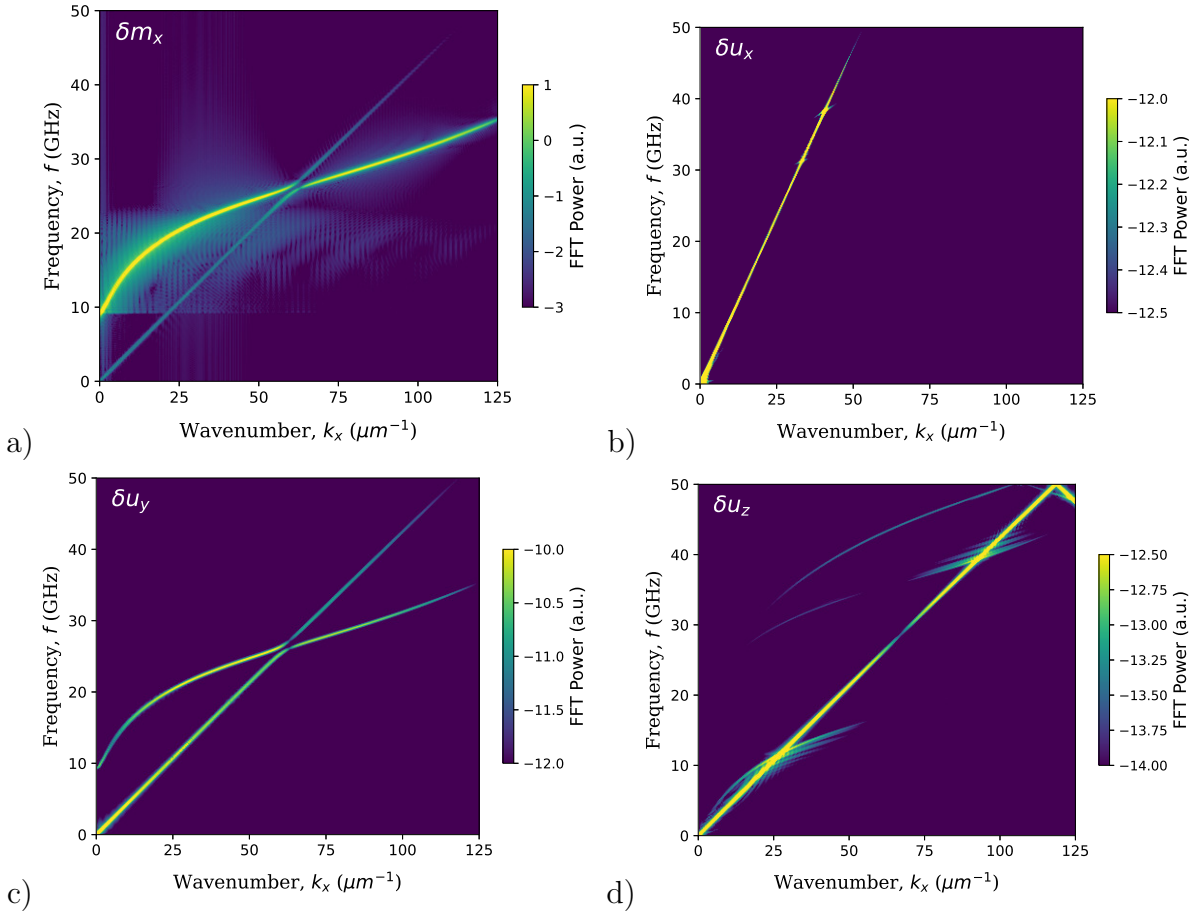


Figure 4.11: The dispersion relation for magnetoelastic waves propagating along the x-direction, $\vec{k} = k_x\hat{x}$, under a static field of $\vec{B}_{DC} = (100\text{ mT})\hat{y}$. This was obtained by applying a fast-Fourier transform (FFT) of (a) $m_x$, (b) $u_x$, (c) $u_y$ and (d) $u_z$ along the x-axis. Similar results are found for the FFT of $m_x$ and $m_z$. The magnetoelastic crossover is only present at $m_x$, $m_z$ and $u_y$. For the other displacement directions only the elastic component is present with a longitudinal velocity of 5938 m/s and a transverse velocity of 2683 m/s.

The two uncoupled curves exhibit a linear dispersion, and their group velocity is equal to the phase velocity. The expected velocities for transverse ($v_t = \sqrt{c44/\rho}$) and longitudinal ($v_l = \sqrt{c_{11}/\rho}$) elastic waves, using the material properties values employed in the simulations, are $v_t = 2693$ m/s and $v_l = 5948$ m/s, respectively. The calculated phase

velocities for $u_z$ and $u_x$ are 2682 m/s and 5938 m/s, respectively, in agreement with the theoretical values for uncoupled elastic wave components in thin films presented in Section 2.4.2.

On the other hand, the components $m_x$, $m_z$, and $u_y$ (as seen in Fig 4.11a and 4.11c) presented similar behaviours, where two hybrid curves are formed in the dispersion relation, and they displayed an anticrossing gap at $k = 64\mu m^{-1}$ and $f = 26GHz$ under a 100 mT DC magnetic field. This is a strong indication of magnetoelastic coupling. From the theoretical prediction these three components are coupled via Equation 2.161.

Away from the anticrossing gap, the dispersion relations for $m_x$, $m_z$, and $u_y$ are similar to the uncoupled case. However, near the gap, the velocity is significantly altered, resulting in each curve being divided into three domains: quasi-elastic, quasi-magnetic, and magnetoelastic. In the quasi-elastic and quasi-magnetic domains, the dispersion coincides with the uncoupled mode, while in the magnetoelastic domain, the dispersion is significantly altered. For the lower curve, the quasi-elastic regime occurs at low-k values, and the quasi-magnetic regime occurs at high-k values. The upper curve exhibits the opposite behavior.

The magnetic dispersion curve can be shifted towards higher frequencies by increasing the static magnetic field intensity, as seen in Figure 4.12 for $B_0 = 40$ mT and 200 mT. Although the external field does not affect the elastic dispersion curve, the position of the magnetoelastic crossover gap changes significantly. For example, at 40 mT, the gap is located at $k = 55\mu m^{-1}$ and $f = 23.5GHz$, while at 200 mT, it shifts to $k = 71\mu m^{-1}$ and $f = 30GHz$.

The dispersion curves can be analyzed at a fixed frequency, indicated by the horizontal dashed lines in figure 4.12. For instance, at $f = 25$ GHz, two peaks are observed along the wavenumber for different magnetic field intensities. At 40 mT, the low-k peak corresponds to the elastic eigenmode at 58 $\mu m^{-1}$, followed by the magnetic mode at 67 $\mu m^{-1}$. In contrast, at 200 mT, the lower peak corresponds to the magnetic mode at 34 $\mu m^{-1}$, and the higher peak corresponds to the elastic mode at 59 $\mu m^{-1}$.

At a fixed frequency, the selection of appropriate external magnetic field values can excite a wave in the quasi-elastic, quasi-magnetic or magnetoelastic regimes. Our aim is to create a magnetic field with a continuously spatially-varying profile, such that the excitation is initially in the quasi-magnetic regime, but eventually transits through the magnetoelastic regime, ending in the quasi-elastic regime.

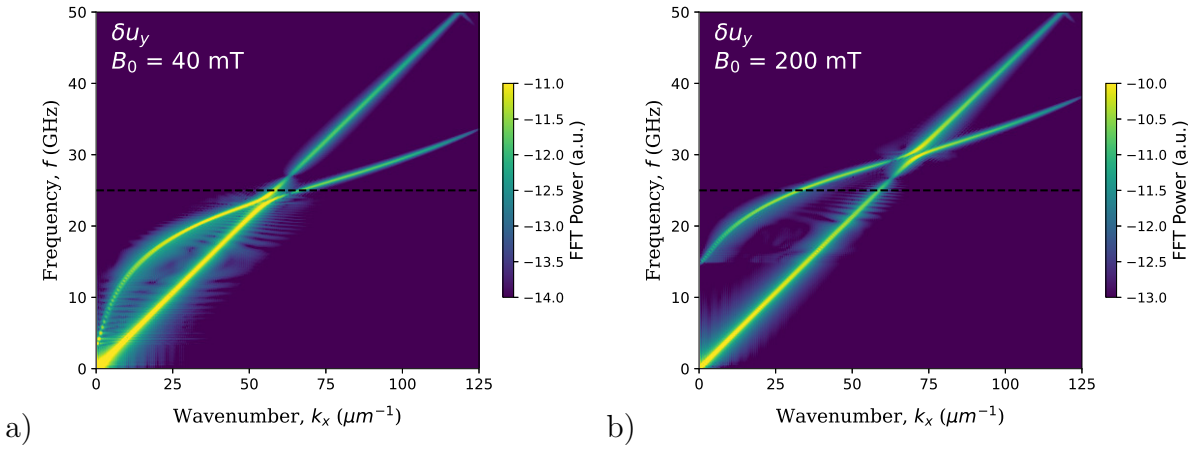


Figure 4.12: The magnetoelastic dispersion relation obtained from the FFT of $u_y$ at an external magnetic field of (a) 40 mT and (b) 200 mT, perpendicular to the static magnetization direction. The horizontal dashed line corresponds to the frequency $f = 25$ GHz.

To obtain the desired spatially varying field, we begin by performing a simulation where a constant frequency excitation at 25 GHz is introduced and allowed to propagate under a constant magnetic field. We then use a spatial FFT to measure the wave number of the components $m_x$ and $u_y$ as a function of the external field. This measurement is carried out for two situations: (a) when the magnetic and elastic modes are uncoupled, i.e. when the magnetoelastic constants are set to zero ($B_1 = B_2 = 0$) and (b) when they are coupled ($B_1 = B_2 \neq 0$), the results are shown in figure 4.13.

In the uncoupled system, figure 4.13a, the magnetic curve is obtained by the AC magnetic field excitation followed by the FFT of $m_x$, and the elastic one by the AC excitation of the force density, with the FFT of $u_y$. In the magnetic curve, the wavenumber (k) of the spin wave is smaller, that is a larger wavelength ($\lambda$), the higher is the magnetic field for a fixed frequency. This is in agreement with the theoretically evaluated dispersion relation for a thin film, equation 2.80. Also, as expected, the purely elastic wave is not affected by the external magnetic field.

On the other hand, in the coupled system, figure 4.13b, two branches are visible, a lower and an upper one. Both branches present magnetic and elastic proprieties. The lower branch has a dominant elastic behaviour for $B_{DC} < 60mT$ and a dominant magnetic behaviour for $B_{DC} > 100mT$. The opposite happens in the upper branch, quasi-magnetic

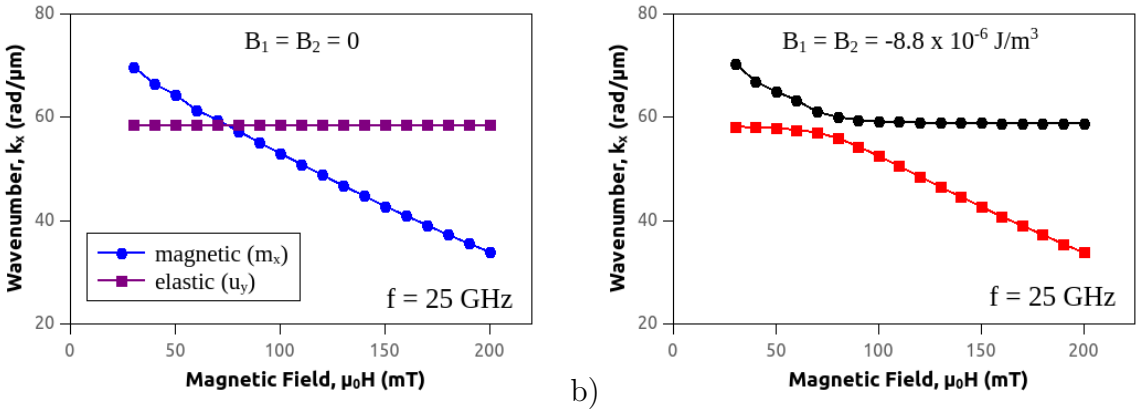


Figure 4.13: The resulting wavenumber ($k_x$) for a 25 GHz excitation for (a) the uncoupled system, with magnetoelastic constants ($B_1$ and $B_2$) set to zero, and for (b) the magnetoelastic coupled system.

for low $B_{DC}$, and quasi-elastic for high $B_{DC}$ values. In the 60 mT $< B_{DC} <$ 100 mT range, both branches transit from one propriety to the other, and therefore both elastic and magnetic proprieties are present simultaneously, and thus those are magnetoelastic waves.

### Magnetoelastic waves under a spatially-varying field

When a spin wavepacket propagates through a non-uniform spatial field, its frequency remains constant while the wavenumber changes according to the local value of the field intensity. On the other hand, if the propagation occurs in a uniform field that varies in time, the wavenumber remains constant while the frequency varies according to the field [59, 108].

This way, we aimed to probe the interconversion of magnetic to an elastic excitation, a magnon-phonon conversion, by means of micromagnetic simulations using the momentum conservation. The idea here is to excite a magnetic wavepacket that propagates through a spatially non-uniform external magnetic field, which starts in the quasi-magnetic region of the dispersion and arrives in the quasi-elastic region.

The simulations is set as Figure 4.14, a quadratically-varying magnetic field from a 300 mT intensity until the excitation region (x = -5 $\mu m$), to 30 mT for x $\geq$ 5 $\mu m$. For 25 GHz,

these values correspond to wave numbers, respectively, in the quasi-magnetic and in the quasi-elastic regions, as shown in the upper branch of figure 4.13.

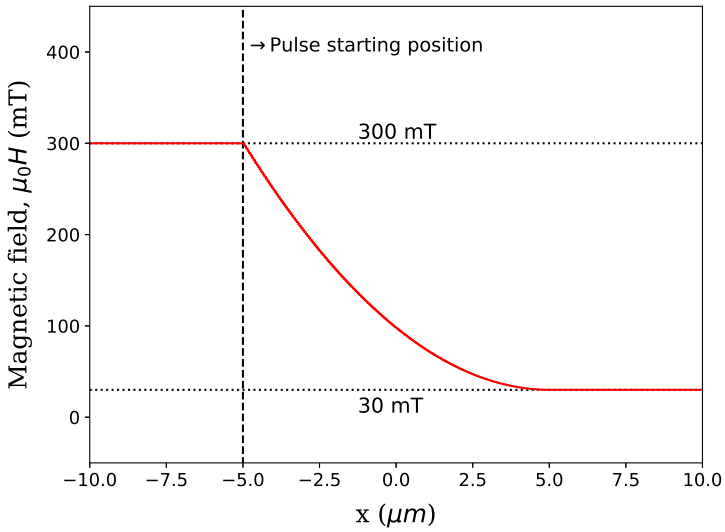


Figure 4.14: The spatially-varying external magnetic field, $H(x)$. It decreases quadratically from a 300 mT to a 30 mT intensity. A magnetic pulse is excited at the x = 5 $\mu m$ position and propagates in the $+x$ direction.

For a non-uniform field, if the spatial field gradient is smaller than a critical value, the excitation does not change branch in the dispersion relation, as shown in Figure 4.13. In this scenario, the pulse can be converted from a quasi-magnetic nature to a quasi-elastic one, without branch hopping. The critical value can be evaluated as [109]

$$\frac{dH_{crit}}{dx} = \frac{\pi B_2 \omega}{M_s \rho v_t^3}. \tag{4.2}$$

For our setup, this value corresponds to 153 mT/$\mu$m, which is much larger than the value used in this simulation (in the order of 40 mT/$\mu$m).

The pulse is generated by applying a sinusoidal external magnetic field, $\vec{H}_{ac}$ = (10 mT) $\sin[2\pi(25GHz)t]\hat{x}$, at a 100 nm wide region centered in x = -5 $\mu m$ for 0.5 ns and then changing it to zero until the end of the simulation at time t = 10 ns. The pulse propagation is shown in figure 4.15. Two wavefronts are formed, one going in the $+x$ and the other in the $-x$ directions. The $-x$ one is rapidly attenuated by the absorbing

boundaries, whereas the $+x$ one propagates along the stripe, under the varying external field, until being absorbed at the right edge of the slab.

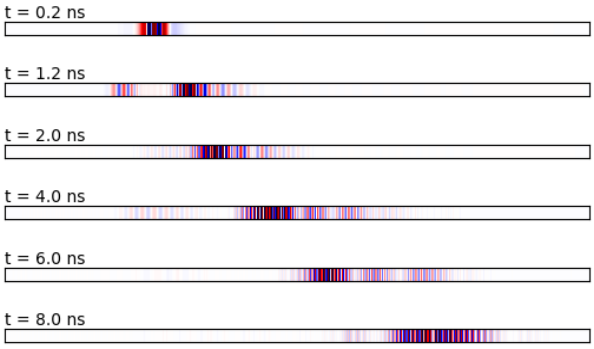


Figure 4.15: Pulse propagation under a spatially-varying magnetic field. The images show $m_x$ as a function of the time. The pulse is excited at the x = -5 $\mu m$ position. The red and blue colors correspond to, respectively, positive and negative variations of the magnetization x-component.

Along the pulse propagation its frequency remains constant at 25 GHz whereas its wavenumber is continuously changed due to the external magnetic field gradient. Figure 4.16a shows the wavenumber $k_x$ measured as a function of time and the corresponding spatial FFT amplitude at that wave number in Figure 4.16b.

The wave number during the excitation period starts at 18 $\mu m^{-1}$ under the initial 300 mT external field where the amplitude of $m_x$ linearly grows until reaching a maximum. Then, along the propagation the wave number varies up to 57 $\mu m^{-1}$, with its amplitude decaying exponentially due to the intrinsic magnetic damping ($\alpha$) until reaching the absorbing boundary at the right edge of the slab at 8 ns.

The $u_y$ absolute amplitude is much smaller than the $m_x$ one at all times of the simulation, however at the instant t = 5 ns, along with the wave number sudden change to 60 $\mu m^{-1}$, its amplitude is strongly enhanced, see the peak at Figure 4.16b. This enhancement of the elastic $u_y$ component is attributed to the magnetoelastic interconversion.

Finally, to highlight the transition from magnetic oscillations to lattice vibrations we have run the simulation again, changing the Gilbert damping $\alpha$ to zero in the middle of the stripe, so both elastic and magnetic components do not suffer any losses until reaching

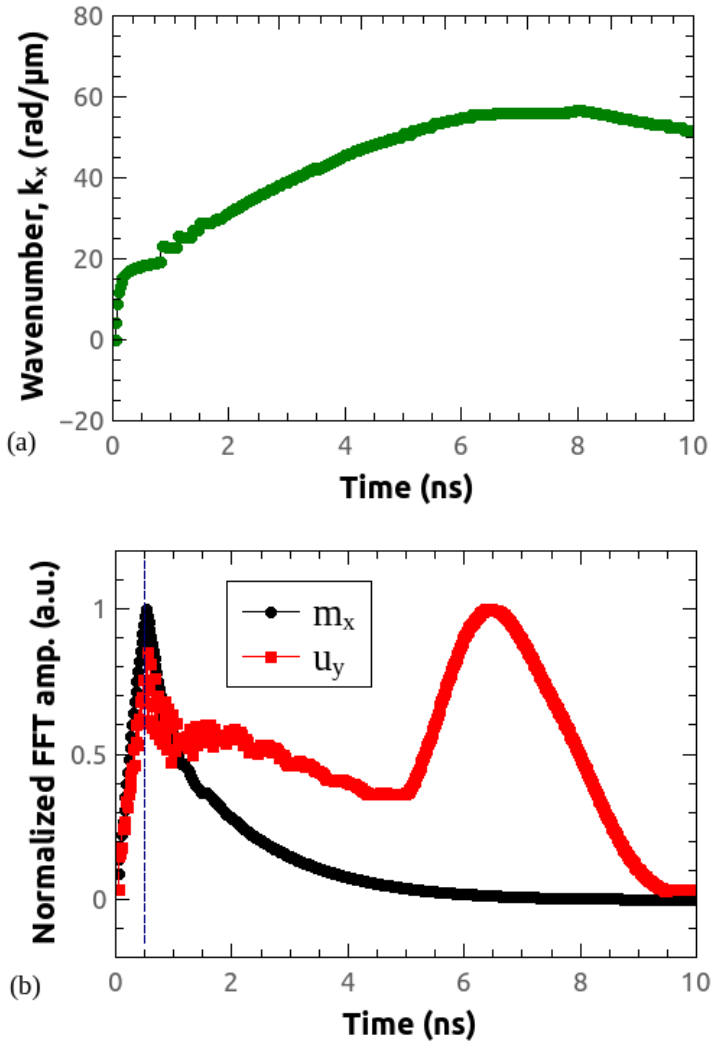


Figure 4.16: (a) The wavenumber $k_x$ of the pulse measured from the spatial FFT as a function of the time as the pulse propagates in the +x direction. (b) The FFT amplitude for the corresponding wavenumber along the pulse propagation. The vertical dashed line shows the instant in which the excitation field is turned off.

the absorbing edges. We evaluated the magnetic energy as the sum of the exchange, magnetostatic and Zeeman components, subtracted from their values at equilibrium (t = 0), and the elastic component as the sum of the Hooke's component, $\int \frac{1}{2}\hat{\sigma}dV$, where $\hat{\sigma}$ is

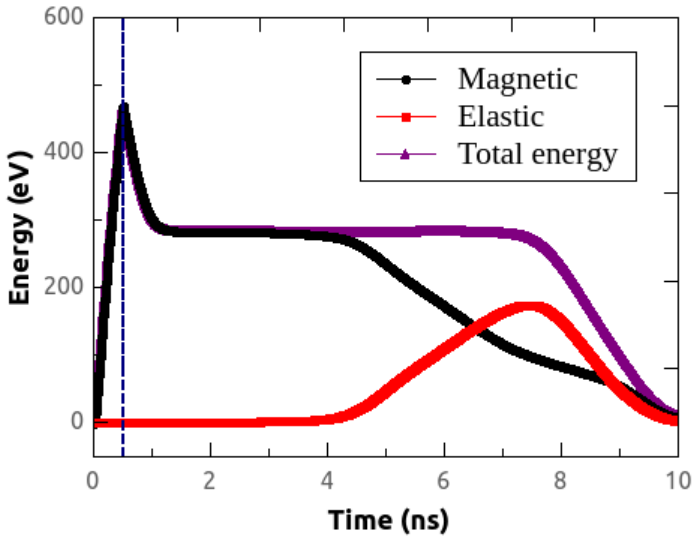


Figure 4.17: The energy components of the system as a function of time. The magnetic energy is evaluated as the sum of the magnetostatic, exchange and Zeeman energies, and the elastic one as the sum of the Hooke's with the kinetic components. The vertical dashed line shows the instant in which the excitation field is turned off.

the stress tensor calculated from Hooke's law, and the kinetic component, $\int \frac{1}{2}\ \rho\dot{\vec{u}}dV$.

Figure 4.17 shows the energy components of the system as a function of the time in that setup. The magnetic energy is linearly increased during the AC excitation (until t = 0.5 ns), when it presents a loss due to the readily $-x$ wave front absorption. The remaining $+x$ wave front stays with a constant energy, due to the absence of intrinsic magnetic damping until 4 ns where its energy is gradually transferred to the elastic system, which continuously grow until reaching a maximum at 8 ns and after that the pulse is absorbed at the boundary.

Therefore, the pulse is excited in the quasi-magnetic region of the dispersion and is gradually converted to the quasi-elastic region, by varying the wavenumber and keeping the frequency constant. This way, the spatially inhomogeneous magnetic field was employed to probe the interconversion between magnetic and elastic excitations due to the magnetoelastic interaction.

### 4.2.4 Conclusions

In this section, we presented a simulation of spin wave conversion to an elastic wave in a thin film using the magnetoelastic extension of MuMax3 [96]. Our simulation involved the study of magnetoelastic wave dispersion in thin films. As expected for this geometry, only the in-plane transverse elastic component ($u_y$) is coupled to the magnetization dynamics, and the anticrossing gap is formed in $u_y$, $m_x$, and $m_z$. We observed that by changing the external magnetic field, the position of the magnetic curves and the anticrossing gap also changed. By fixing the frequency of the excitation, we could obtain quasi-elastic, quasi-magnetic, and magnetoelastic behaviors for certain magnetic field intensities.

Furthermore, we designed a setup with a varying static magnetic field, with a gradient below the critical value for branch hopping. We excited a wavepacket in the quasi-magnetic region, and as it propagated, its frequency remained constant while its wavenumber gradually changed, eventually reaching the quasi-elastic region. We observed that the spin wave was converted to an elastic wave, which was evident from the amplitudes and energies of the system, consistent with theoretical predictions and experiments.

In conclusion, our simulation reveals how spin waves can be converted to elastic waves in thin films, highlighting the usefulness of magnetoelastic simulations for predicting the behaviour of magnetoelastic excitations. This insight may have implications for the development of new magnonic devices.

## 4.3 Magnetoelastic waves in Néel-type domain walls

In this section, we focused on using the magnetoelastic extension of MuMax3 [96] to study the magnetic and elastic eigenmodes of a magnetoelastic strip containing a Néel-type domain wall.

While analytical solutions for the wave equations in infinite films are available, these solutions become impractical when complex patterns of magnetization are present. Thus, we turned to simulations to obtain a better understanding of the system and to compare the results with theoretical predictions.

Interestingly, even with the presence of magnetoelastic interaction, some of the curves do not form anticrossing gaps. We will discuss this further and show that this can be explained based on the symmetry of the elastic and magnetic modes. The simulation results have been previously published and are available in [98].

### 4.3.1 Introduction

Transmitting and processing data with spin waves (SW) is a promising field known as magnonics, that has the potential to increase the energy efficiency and reduce the size of the current information technology [2, 11, 103]. However, the low efficiency in SW excitation and detection [51] and the small propagation length [53] remain drawbacks in the field. The coupling between SW and elastic waves, through the magnetoelastic interaction, has emerged as a promising strategy to overcome these challenges [54, 64].

Recently, magnetic domain walls have been proposed as propagation channels for spin waves [110, 111]. The domain walls can be found in closure-domain remanent states, which are stable even without an external magnetic field. Also, the domain walls are topologically protected regions that act as potential wells for propagating SW, creating laterally-confined magnetic modes with high group velocities [23, 112, 113]. This way, these propagating waves are promising candidates for data carriers in magnonic systems. However, a study of the effect of magnetoelastic interaction taking into account the domain wall-confined magnetic eigenmodes is still lacking.

In this work, we have calculated the dynamics of magnetoelastic waves in a thin CoFeB slab containing a Néel wall using coupled micromagnetic and elastodynamics simulations.

We have obtained the dispersion relation for the magnetic and elastic modes and compared them to the analytical equations for the uncoupled waves. Then we show three examples of crossing points between elastic and magnetic eigenmodes and discuss the formation of an anticrossing gap due to a strong coupling, or gapless crossing, for independent resonators.

### 4.3.2 Simulation setup

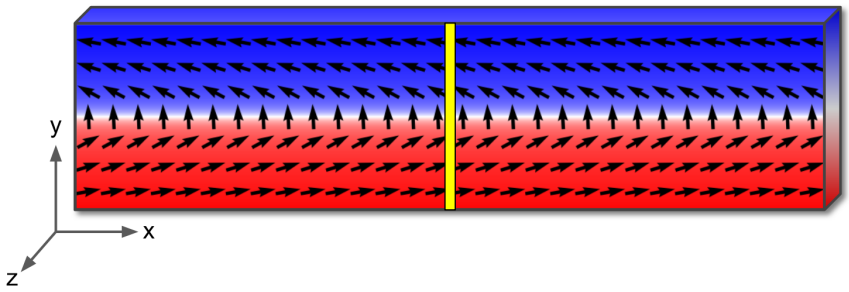


Figure 4.18: Sketch of the thin magnetic stripe of two oppositely magnetized domains with the Néel wall between them. The arrows show the direction of the magnetization at equilibrium, and the yellow stripe indicates the region where the external pulse is applied to generate spin and elastic waves.

We have numerically calculated the magnetic and elastic dynamics of thin magnetoelastic stripes with a high aspect ratio containing two oppositely magnetized domains, separated by a Néel-type domain wall, see Figure 4.18. The film is in the xy-plane, with the bottom and top magnetic domains oriented, respectively, in the $+\hat{x}$ and $-\hat{x}$ directions. The Néel domain wall is the transition between these two domains, in which the magnetization curls anticlockwise in-plane, being aligned in the $+\hat{y}$ direction precisely at its center.

The magnetic eigenmodes are excited by an external magnetic field pulse applied in the yellow stripe of Figure 4.18, generating plane waves that propagate in the x-direction. The elastic modes are also excited via the magnetoelastic interaction in this process. In the opposite sense, a lattice elastic perturbation applied at the yellow stripe position can generate magnetic modes.

We have numerically simulated the coupled magnetization and elastodynamic dynamics, using Mumax3 [78] software including the magnetoelastic module extension [114]. We

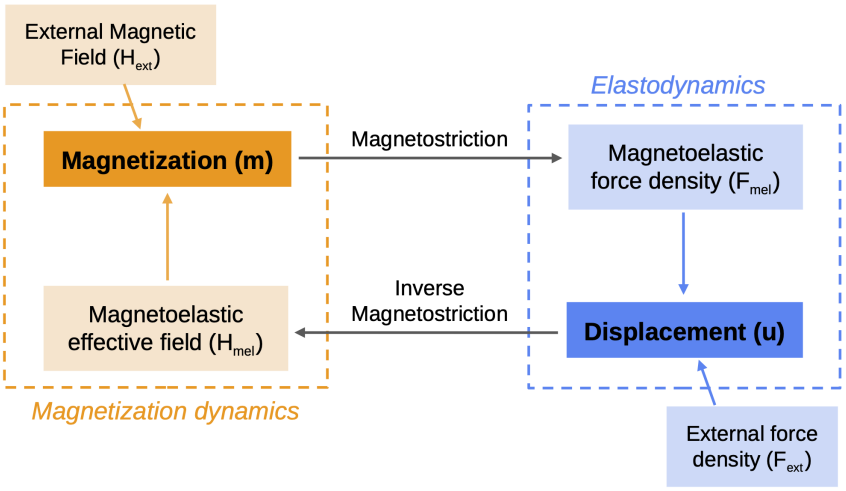


Figure 4.19: The magnetoelastic feedback. Scheme of the magnetoelastic interaction, the magnetization dynamics creates a force density, through the magnetostrictive effect, that drives the elastic displacement dynamics that, for instance, creates an effective magnetoelastic field from the inverse magnetostriction that drives the magnetization. This system can feedback itself generating two coupled oscillators.

have simulated magnetic materials with large magnetoelasticity constants like CoFeB, Ni, and Yttrium Iron Garnet (YIG) and qualitatively similar results were found. However, all the results presented here are for CoFeB [106, 107] due to the feasibility of experimentally obtaining Néel domain walls in a reproducible manner [115–119]. We consider the saturation magnetization ($M_S$) 1.6 MA/m, exchange stiffness ($A_{ex}$) 18 pJ/m, Gilbert damping ($\alpha$) 0.007, and elastic stiffness constants $C_{11} = 283$ GPa, $C_{12} = 166$ GPa and $C_{44} = 58$ GPa, mass density ($\rho$) 8000 km/m$^3$ and magnetoelastic coupling constants $B_1 = B_2 = -8.8$ MJ/m$^3$.

To generate a Néel wall, stripes with a large aspect ratio were used, 32 nm wide, 20 nm thick, and 20.48 $\mu m$ long. The cell size is given by $dx = dy = 5$ nm, and $dz = 20$ nm, and the number of cells are $N_x = 4096$, $N_y = 64$, and $N_z = 1$. The simulations start already with the Néel wall placed in the middle, crossing the stripe long direction (see Figure 4.18). The wall remains stable even when it exhibits stationary or propagating modes in $u$ and $m$. No external static magnetic field is applied.

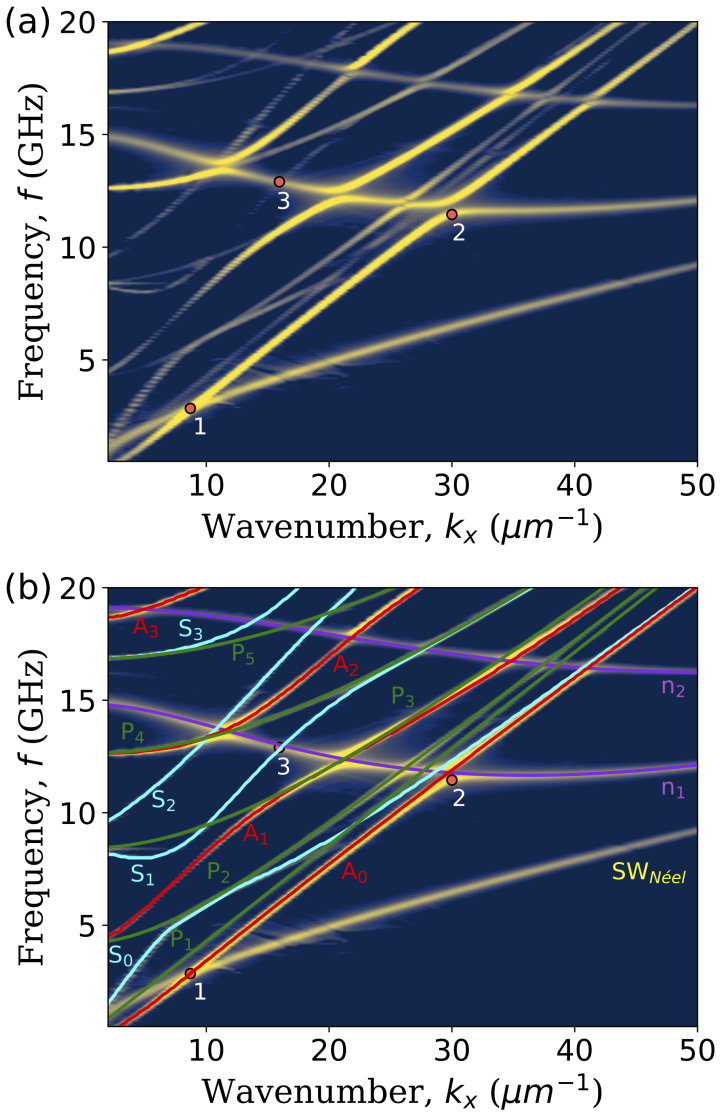


Figure 4.20: Dispersion relation of the coupled magnetoelastic system. (a) The curves were obtained from the magnetization and elastic displacement FFT in the numerical simulation. Due to the magnetoelastic interaction, several crossing points are separated by a gap into two branches, e.g., point "2", but also with several gapless crossing, as points "1" and "3". (b) Identification of the modes, obtained by calculation of analytical dispersion curves from theory.

In order to obtain the $u$ and $m$ modes, their dispersion relations, and the crossing of $u$ and $m$ branches, a small-amplitude sinc-shaped magnetic field applied on $\hat{z}$ direction with 50 GHz cut-off frequency applied in a 100 nm wide stripe placed at the middle of the stripe (see Figure 4.18). This produces $m$ waves and then $u$ waves due to the magnetoelastic coupling and run for a total of 20 ns allowing the excitation to extend over the whole sample.

Spatial-temporal Fast Fourier Transforms (FFT) are performed in the $u$ or $m$ components along the x-direction, allowing to build the entire dispersion relation of the coupled system, i.e., resonance frequency ($f_{res}$) as a function of the $k_x$ wave vector. To calculate the $u$ and $m$ modes the inverse Fast Fourier Transform (iFFT) is performed for the corresponding $f_{res}$ and $k_x$ point in the dispersion curve.

### 4.3.3 Results and discussion: Uncoupled elastic and magnetic modes

The magnetoelastic modes from the pulsed excitation in the micromagnetic simulations generate the dispersion relation, as shown in Figure 4.20a. It corresponds to a complex combination of coupled magnetic and elastic eigenmodes, some of which present an anti-crossing gap as point "2", and some with a gapless crossing like "1" and "3".

However, in order to identify the eigenmodes that correspond to each curve (elastic or magnetic), we have calculated the theoretical dispersion relation equations for the expected elastic and magnetic modes as if they were uncoupled from each other, that is, if the magnetoelastic constants were null, $B_1 = B_2 = 0$.

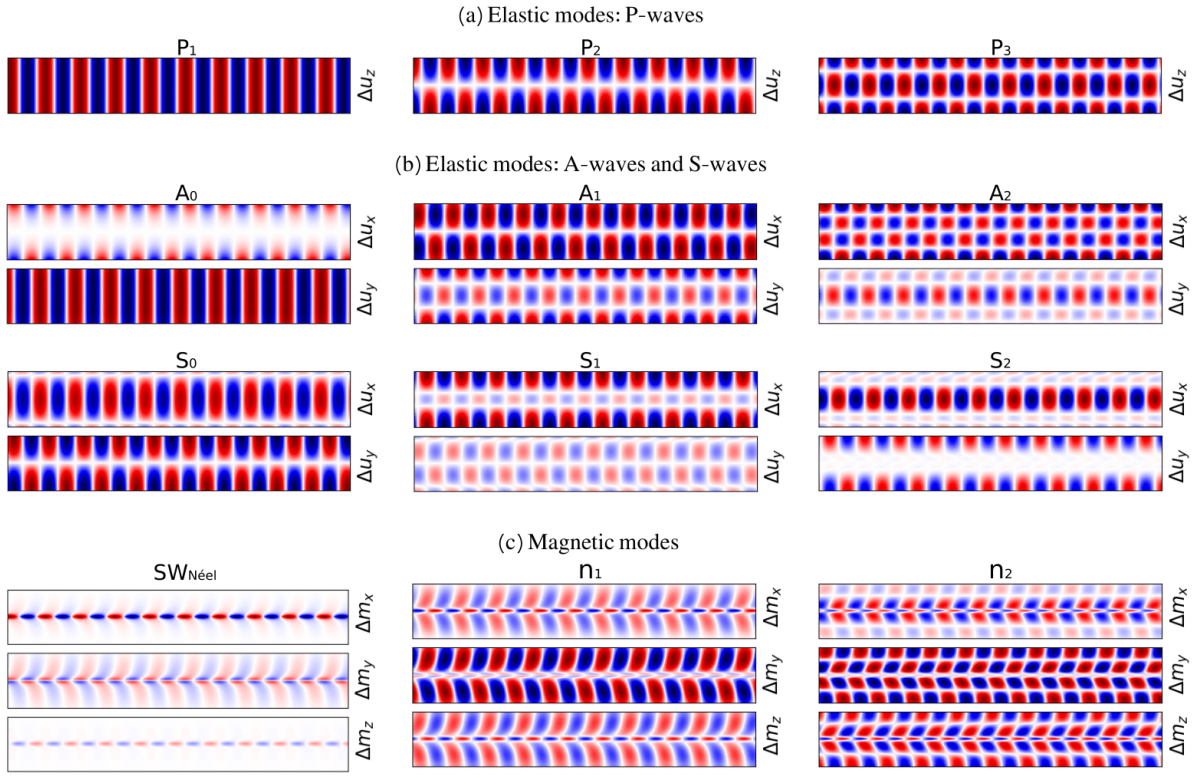


Figure 4.21: Uncoupled magnetic and elastic eigenmodes obtained from micromagnetic simulations with null coupling constants, $B_1 = B_2 = 0$. The finite width of the waveguide creates modes with quantized wave vector values in the y-direction. (a) The out-of-plane elastic waves, P-waves with null $\Delta u_x$ and $\Delta u_y$. (b) The two types of in-plane elastic waves, A-waves and S-waves, which have, respectively antisymmetric and symmetric $\Delta u_x$, the opposite for $\Delta u_y$, and null $\Delta u_z$ values. (c) The magnetic modes for the Néel wall, first the domain-wall confined mode, $\mathrm{SW}_{Neel}$, then the modes of the uniform domains, $\mathrm{n}_1$ and $\mathrm{n}_2$. The red and blue colors represent, respectively, positive and negative values.

### Elastic modes

Still considering uncoupled modes, consider a long waveguide, parallel to $\hat{x}$, with thickness $d$, where $kd \ll 1$, and width $w$. First, the out-of-plane modes, also known as P-waves,

follow the relation [93],

$$\omega_n = v_\perp \sqrt{k_x^2 + \frac{(n-1)\pi}{w}}, (n = 1, 2, 3, \cdots), \tag{4.3}$$

where $v_\perp = \sqrt{C_{44}/\rho}$ and $n$ is the mode order. The solutions for this equation are plotted as green lines in Figure 4.20b with the label $P_n$, with n ranging from 1 to 5. Snapshots of the out-of-plane displacement ($\Delta u_z$) of the P-wave modes are shown in Figure 4.21a. The first mode $P_1$ is uniform along the width, $k_y = 0$, and, as the finite width generate quantized wavelength values in that direction, in $P_2$ there is a node in the center, and $k_y = \pi/w$, in $P_3$, $k_y = 2\pi/w$, and so on. Finally, we highlight that, in relation to the wave propagation axis $\hat{x}$, the P-waves alternate between symmetric ($P_1$ and $P_3$) and antisymmetric modes ($P_2$). For the P-waves, the $\Delta u_x$ and $\Delta u_y$ components are negligible.

Differently from what we would get in an infinite film, in a waveguide with finite width, the in-plane elastic waves, the longitudinal ($\Delta u_x$) and transverse ($\Delta u_y$) components are coupled to each other [93]. For the displacement along $\hat{x}$, the elastic modes can be split into two systems, the S-waves and A-waves, where, in a waveguide with width $w$, their eigenfrequencies can be described by the solutions for the Rayleigh-Lamb equations [93],

$$\frac{\tan(qw/2)}{\tan(pw/2)} = -\left[\frac{4k_x^2 pq}{(q^2 - k_x^2)^2}\right]^{\pm 1}, \tag{4.4}$$

with $p^2 = (\omega/v_\parallel)^2 - k_x^2$, $q^2 = (\omega/v_\perp)^2 - k_x^2$ and the exponent $+1$ referring to S-waves and $-1$ to A-waves. The solutions for this transcendental equation were obtained numerically, and the results are plotted in Figure 4.20b as the cyan (S-waves) and red (A-waves) curves.

The corresponding elastic eigenmodes are shown in figure 4.21b for the A- and S-waves, respectively. It can be seen that, in the A-waves, $\Delta u_x$ is antisymmetric with regard to y=0 and $\Delta u_y$ is symmetric. The exact opposite happens for the S-waves, that is, the longitudinal displacement $\Delta u_x$ is symmetric and the transverse $\Delta u_y$, antisymmetric. The out-of-plane displacement $\Delta u_z$ is null in both wave types.

### Magnetic modes

Now, the magnetic modes propagating in the waveguide are not easily described by an analytical solution due to the complex shape of the magnetization of the two domains

separated by the Néel wall, see Figure 4.18. Disregarding the effects of the curling of the magnetization, we roughly describe the two uniform domains as waveguides with the magnetization parallel or antiparallel to the wave vector, with half of the total width of the stripe.

For a waveguide uniformly magnetized in $\hat{x}$, with $\mathbf{M} \parallel \mathbf{k}$ we obtain Backward-volume spin wave eigenmodes, that can be described by the relation [120, 121],

$$\omega_n = \sqrt{\omega_a \omega_b}, \tag{4.5}$$

where

$$\omega_a = \omega_H + \omega_M \left( D k_{tot}^2 + P \frac{k_y^2}{k_{tot}^2} \right), \tag{4.6}$$

$$\omega_b = \omega_H + \omega_M (D k_{tot}^2 + 1 - P), \tag{4.7}$$

$$P = 1 - \frac{1 - e^{k_{tot} d}}{kd}, \tag{4.8}$$

where $\omega_M = \mu_0 \gamma M_S$, $\omega_H = \mu_0 \gamma H_{ext}$, $k_{tot}^2 = k_x^2 + k_y^2$, and, due to the finite width of the waveguide, $k_y = n\pi / w_{eff}$, where $w_{eff}$ is the effective width [102, 122, 123] and n = 1, 2, 3, $\cdots$. In Figure 4.20b, we plot the first two magnetic modes of this equation in purple, $n_1$ and $n_2$, using $w_{eff} = 178$ nm and $\mu_0 H_{ext} = 22$ mT. The theoretical values present a good fit with the curves from the simulation, which shows that the approximation of the spin waves propagating along the uniform domains are reasonable for this range of f and k.

Besides those, an extra magnetic mode is found below $n_1$ and $n_2$ spin waves dispersion curves, which is linked to the Néel wall eigenmode, signed as $SW_{Neel}$ in Figure 4.20b. The curling of the magnetization due to the wall creates a strong demagnetizing field in the opposite direction of the magnetization in the center of the wall that decreases the total effective field in that region, generating a potential well [112]. This way, this potential creates a spin wave eigenmode that is laterally confined inside the domain-wall width, creating a channeling effect [110, 111]. We could not find an analytic equation to fit the curve of the Néel wall-confined mode.

The spatial distribution of the magnetization in the magnetic eigenmode is shown in Figure 4.21c. First, as expected for the confined mode, $SW_{Neel}$, the excitation is mainly concentrated within the Néel wall, and only a minor part reaches the domains. For the $n_1$ and $n_2$ modes, the excitation is mainly in the domains with curved wavefronts, and, for the latter, with one node in each domain center. In all magnetic modes, in relation to y=0, the $\Delta m_x$ and $\Delta m_z$ components are symmetric, while $\Delta m_y$ is antisymmetric.

### 4.3.4 Results and discussion: Coupled magnetoelastic modes

After showing the uncoupled elastic and magnetic modes, let us discuss the effect of the magnetoelastic coupling. The dispersion relation shown in Figure 4.20a was obtained by an excitation generated by an external magnetic field pulse, followed by FFT of the response from both magnetic and elastic components. Even though the excitation was purely magnetic, the elastic modes are also excited through the magnetoelastic interaction.

Away from the crossing points, in Figure 4.20b it can be seen that the uncoupled equations match the curves of the coupled system, which indicates that the eigenfrequencies are rather unperturbed by the interaction. The eigenmodes are mainly the same of the uncoupled system but with some minor changes in their spatial distribution such as a minor $\Delta u_z$ component in S- and A-waves, and small $\Delta u_x$ and $\Delta u_y$ in P-waves, as the magnetoelastic interaction couples all elastic components [121].

On the other hand, near the crossing points the curves can significantly differ from the uncoupled equations, some of those points present magnetoelastic anticrossing gaps, as the one pointed as "2" in Figure 4.20a. In these regions, the elastic and magnetic modes are strongly coupled to each other, we can say it is a magnetoelastic wave, and the curve is separated in two branches, one ranging from a pure-magnetic behavior towards a pure-elastic, and the vice-versa for the other branch [79, 94].

Nevertheless, some of the crossing points between curves do not present an anticrossing gap, and their curves are simply the sum of the elastic and the magnetic modes; see points "1" and "3" in Figure 4.20a. At these points, the magnetic and the elastic systems are both in resonance but independently. That happens when the magnetoelastic feedback does not fulfil their resonance, and the reasons for those will be discussed in this section. Next, we will show these three interaction points in the dispersion curve and discuss the presence or absence of the anticrossing gap in each of them.

#### Crossing of $\mathrm{SW}_{Neel}$ and $\mathrm{A}_0$ modes

First, let us discuss the gapless crossing between the Néel wall-confined magnetic eigenmode ($\mathrm{SW}_{Neel}$) and the elastic $\mathrm{A}_0$ mode at 2.9 GHz and 9 $\mu\mathrm{m}^{-1}$, pointed as "1" in Fig. 4.20a. The spatial distribution of the elastic displacement $\Delta u$ and magnetization $\Delta m$ amplitudes, together with the magnetoelastic body force $\mathrm{F}_{mel}$ and the magnetic field $\mathrm{H}_{mel}$ at that point

are shown in Figure 4.22. In this point, the $\Delta m$ and $\Delta u$ distributions are identical to the uncoupled modes, see Figure 4.21. The magnetic modes are mainly confined to the domain-wall width, while $\Delta u_x$ is restricted to the edges and $\Delta u_y$ is uniform along the $\hat{y}$ direction.

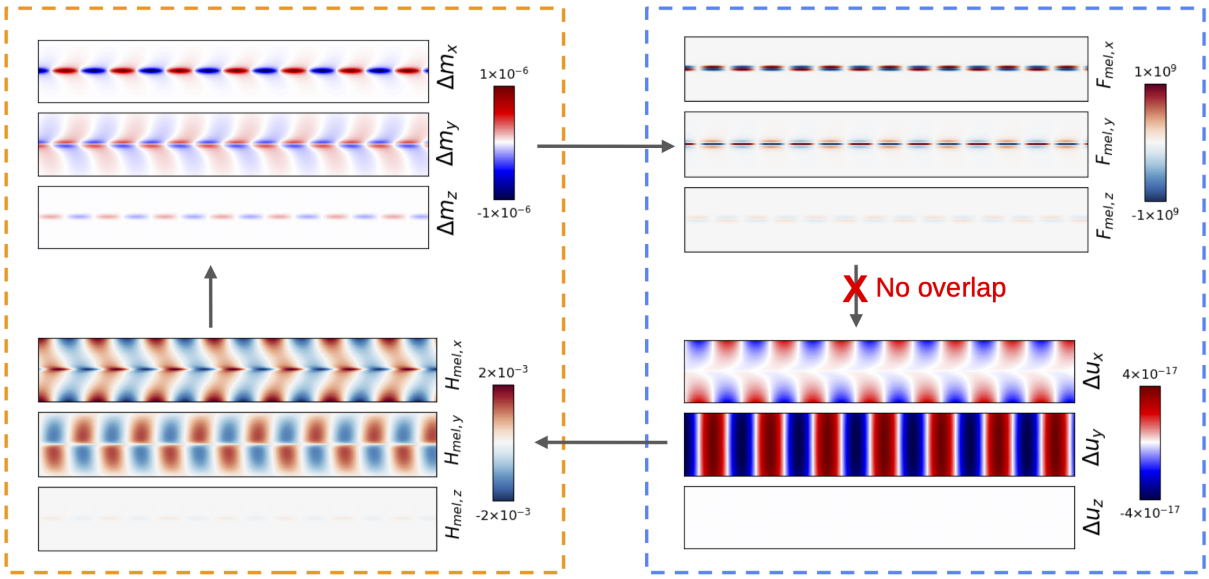


Figure 4.22: Point "1" in the dispersion relation: the gapless crossing between $\mathrm{SW}_{Neel}$ and $\mathrm{A}_0$. Starting from the top left image, we show for the results of the numerical simulation of the magnetoelastic coupled system, in clockwise direction, the magnetization $\Delta m$, the body force $F_{mel}$ [N/m$^3$], the elastic displacement $\Delta u$ [m], and the magnetoelastic magnetic field $H_{mel}$ [A/m]. This is a gapless crossing point in the dispersion relation as $\mathrm{F}_{mel}$ generated by $\Delta m$, confined to the wall-width, is not located in the same region as the displacement $\Delta u$ of elastic eigenmode, which is spread in the domains. Thus, the elastic and the magnetic systems are uncoupled at that point.

To understand why this is a gapless mode, we have to look again at the magnetoelastic feedback, summarized in Figure 4.19. The external magnetic field drives the magnetization resonance at that point, which is limited to the Néel wall width. The magnetization dynamics, for instance, due to the magnetostriction creates a magnetoelastic body force density $\mathrm{F}_{mel}$) which drives the elastic displacement resonance of the system. Finally, the displacement, through the inverse magnetostriction, generates an effective magnetoelastic field $\mathrm{H}_{mel}$ that drives the magnetization closing the feedback gap.

If now, let us check how the magnetoelastic feedback is working for this case. The external magnetic field drives the wall-confined magnetization dynamics shown in the top left of Figure 4.22, which, for instance, generates an effective body force, shown on the top right of the figure. If we look at the relation between $\mathrm{F}_{mel}$ and $\Delta u$ components, we can see that the overlap between them is minimal. In the x-direction $\mathrm{F}_{mel,x}$ is enclosed in the center, whereas $\Delta u_x$ is at the edges of the stripe. In y-direction $\mathrm{F}_{mel,y}$ is also confined to a narrow channel, and $\Delta u_y$ is spread all over the width. Therefore, it is not possible for this spatial distribution of $\mathrm{F}_{mel}$ to create a mode as the $\Delta u$ for $\mathrm{A}_0$.

In summary, the low overlap between the magnetoelastic body force $F_{mel}$ created by the magnetization dynamics, and the corresponding elastic displacement eigenmode do not allow the magnetoelastic feedback cycle to effectively close in that point. Consequently, the two modes oscillate as independent resonators, marking a gapless crossing point in the dispersion relation.

### Crossing of $\mathrm{n}_1$ and $\mathrm{A}_0$ modes

Let us check the anticrossing gap at 11.5 GHz and 30 $\mu\mathrm{m}^{-1}$ between the magnetic $\mathrm{n}_1$ and the elastic $\mathrm{A}_0$ modes, see point "2" in Figure 4.20a. Unlike the previous point "1", here we can see that interaction between the modes creates a gap, $\Delta f = 0.6$ GHz, separating them into two branches.

We show in Figure 4.23, in clockwise order, the magnetization $\Delta m$, the body force $F_{mel}$, the displacement $\Delta u$ and the effective magnetic field $H_{mel}$ for the point "2", Which is in the lower branch of the $\mathrm{n}_1$-$\mathrm{A}_0$ crossing. For the $\mathrm{n}_1$ magnetic mode $\Delta m$ is minimally affected by the magnetoelastic interaction, compared to the uncoupled $\mathrm{n}_1$ mode in Figure 4.21c, i.e., the coupled mode also has an excitation within the Néel wall along the plane waves in the uniform domains. They are symmetric in $\Delta m_x$ and $\Delta m_z$, and antisymmetric in $\Delta m_y$.

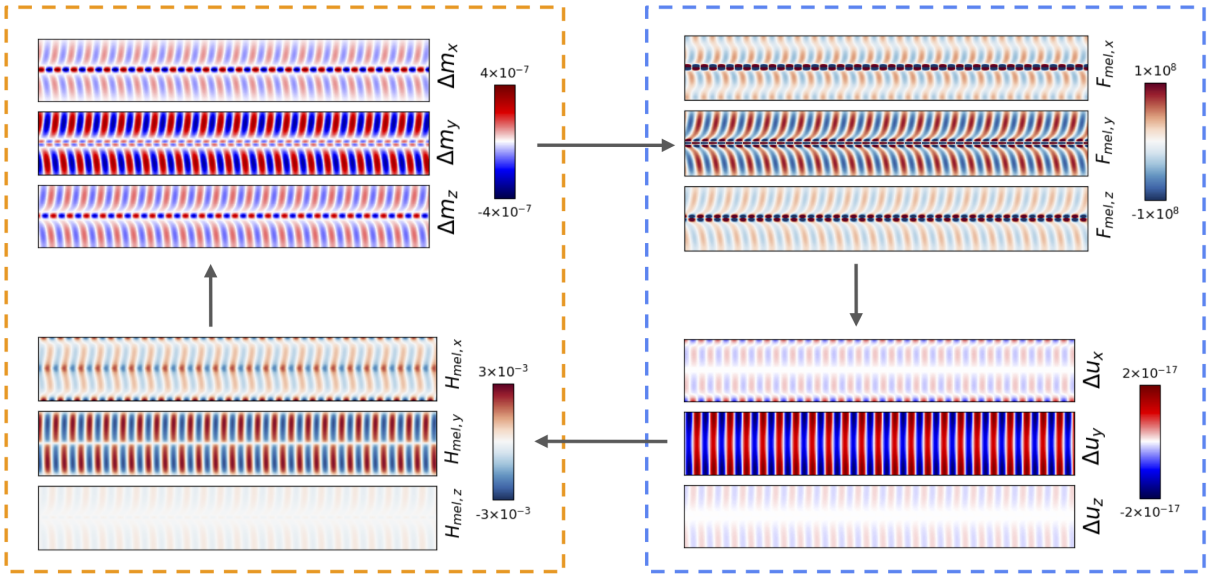


Figure 4.23: Point "2" in the dispersion relation: The coupled crossing of $n_1$ and $A_0$ modes. The numeric simulations at this point show a strong coupling between the magnetic and elastic systems as the $F_{mel}$ generated from the magnetization dynamics $\Delta m$ not only presents a high overlap to the displacement $\Delta u$ of the $A_0$ elastic mode, but also they both carry the same symmetry, antisymmetric for the $\hat{x}$ and $\hat{z}$ components, and symmetric in $\hat{y}$. The same happens between the effective magnetic field $H_{mel}$ and the magnetization $\Delta m$, effectively closing the magnetoelastic feedback cycle, creating an anticrossing gap in the dispersion curve.

On the other hand, the $\Delta u$ modes are affected by magnetoelastic interaction, compared to the $A_0$ mode in Figure 4.21b. One exception is $\Delta u_y$, which is composed of plane waves with constant amplitude along the width, just like in the uncoupled mode. In $\Delta u_x$, besides the edge excitation, an extra antisymmetric displacement occurs in the region of the domains and has a null $\Delta u_x$ displacement in the domain wall region. This extra antisymmetric excitation in the domains, null in the Néel wall, is also present in $\Delta u_z$, which is null in the uncoupled case.

These extra amplitudes in the elastic eigenmode and the anticrossing gap can be understood using the dynamics of the magnetoelastic body force $F_{mel}$ and the effective magnetic field $H_{mel}$. In Figure 4.23, the magnetic $\Delta m$ mode is excited by the external magnetic

field pulse, which for instance, generates the corresponding $F_{mel}$ shown in the top right corner. Comparing $F_{mel}$ to the displacement $\Delta u$ in this point, in $F_{mel,x}$ one sees that both the antisymmetric amplitudes at the edges and the extra amplitude inside the domains are similar to what we find in $\Delta u_x$. Also, besides the Néel wall region, $F_{mel,y}$ is symmetric and overlaps with $\Delta u_y$, so in this case, the body force can indeed be excite the elastic mode.

Also, the elastic displacement generates an effective magnetoelastic field $H_{mel}$, see Eq. 2.117, which is shown in the bottom left of Figure 4.23. Similarly, $H_{mel}$ overlaps to the $\Delta m$ modes, $H_{mel,x}$ and $H_{mel,z}$ are symmetric and $H_{mel,y}$ antisymmetric, just like the corresponding magnetic modes. This way, the magnetoelastic feedback cycle closes, and the magnetic dynamics drive the elastic resonance and vice-versa. Therefore, the two modes oscillate as coupled resonators, and a gap is formed in the crossing point of the dispersion relation.

### Crossing of $n_1$ and $S_1$ modes

Another interesting crossing in the relation dispersion occurs at point "3", which corresponds to the crossing of the magnetic $n_1$ and the elastic symmetric $S_1$ modes (12.8 GHz and 16 $\mu m^{-1}$). It is worth noting that here there is a net overlap of the body force and displacement and between the effective field and the magnetization, but it is still a gapless mode. Let us discuss why it happens by examining the spatial distribution of the coupled elastic and magnetic modes, as shown in Figure 4.24.

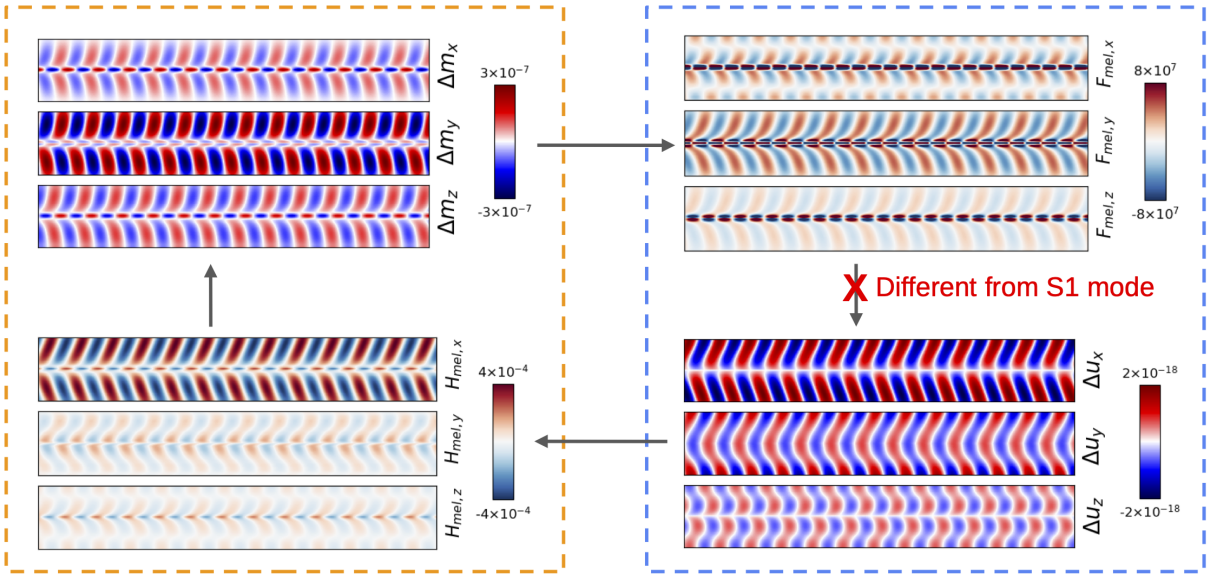


Figure 4.24: Point "3" in the dispersion relation: the gapless crossing of $n_1$ and $S_1$ modes. In this crossing point, the simulations show that $F_{mel}$ does overlap with $\Delta u$ and $H_{mel}$ overlaps $\Delta m$, but the elastic eigenmode generated by $F_{mel}$ is not equivalent to $S_1$, which the resonant elastic mode at that point. For instance, the $\Delta u$ mode has opposite symmetry from what we would expect for the $S_1$ eigenmode, which would be symmetric in $\Delta u_x$ and antisymmetric in $\Delta u_y$. This way, the elastic and the magnetic systems behave as independent oscillators, and no magnetoelastic gap is formed in the dispersion.

As in the previous cases, the $\Delta m$ mode does not change compared to the uncoupled case; compare the top left image in Figure 4.24 to the $n_1$ mode in Figure 4.21c. However, the picture is different in the elastic displacement; the $\Delta u$ mode obtained here is distinct from the uncoupled $S_1$ mode, see Figure 4.21b. The $\Delta u_x$ component of $S_1$ is symmetric while $\Delta u_y$ is antisymmetric, and the opposite is seen in the crossing point of the coupled system, $\Delta u_x$ is antisymmetric and $\Delta u_y$ is symmetric. Thus, the coupled elastic mode generated by the magnetoelastic interaction is not related to a pure elastic resonance at that point, which is the $S_1$ eigenmode.

The reason for such a different elastic mode arises from the shape of the magnetoelastic body force, as seen from the top right part of Figure 4.24. This body force is a consequence of the magnetization pattern, which has the Néel wall and generates a $F_{mel}$ that has an

antisymmetric pattern in $\hat{x}$ and $\hat{z}$, and symmetric in $\hat{y}$. This structure of the body force does not allow it to excite any mode that is symmetric in $\hat{x}$ direction. Therefore the S-waves cannot get coupled to this magnetic mode, and there is no gap as can be seen from the dispersion relation, see Figure 4.20.

Thus, the magnetoelastic feedback cycle cannot be closed here as the magnetoelastic body force, created by the magnetization pattern, has a different symmetry from the resonant elastic mode. This way, the body force excites an elastic mode that is not resonant, and the two systems cannot feedback themselves through the magnetoelastic interaction generating a gapless crossing.

Finally, the symmetry analysis can also be extended for the behaviour of the P-waves. The even-numbered P-modes ($P_2$ is shown in Figure 4.21a) present an antisymmetric $u_z$ pattern, which allows them to successfully interact with the magnetoelastic body force created by the magnetization dynamics, closing the feedback cycle, thus an anticrossing gap can be seen in Figure 4.20. On the other hand, the odd-numbered P-modes ($P_1$ and $P_3$ in Figure 4.21a) are symmetric in $u_z$, which would not allow an effective overlap with the antisymmetric body force, as can be seen in $P_1$ and $P_5$ modes, with gapless crossing points in Figure 4.20. The exception is the $P_3$ mode that presents an anticrossing gap in the dispersion curve, but at that point the $A_1$ curve is simultaneously crossing the magnetic one. So, even though the $P_3$ out-of-plane displacement is symmetric in $u_z$ and does not effectively overlap with the body force, the $A_1$ in-plane displacement is antisymmetric in $u_x$ and symmetric in $u_y$, just like the body force, and thus the magnetoelastic feedback cycle is effectively closed there.

### 4.3.5 Conclusions

In summary, we have simulated the magnetoelastic modes of a CoFeB waveguide containing a Néel wall. We have calculated the eigenfrequencies and mode profiles of the pure elastic modes, the out-of-plane P-waves, and the in-plane S- and A-waves. It was also done for the pure magnetic modes present in the Néel wall, that is one lower branch corresponding to the wall-confined mode with strictly-positive group velocity.

The dispersion relation for the coupled magnetoelastic showed a good agreement with the uncoupled analytical equations, showing that, far from the crossing points the eigen-modes only slightly affected by the magnetoelastic interaction. On the other hand, near

the crossing points, the magnetic and elastic modes can either generate coupled oscillators marked by a gap in the dispersion relation separating the curves into two branches or oscillate independently, forming a gapless crossing point.

We showed that the wall-confined spin wave could not be strongly coupled to the elastic modes, as the body force generated by the magnetization dynamics is also strongly confined to the domain wall width. Thus the overlap with the resonant elastic displacement is minimum, and the magnetoelastic feedback cycle cannot be effectively closed. Also, the other eigenmodes of the domain structure, due to its geometry, generate a body force that is antisymmetric in $\hat{x}$ and $\hat{z}$, and symmetric in $\hat{y}$, and it has the opposite symmetry of the S-waves displacement; thus they cannot effectively couple to each other, generating gapless crossing points.

Finally, concerning the possibility of employing elastic properties in developing novel spintronic devices, we have shown the conditions to obtain a strong magnetoelastic coupling. Not only the magnetoelastic body force and effective magnetic field should be nonzero for all components, but also a large overlap between $F_{mel}$ and $\Delta u$ and between $H_{mel}$ and $\Delta m$ should be present, with the same symmetry, to generate a strong magnetoelastic feedback cycle that can keep the two systems in a coupled oscillation.

# Chapter 5

# Summary and Perspectives

Throughout this thesis, we have explored the influence of the magnetoelastic interaction on the propagation of spin waves in thin films. Our investigations have included the effects of external strain on magnetization dynamics, the conversion of magnetic to elastic excitations and vice versa, and the hybrid modes formed by the coupling of elastic and magnetic waves.

By utilizing MuMax3 simulation software and its magnetoelastic extension, we have been able to gain valuable insights into the behavior of magnetoelastic excitations in thin films, with potential applications in the development of novel magnonic devices. In this final chapter, we will summarize the key findings of our research and discuss their implications for the field of magnonics.

## 5.1 Summary

The first simulation investigated the generation and propagation of spin waves in long Ni stripes in response to an external propagating strain wave. Through our simulations, we found that the most efficient excitation of spin waves occurs when the static magnetization is at 45 degrees in relation to the wave vector. We also observed that the propagation of the level of attenuation of the acoustic wave has a significant impact on the spin-wave propagation. When the acoustic wave rapidly decays, the spin wave is able to propagate freely but only over a short distance, whereas when the acoustic wave propagates over the

whole Ni stripe, the spin waves are carried by the acoustic waves and propagate over longer distances.

Our simulations also explored the potential use of voltage measurements, specifically through the ISHE voltage, to probe the spin-wave propagation. We determined the optimal placement of contact pads to measure both the AC and DC components in films, and obtained spin and charge current maps at the Ni/Pt interface and on the Pt line. These findings help to further understand the AC and DC acoustic-driven spin pumping effect.

The second simulation aimed to investigate the conversion of a spin wave to an elastic wave in an unbounded thin film using the magnetoelastic extension of MuMax3. The results obtained were in agreement with the theoretical predictions, demonstrating that only the in-plane transverse elastic component ($u_y$) is coupled to the magnetization dynamics, leading to the formation of an anticrossing gap in the dispersion relation. The intensity of the external magnetic field strongly affected the position of the gap, and by fixing the excitation frequency, quasi-elastic, quasi-magnetic, and magnetoelastic behaviors were observed for certain magnetic field intensities.

To obtain the conversion of a spin wave to an elastic wave, a setup with a spatially varying static magnetic field was designed. A wavepacket was excited in the quasi-magnetic region, and as it propagated, due to energy conservation, its frequency remained constant while its wavenumber gradually changed, eventually reaching the quasi-elastic region. The results showed that the spin wave is effectively converted to an elastic wave, as evidenced by the amplitudes and energies of the system. These findings have important implications for the development of novel magnonic devices, where the conversion of magnetic excitations to elastic waves can be utilized for signal processing and transmission.

In the third simulation, the focus was on the magnetoelastic modes of a CoFeB waveguide containing a Néel wall. The eigenfrequencies and mode profiles of the pure elastic modes, P-waves, S-waves, and A-waves, were calculated, as well as the pure magnetic modes, which include the Néel wall-confined mode and the backward volume modes in the uniform domains. Far from the crossing points, the dispersion relation for the coupled magnetoelastic modes showed good agreement with the uncoupled analytical equations. However, near the crossing points, the magnetic and elastic modes can either generate coupled oscillators marked by an anticrossing gap in the dispersion relation or oscillate independently, forming a gapless crossing point.

It was shown that the wall-confined spin wave could not be strongly coupled to the

elastic modes, as the body force generated by the magnetization is also strongly confined to the domain wall width. Thus the overlap to the elastic displacement is minimum, and the magnetoelastic feedback cycle cannot be effectively closed. Also, the magnetic eigenmodes that generate a body force that is antisymmetric in $\hat{x}$ and $\hat{z}$, and symmetric in $\hat{y}$, and thus have the opposite symmetry of the S-waves displacement; cannot effectively couple to each other, generating gapless crossing points.

Finally, it was shown that to obtain a strong magnetoelastic coupling and form an anticrossing gap, not only should the magnetoelastic body force and effective magnetic field be non-zero, but also a large overlap between $F_{mel}$ and $\Delta u$ and between $H_{mel}$ and $\Delta m$ should be present, with the same symmetry, to generate a strong magnetoelastic feedback cycle that can keep the two systems in a coupled oscillation. Overall, the simulation provided insights into the conditions required for a strong magnetoelastic coupling in a CoFeB waveguide containing a Néel wall.

In conclusion, the micromagnetic simulations presented in this section explored the effect of the magnetoelastic interaction in the propagation of spin waves, shedding light on the physics of hybrid interactions between magnons and phonons. These findings are important for the development of novel magnonic devices that rely on the magnetoelastic coupling, which can provide new functionalities and improved performance.

## 5.2 Perspectives

The simulations presented in this chapter have provided valuable insights into the magnetoelastic interaction and its effect on the propagation of spin waves. These findings open up exciting possibilities for future work, including experimental studies of the excitation of spin waves with interdigital transducers on piezoelectric substrates under constant or spatially varying magnetic fields. Such experiments would enable the exploration of the magnetoelastic coupling in more complex geometries and magnetic structures, and help to further refine our understanding of the underlying physics.

In addition to the experimental possibilities mentioned earlier, the results of this thesis also open up new avenues for micromagnetic simulations. One of these is the study of non-reciprocity in magnetoelastic waves, which can be achieved through the Dzyaloshinskii-Moriya interaction (DMI), among other mechanisms. This can be useful for the develop-

ment of spin wave circulators and couplers, which are essential components in magnonic devices for information processing and storage.

Another promising area of research is the interaction between magnetoelastic waves and magnetic textures, such as magnetic vortices or skyrmions. These structures have received significant attention due to their potential for application in race-track memories. The interaction between magnetoelastic waves and these magnetic textures can potentially lead to novel device concepts and improved performance.

These ideas for future work are summarized below:

- Interdigital transducers for efficient excitation and detection of magnonic signals: Interdigital transducers can provide an efficient means of exciting and detecting magnonic signals. This can involve exploring the design and optimization of interdigital transducers for different materials and structures, and studying the effects of various parameters such as transducer spacing, electrode width, and material properties.

- Magnetoelastic interaction to add non-reciprocity: The magnetoelastic interaction can be used to add non-reciprocity to create magnonic circulators or couplers, which are essential components in magnonic devices for information processing and storage. This can involve studying the design and optimization of magnonic circulators or couplers for different materials and structures, and exploring potential applications.

- Magnetoelastic waves and domain walls for race-track memory devices: The use of magnetoelastic waves and domain walls for creating race-track memory devices can provide a promising avenue for the development of next-generation data storage technologies. This can involve studying the interaction between magnetoelastic waves and domain walls, and exploring potential applications of this interaction in areas such as spintronic memory devices.

- Magnon-phonon interaction in quasi-particle quantum mechanics: Investigating the magnon-phonon interaction from the perspective of quasi-particle quantum mechanics can reveal deeper insights into the underlying physics. This can involve exploring the interaction between magnons and phonons in different materials and structures and studying the effects of various parameters such as temperature, magnetic field, and pressure.

- Chirality of phonons generated from magnons in spatially-varying magnetic fields: Studying the chirality of phonons generated from magnons in spatially-varying magnetic fields can lead to a better understanding of the magnetoelastic interaction. This can involve investigating the relationship between the chirality of phonons and the magnetic structure and properties of the material, and exploring potential applications.

- Effect of magnetoelastic wave propagation in complex magnetic structures: The effect of magnetoelastic wave propagation in complex magnetic structures, such as domain walls or films coupled by exchange bias, can have important implications for the development of novel devices. This can involve studying the interaction between magnetoelastic waves and magnetic textures, and exploring potential applications of this interaction.

Overall, the simulations presented in this thesis demonstrate the potential of magnetoelastic waves for a wide range of applications in information technology. The coupling between magnetic and elastic degrees of freedom provides a rich physics that can be exploited for the design of new devices and the exploration of fundamental physical phenomena. As such, future work in this area has the potential to significantly impact the field of magnonics and spintronics.

# References


[1] Felix Bloch. Zur theorie des austauschproblems und der remanenzerscheinung der ferromagnetika. In *Zur Theorie des Austauschproblems und der Remanenzerscheinung der Ferromagnetika*, pages 295–335. Springer Berlin Heidelberg, 1932. doi:10.1007/978-3-662-41138-4_1.

[2] A A Serga, A V Chumak, and B Hillebrands. YIG magnonics. *Journal of Physics D: Applied Physics*, 43(26):264002, June 2010. doi:10.1088/0022-3727/43/26/264002.

[3] Ivan Lisenkov, Albrecht Jander, and Pallavi Dhagat. Magnetoelastic parametric instabilities of localized spin waves induced by traveling elastic waves. *Physical Review B*, 99(18), May 2019. doi:10.1103/physrevb.99.184433.

[4] A. A. Serga, B. Hillebrands, S. O. Demokritov, A. N. Slavin, P. Wierzbicki, V. Vasyuchka, O. Dzyapko, and A. Chumak. Parametric generation of forward and phase-conjugated spin-wave bullets in magnetic films. *Physical Review Letters*, 94(16), April 2005. doi:10.1103/physrevlett.94.167202.

[5] T. Sebastian, T. Brächer, P. Pirro, A. A. Serga, B. Hillebrands, T. Kubota, H. Naganuma, M. Oogane, and Y. Ando. Nonlinear emission of spin-wave caustics from an edge mode of a MicrostructuredCo2mn0.6fe0.4siwaveguide. *Physical Review Letters*, 110(6), February 2013. doi:10.1103/physrevlett.110.067201.

[6] A. A. Serga, S. O. Demokritov, B. Hillebrands, and A. N. Slavin. Self-generation of two-dimensional spin-wave bullets. *Physical Review Letters*, 92(11), March 2004. doi:10.1103/physrevlett.92.117203.

[7] O. R. Sulymenko, O. V. Prokopenko, V. S. Tyberkevych, A. N. Slavin, and A. A. Serga. Bullets and droplets: Two-dimensional spin-wave solitons in modern magnonics (review article). *Low Temperature Physics*, 44(7):602–617, July 2018. doi:10.1063/1.5041426.

[8] S. O. Demokritov, V. E. Demidov, O. Dzyapko, G. A. Melkov, A. A. Serga, B. Hillebrands, and A. N. Slavin. Bose–einstein condensation of quasi-equilibrium magnons at room temperature under pumping. *Nature*, 443(7110):430–433, September 2006. doi:10.1038/nature05117.

[9] A. V. Chumak, G. A. Melkov, V. E. Demidov, O. Dzyapko, V. L. Safonov, and S. O. Demokritov. Bose-einstein condensation of magnons under incoherent pumping. *Physical Review Letters*, 102(18), May 2009. doi:10.1103/physrevlett.102.187205.

[10] Dmytro A. Bozhko, Alexander A. Serga, Peter Clausen, Vitaliy I. Vasyuchka, Frank Heussner, Gennadii A. Melkov, Anna Pomyalov, Victor S. L'vov, and Burkard Hillebrands. Supercurrent in a room-temperature bose–einstein magnon condensate. *Nature Physics*, 12(11):1057–1062, August 2016. doi:10.1038/nphys3838.

[11] A. V. Chumak, V. I. Vasyuchka, A. A. Serga, and B. Hillebrands. Magnon spintronics. *Nature Physics*, 11(6):453–461, June 2015. doi:10.1038/nphys3347.

[12] Anjan Barman, Gianluca Gubbiotti, S Ladak, A O Adeyeye, M Krawczyk, J Gräfe, C Adelmann, S Cotofana, A Naeemi, V I Vasyuchka, B Hillebrands, S A Nikitov, H Yu, D Grundler, A V Sadovnikov, A A Grachev, S E Sheshukova, J-Y Duquesne, M Marangolo, G Csaba, W Porod, V E Demidov, S Urazhdin, S O Demokritov, E Albisetti, D Petti, R Bertacco, H Schultheiss, V V Kruglyak, V D Poimanov, S Sahoo, J Sinha, H Yang, M Münzenburg, T Moriyama, S Mizukami, P Landeros, R A Gallardo, G Carlotti, J-V Kim, R L Stamps, R E Camley, B Rana, Y Otani, W Yu, T Yu, G E W Bauer, C Back, G S Uhrig, O V Dobrovolskiy, B Budinska, H Qin, S van Dijken, A V Chumak, A Khitun, D E Nikonov, I A Young, B W Zingsem, and M Winklhofer. The 2021 magnonics roadmap. *Journal of Physics: Condensed Matter*, 33(41):413001, August 2021. doi:10.1088/1361-648x/abec1a.

[13] Mahdi Jamali, Jae Hyun Kwon, Soo-Man Seo, Kyung-Jin Lee, and Hyunsoo Yang.

Spin wave nonreciprocity for logic device applications. *Scientific Reports*, 3(1), November 2013. doi:10.1038/srep03160.

[14] Vanessa Li Zhang, Kai Di, Hock Siah Lim, Ser Choon Ng, Meng Hau Kuok, Jiawei Yu, Jungbum Yoon, Xuepeng Qiu, and Hyunsoo Yang. In-plane angular dependence of the spin-wave nonreciprocity of an ultrathin film with dzyaloshinskii-moriya interaction. *Applied Physics Letters*, 107(2):022402, July 2015. doi:10.1063/1.4926862.

[15] R.A. Gallardo, T. Schneider, A.K. Chaurasiya, A. Oelschlägel, S.S.P.K. Arekapudi, A. Roldán-Molina, R. Hübner, K. Lenz, A. Barman, J. Fassbender, J. Lindner, O. Hellwig, and P. Landeros. Reconfigurable spin-wave nonreciprocity induced by dipolar interaction in a coupled ferromagnetic bilayer. *Physical Review Applied*, 12(3), September 2019. doi:10.1103/physrevapplied.12.034012.

[16] M. P. Kostylev, G. Gubbiotti, J.-G. Hu, G. Carlotti, T. Ono, and R. L. Stamps. Dipole-exchange propagating spin-wave modes in metallic ferromagnetic stripes. *Physical Review B*, 76(5), August 2007. doi:10.1103/physrevb.76.054422.

[17] Philipp Wessels, Andreas Vogel, Jan-Niklas Tödt, Marek Wieland, Guido Meier, and Markus Drescher. Direct observation of isolated damon-eshbach and backward volume spin-wave packets in ferromagnetic microstripes. *Scientific Reports*, 6(1), February 2016. doi:10.1038/srep22117.

[18] Huajun Qin, Sampo J. Hämäläinen, Kristian Arjas, Jorn Witteveen, and Sebastiaan van Dijken. Propagating spin waves in nanometer-thick yttrium iron garnet films: Dependence on wave vector, magnetic field strength, and angle. *Physical Review B*, 98(22), December 2018. doi:10.1103/physrevb.98.224422.

[19] M. Vogel, P. Pirro, B. Hillebrands, and G. von Freymann. Optical elements for anisotropic spin-wave propagation. *Applied Physics Letters*, 116(26):262404, June 2020. doi:10.1063/5.0018519.

[20] Sergiy Cherepov, Pedram Khalili Amiri, Juan G. Alzate, Kin Wong, Mark Lewis, Pramey Upadhyaya, Jayshankar Nath, Mingqiang Bao, Alexandre Bur, Tao Wu, Gregory P. Carman, Alexander Khitun, and Kang L. Wang. Electric-field-induced spin wave generation using multiferroic magnetoelectric cells. *Applied Physics Letters*, 104(8):082403, February 2014. doi:10.1063/1.4865916.

[21] A. V. Sadovnikov, A. A. Grachev, E. N. Beginin, S. E. Sheshukova, Yu. P. Sharaevskii, and S. A. Nikitov. Voltage-controlled spin-wave coupling in adjacent ferromagnetic-ferroelectric heterostructures. *Physical Review Applied*, 7(1), January 2017. doi:10.1103/physrevapplied.7.014013.

[22] V. N. Krivoruchko, A. S. Savchenko, and V. V. Kruglyak. Electric-field control of spin-wave power flow and caustics in thin magnetic films. *Physical Review B*, 98(2), July 2018. doi:10.1103/physrevb.98.024427.

[23] Bivas Rana and YoshiChika Otani. Voltage-controlled reconfigurable spin-wave nanochannels and logic devices. *Physical Review Applied*, 9(1), January 2018. doi:10.1103/physrevapplied.9.014033.

[24] Noel Perez and Luis Lopez-Diaz. Magnetic field induced spin-wave energy focusing. *Physical Review B*, 92(1), July 2015. doi:10.1103/physrevb.92.014408.

[25] P. G. Gowtham, T. Moriyama, D. C. Ralph, and R. A. Buhrman. Traveling surface spin-wave resonance spectroscopy using surface acoustic waves. *Journal of Applied Physics*, 118(23):233910, December 2015. doi:10.1063/1.4938390.

[26] Xu Li, Dominic Labanowski, Sayeef Salahuddin, and Christopher S. Lynch. Spin wave generation by surface acoustic waves. *Journal of Applied Physics*, 122(4):043904, July 2017. doi:10.1063/1.4996102.

[27] A. V. Sadovnikov, A. A. Grachev, S. E. Sheshukova, Yu. P. Sharaevskii, A. A. Serdobintsev, D. M. Mitin, and S. A. Nikitov. Magnon straintronics: Reconfigurable spin-wave routing in strain-controlled bilateral magnetic stripes. *Physical Review Letters*, 120(25), June 2018. doi:10.1103/physrevlett.120.257203.

[28] Ferran Macià, Andrew D Kent, and Frank C Hoppensteadt. Spin-wave interference patterns created by spin-torque nano-oscillators for memory and computation. *Nanotechnology*, 22(9):095301, January 2011. doi:10.1088/0957-4484/22/9/095301.

[29] P Jobez, I Usmani, N Timoney, C Laplane, N Gisin, and M Afzelius. Cavity-enhanced storage in an optical spin-wave memory. *New Journal of Physics*, 16(8):083005, August 2014. doi:10.1088/1367-2630/16/8/083005.

[30] Andrii V. Chumak, Alexander A. Serga, and Burkard Hillebrands. Magnon transistor for all-magnon data processing. *Nature Communications*, 5(1), August 2014. doi:10.1038/ncomms5700.

[31] L. J. Cornelissen, J. Liu, B. J. van Wees, and R. A. Duine. Spin-current-controlled modulation of the magnon spin conductance in a three-terminal magnon transistor. *Physical Review Letters*, 120(9), March 2018. doi:10.1103/physrevlett.120.097702.

[32] K. S. Das, F. Feringa, M. Middelkamp, B. J. van Wees, and I. J. Vera-Marun. Modulation of magnon spin transport in a magnetic gate transistor. *Physical Review B*, 101(5), February 2020. doi:10.1103/physrevb.101.054436.

[33] Simone Borlenghi, Weiwei Wang, Hans Fangohr, Lars Bergqvist, and Anna Delin. Designing a spin-seebeck diode. *Physical Review Letters*, 112(4), January 2014. doi:10.1103/physrevlett.112.047203.

[34] Jin Lan, Weichao Yu, Ruqian Wu, and Jiang Xiao. Spin-wave diode. *Physical Review X*, 5(4), December 2015. doi:10.1103/physrevx.5.041049.

[35] S. Klingler, P. Pirro, T. Brächer, B. Leven, B. Hillebrands, and A. V. Chumak. Design of a spin-wave majority gate employing mode selection. *Applied Physics Letters*, 105(15):152410, October 2014. doi:10.1063/1.4898042.

[36] Andrey A. Nikitin, Alexey B. Ustinov, Alexander A. Semenov, Andrii V. Chumak, Alexander A. Serga, Vitaliy I. Vasyuchka, Erkki Lähderanta, Boris A. Kalinikos, and Burkard Hillebrands. A spin-wave logic gate based on a width-modulated dynamic magnonic crystal. *Applied Physics Letters*, 106(10):102405, March 2015. doi:10.1063/1.4914506.

[37] Weichao Yu, Jin Lan, and Jiang Xiao. Magnetic logic gate based on polarized spin waves. *Physical Review Applied*, 13(2), February 2020. doi:10.1103/physrevapplied.13.024055.

[38] Y. Au, E. Ahmad, O. Dmytriiev, M. Dvornik, T. Davison, and V. V. Kruglyak. Resonant microwave-to-spin-wave transducer. *Applied Physics Letters*, 100(18):182404, April 2012. doi:10.1063/1.4711039.

[39] Giacomo Talmelli, Thibaut Devolder, Nick Träger, Johannes Förster, Sebastian Wintz, Markus Weigand, Hermann Stoll, Marc Heyns, Gisela Schütz, Iuliana P. Radu, Joachim Gräfe, Florin Ciubotaru, and Christoph Adelmann. Reconfigurable submicrometer spin-wave majority gate with electrical transducers. *Science Advances*, 6(51):eabb4042, December 2020. doi:10.1126/sciadv.abb4042.

[40] E. K. Semenova and D. V. Berkov. Spin wave propagation through an antidot lattice and a concept of a tunable magnonic filter. *Journal of Applied Physics*, 114(1):013905, July 2013. doi:10.1063/1.4812468.

[41] A. V. Sadovnikov, E. N. Beginin, S. A. Odincov, S. E. Sheshukova, Yu. P. Sharaevskii, A. I. Stognij, and S. A. Nikitov. Frequency selective tunable spin wave channeling in the magnonic network. *Applied Physics Letters*, 108(17):172411, April 2016. doi:10.1063/1.4948381.

[42] Ádám Papp, Wolfgang Porod, Árpád I. Csurgay, and György Csaba. Nanoscale spectrum analyzer based on spin-wave interference. *Scientific Reports*, 7(1), August 2017. doi:10.1038/s41598-017-09485-7.

[43] Krzysztof Szulc, Piotr Graczyk, Michał Mruczkiewicz, Gianluca Gubbiotti, and Maciej Krawczyk. Spin-wave diode and circulator based on unidirectional coupling. *Physical Review Applied*, 14(3), September 2020. doi:10.1103/physrevapplied.14.034063.

[44] J. Ding, M. Kostylev, and A. O. Adeyeye. Magnonic crystal as a medium with tunable disorder on a periodical lattice. *Physical Review Letters*, 107(4), July 2011. doi:10.1103/physrevlett.107.047205.

[45] Björn Obry, Philipp Pirro, Thomas Brächer, Andrii V. Chumak, Julia Osten, Florin Ciubotaru, Alexander A. Serga, Jürgen Fassbender, and Burkard Hillebrands. A micro-structured ion-implanted magnonic crystal. *Applied Physics Letters*, 102(20):202403, May 2013. doi:10.1063/1.4807721.

[46] Qi Wang, Andrii V. Chumak, Lichuan Jin, Huaiwu Zhang, Burkard Hillebrands, and Zhiyong Zhong. Voltage-controlled nanoscale reconfigurable magnonic crystal. *Physical Review B*, 95(13), April 2017. doi:10.1103/physrevb.95.134433.

[47] A V Chumak, A A Serga, and B Hillebrands. Magnonic crystals for data processing. *Journal of Physics D: Applied Physics*, 50(24):244001, May 2017. doi:10.1088/1361-6463/aa6a65.

[48] Kyoung-Woong Moon, Byong Sun Chun, Wondong Kim, and Chanyong Hwang. Control of spin-wave refraction using arrays of skyrmions. *Physical Review Applied*, 6(6), December 2016. doi:10.1103/physrevapplied.6.064027.

[49] Carolin Behncke, Christian F. Adolff, Nicolas Lenzing, Max Hänze, Benedikt Schulte, Markus Weigand, Gisela Schütz, and Guido Meier. Spin-wave interference in magnetic vortex stacks. *Communications Physics*, 1(1), September 2018. doi:10.1038/s42005-018-0052-1.

[50] Edoardo Albisetti, Daniela Petti, Giacomo Sala, Raffaele Silvani, Silvia Tacchi, Simone Finizio, Sebastian Wintz, Annalisa Calò, Xiaorui Zheng, Jörg Raabe, Elisa Riedo, and Riccardo Bertacco. Nanoscale spin-wave circuits based on engineered reconfigurable spin-textures. *Communications Physics*, 1(1), September 2018. doi:10.1038/s42005-018-0056-x.

[51] T. Schneider, A. A. Serga, T. Neumann, B. Hillebrands, and M. P. Kostylev. Phase reciprocity of spin-wave excitation by a microstrip antenna. *Phys. Rev. B*, 77:214411, Jun 2008. URL: https://link.aps.org/doi/10.1103/PhysRevB.77.214411, doi:10.1103/PhysRevB.77.214411.

[52] O. Rousseau, B. Rana, R. Anami, M. Yamada, K. Miura, S. Ogawa, and Y. Otani. Realization of a micrometre-scale spin-wave interferometer. *Scientific Reports*, 5(1), May 2015. doi:10.1038/srep09873.

[53] M. Collet, O. Gladii, M. Evelt, V. Bessonov, L. Soumah, P. Bortolotti, S. O. Demokritov, Y. Henry, V. Cros, M. Bailleul, V. E. Demidov, and A. Anane. Spin-wave propagation in ultra-thin YIG based waveguides. *Applied Physics Letters*, 110(9):092408, February 2017. doi:10.1063/1.4976708.

[54] D. A. Bozhko, V. I. Vasyuchka, A. V. Chumak, and A. A. Serga. Magnon-phonon interactions in magnon spintronics (review article). *Low Temperature Physics*, 46(4):383–399, April 2020. doi:10.1063/10.0000872.

[55] R. M. White and F. W. Voltmer. Direct piezoelectric coupling to surface elastic waves. *Applied Physics Letters*, 7(12):314–316, December 1965. doi:10.1063/1.1754276.

[56] Y. Yahagi, B. Harteneck, S. Cabrini, and H. Schmidt. Controlling nanomagnet magnetization dynamics via magnetoelastic coupling. *Physical Review B*, 90(14), October 2014. URL: https://doi.org/10.1103/physrevb.90.140405.

[57] C. Berk, Y. Yahagi, S. Dhuey, S. Cabrini, and H. Schmidt. Controlling the influence of elastic eigenmodes on nanomagnet dynamics through pattern geometry. *Journal of Magnetism and Magnetic Materials*, 426:239–244, March 2017. doi:10.1016/j.jmmm.2016.11.057.

[58] Cassidy Berk, Mike Jaris, Weigang Yang, Scott Dhuey, Stefano Cabrini, and Holger Schmidt. Strongly coupled magnon–phonon dynamics in a single nanomagnet. *Nature Communications*, 10(1), jun 2019. URL: https://doi.org/10.1038/s41467-019-10545-x.

[59] J. Holanda, D. S. Maior, A. Azevedo, and S. M. Rezende. Detecting the phonon spin in magnon–phonon conversion experiments. *Nature Physics*, 14(5):500–506, April 2018. doi:10.1038/s41567-018-0079-y.

[60] S. Davis, A. Baruth, and S. Adenwalla. Magnetization dynamics triggered by surface acoustic waves. *Applied Physics Letters*, 97(23):232507, dec 2010. URL: https://doi.org/10.1063%2F1.3521289, doi:10.1063/1.3521289.

[61] Ayan K. Biswas, Supriyo Bandyopadhyay, and Jayasimha Atulasimha. Acoustically assisted spin-transfer-torque switching of nanomagnets: An energy-efficient hybrid writing scheme for non-volatile memory. *Applied Physics Letters*, 103(23):232401, dec 2013. URL: https://doi.org/10.1063%2F1.4838661, doi:10.1063/1.4838661.

[62] L. Thevenard, I. S. Camara, S. Majrab, M. Bernard, P. Rovillain, A. Lemaître, C. Gourdon, and J.-Y. Duquesne. Precessional magnetization switching by a surface acoustic wave. *Physical Review B*, 93(13), apr 2016. URL: https://doi.org/10.1103/physrevb.93.134430.

[63] P Kuszewski, I S Camara, N Biarrotte, L Becerra, J von Bardeleben, W Savero Torres, A Lemaître, C Gourdon, J-Y Duquesne, and L Thevenard. Resonant

magneto-acoustic switching: influence of rayleigh wave frequency and wavevector. *Journal of Physics: Condensed Matter*, 30(24):244003, may 2018. URL: https://doi.org/10.1088%2F1361-648x%2Faac152, doi:10.1088/1361-648x/aac152.

[64] A. Barra, A. Mal, G. Carman, and A. Sepulveda. Voltage induced mechanical/spin wave propagation over long distances. *Applied Physics Letters*, 110(7):072401, February 2017. doi:10.1063/1.4975828.

[65] Rutger Duflou, Florin Ciubotaru, Adrien Vaysset, Marc Heyns, Bart Sorée, Iuliana P. Radu, and Christoph Adelmann. Micromagnetic simulations of magnetoelastic spin wave excitation in scaled magnetic waveguides. *Applied Physics Letters*, 111(19):192411, nov 2017. URL: https://doi.org/10.1063%2F1.5001077, doi:10.1063/1.5001077.

[66] M. Weiler, L. Dreher, C. Heeg, H. Huebl, R. Gross, M. S. Brandt, and S. T. B. Goennenwein. Elastically driven ferromagnetic resonance in nickel thin films. *Physical Review Letters*, 106(11), mar 2011. URL: https://doi.org/10.1103/physrevlett.106.117601.

[67] L. Dreher, M. Weiler, M. Pernpeintner, H. Huebl, R. Gross, M. S. Brandt, and S. T. B. Goennenwein. Surface acoustic wave driven ferromagnetic resonance in nickel thin films: Theory and experiment. *Physical Review B*, 86(13), October 2012. URL: https://doi.org/10.1103/physrevb.86.134415.

[68] D. Labanowski, A. Jung, and S. Salahuddin. Power absorption in acoustically driven ferromagnetic resonance. *Applied Physics Letters*, 108(2):022905, jan 2016. URL: https://doi.org/10.1063%2F1.4939914, doi:10.1063/1.4939914.

[69] R. Sasaki, Y. Nii, Y. Iguchi, and Y. Onose. Nonreciprocal propagation of surface acoustic wave inNi/LiNbO3. *Physical Review B*, 95(2), January 2017. URL: https://doi.org/10.1103/physrevb.95.020407.

[70] D. Labanowski, A. Jung, and S. Salahuddin. Effect of magnetoelastic film thickness on power absorption in acoustically driven ferromagnetic resonance. *Applied Physics Letters*, 111(10):102904, sep 2017. URL: https://doi.org/10.1063%2F1.4994933, doi:10.1063/1.4994933.

[71] Derek A. Bas, Piyush J. Shah, Michael E. McConney, and Michael R. Page. Optimization of acoustically-driven ferromagnetic resonance devices. *Journal of Applied Physics*, 126(11):114501, September 2019. doi:10.1063/1.5111846.

[72] D. A. Bas, P. J. Shah, A. Matyushov, M. Popov, V. Schell, R. C. Budhani, G. Srinivasan, E. Quandt, N. Sun, and M. R. Page. Acoustically driven ferromagnetic resonance in diverse ferromagnetic thin films. *IEEE Transactions on Magnetics*, pages 1–1, 2020. doi:10.1109/TMAG.2020.3019214.

[73] L. Thevenard, C. Gourdon, J. Y. Prieur, H. J. von Bardeleben, S. Vincent, L. Becerra, L. Largeau, and J.-Y. Duquesne. Surface-acoustic-wave-driven ferromagnetic resonance in (ga,mn)(as,p) epilayers. *Phys. Rev. B*, 90:094401, Sep 2014. URL: https://link.aps.org/doi/10.1103/PhysRevB.90.094401, doi:10.1103/PhysRevB.90.094401.

[74] A. Hernández-Mínguez, F. Macià, J. M. Hernàndez, J. Herfort, and P. V. Santos. Large nonreciprocal propagation of surface acoustic waves in epitaxial ferromagnetic/semiconductor hybrid structures. *Phys. Rev. Applied*, 13:044018, Apr 2020. URL: https://link.aps.org/doi/10.1103/PhysRevApplied.13.044018, doi:10.1103/PhysRevApplied.13.044018.

[75] J. Janušonis, C. L. Chang, P. H. M. van Loosdrecht, and R. I. Tobey. Frequency tunable surface magneto elastic waves. *Applied Physics Letters*, 106(18):181601, May 2015. doi:10.1063/1.4919882.

[76] P. Kuszewski, J.-Y. Duquesne, L. Becerra, A. Lemaître, S. Vincent, S. Majrab, F. Margaillan, C. Gourdon, and L. Thevenard. Optical probing of rayleigh wave driven magnetoacoustic resonance. *Phys. Rev. Applied*, 10:034036, Sep 2018. URL: https://link.aps.org/doi/10.1103/PhysRevApplied.10.034036, doi:10.1103/PhysRevApplied.10.034036.

[77] Blai Casals, Nahuel Statuto, Michael Foerster, Alberto Hernández-Mínguez, Rafael Cichelero, Peter Manshausen, Ania Mandziak, Lucía Aballe, Joan Manel Hernàndez, and Ferran Macià. Generation and imaging of magnetoacoustic waves over millimeter distances. *Phys. Rev. Lett.*, 124:137202, Apr 2020. URL: https://link.aps.org/doi/10.1103/PhysRevLett.124.137202, doi:10.1103/PhysRevLett.124.137202.

[78] Arne Vansteenkiste, Jonathan Leliaert, Mykola Dvornik, Mathias Helsen, Felipe Garcia-Sanchez, and Bartel Van Waeyenberge. The design and verification of MuMax3. *AIP Advances*, 4(10):107133, October 2014. doi:10.1063/1.4899186.

[79] Sergio Rezende. *Fundamentals of magnonics*. Springer, Cham, Switzerland, 2020.

[80] Frederic Vanderveken, Florin Ciubotaru, and Christoph Adelmann. Magnetoelastic waves in thin films. In *Topics in Applied Physics*, pages 287–322. Springer International Publishing, 2021. doi:10.1007/978-3-030-62844-4_12.

[81] Yaroslav Tserkovnyak, Arne Brataas, and Gerrit E. W. Bauer. Spin pumping and magnetization dynamics in metallic multilayers. *Phys. Rev. B*, 66:224403, Dec 2002. URL: https://link.aps.org/doi/10.1103/PhysRevB.66.224403, doi:10.1103/PhysRevB.66.224403.

[82] Y. Tserkovnyak, A. Brataas, and G. E. W. Bauer. Enhanced gilbert damping in thin ferromagnetic films. *Phys. Rev. Lett.*, 88:117601, Feb 2002. URL: https://link.aps.org/doi/10.1103/PhysRevLett.88.117601, doi:10.1103/PhysRevLett.88.117601.

[83] Y. Tserkovnyak, A. Brataas, G. E. W. Bauer, and B. I. Halperin. Nonlocal magnetization dynamics in ferromagnetic heterostructures. *Rev. Mod. Phys.*, 77:1375–1421, Dec 2005. URL: https://link.aps.org/doi/10.1103/RevModPhys.77.1375, doi:10.1103/RevModPhys.77.1375.

[84] F. S. M. Guimarães, A. T. Costa, R. B. Muniz, and D. L. Mills. Spin currents in metallic nanostructures: Explicit calculations. *Phys. Rev. B*, 84:054403, Aug 2011. URL: https://link.aps.org/doi/10.1103/PhysRevB.84.054403, doi:10.1103/PhysRevB.84.054403.

[85] A. Azevedo, L. H. Vilela-Leão, R. L. Rodríguez-Suárez, A. F. Lacerda Santos, and S. M. Rezende. Spin pumping and anisotropic magnetoresistance voltages in magnetic bilayers: Theory and experiment. *Phys. Rev. B*, 83:144402, Apr 2011. URL: https://link.aps.org/doi/10.1103/PhysRevB.83.144402, doi:10.1103/PhysRevB.83.144402.

[86] D. Kobayashi, T. Yoshikawa, M. Matsuo, R. Iguchi, S. Maekawa, E. Saitoh, and Y. Nozaki. Spin current generation using a surface acoustic wave generated via spin-rotation coupling. *Phys. Rev. Lett.*, 119:077202, Aug 2017. URL: https://link.aps.org/doi/10.1103/PhysRevLett.119.077202, doi:10.1103/PhysRevLett.119.077202.

[87] Yunyoung Hwang, Jorge Puebla, Mingran Xu, Aurelien Lagarrigue, Kouta Kondou, and Yoshichika Otani. Enhancement of acoustic spin pumping by acoustic distributed bragg reflector cavity. *Applied Physics Letters*, 116(25):252404, June 2020. doi:10.1063/5.0011799.

[88] Mingran Xu, Jorge Puebla, Florent Auvray, Bivas Rana, Kouta Kondou, and Yoshichika Otani. Inverse edelstein effect induced by magnon-phonon coupling. *Phys. Rev. B*, 97:180301, May 2018. URL: https://link.aps.org/doi/10.1103/PhysRevB.97.180301, doi:10.1103/PhysRevB.97.180301.

[89] Jorge Puebla, Mingran Xu, Bivas Rana, Kei Yamamoto, Sadamichi Maekawa, and Yoshichika Otani. Acoustic ferromagnetic resonance and spin pumping induced by surface acoustic waves. *Journal of Physics D: Applied Physics*, 53(26):264002, May 2020. doi:10.1088/1361-6463/ab7efe.

[90] E. Saitoh, M. Ueda, H. Miyajima, and G. Tatara. Conversion of spin current into charge current at room temperature: Inverse spin-hall effect. *Applied Physics Letters*, 88(18):182509, May 2006. doi:10.1063/1.2199473.

[91] Dahai Wei, Martin Obstbaum, Mirko Ribow, Christian H. Back, and Georg Woltersdorf. Spin hall voltages from a.c. and d.c. spin currents. *Nature Communications*, 5(1), April 2014. URL: https://doi.org/10.1038/ncomms4768.

[92] B A Kalinikos and A N Slavin. Theory of dipole-exchange spin wave spectrum for ferromagnetic films with mixed exchange boundary conditions. *Journal of Physics C: Solid State Physics*, 19(35):7013–7033, December 1986. doi:10.1088/0022-3719/19/35/014.

[93] Jan Achenbach. *Wave propagation in elastic solids: Volume 16*. North-Holland Series in Applied Mathematics & Mechanics. North-Holland Publishing, Oxford, England, January 1984.

[94] Alexander G Gurevich and Gennadii A Melkov. *Magnetization Oscillations and Waves*. CRC Press, Boca Raton, FL, September 1996.

[95] Karl F Graff. *Wave motion in elastic solids*. Dover Books on Physics. Dover Publications, Mineola, NY, June 1991.

[96] Frederic Vanderveken, Jeroen Mulkers, Jonathan Leliaert, Bartel Van Waeyenberge, Bart Sorée, Odysseas Zografos, Florin Ciubotaru, and Christoph Adelmann. Finite difference magnetoelastic simulator. *Open Research Europe*, 1:35, April 2021. doi:10.12688/openreseurope.13302.1.

[97] D. Froes, M. Arana, L. C. Sampaio, and J. P. Sinnecker. Acoustic wave surfing: spin waves and spin pumping driven by elastic wave. *Journal of Physics D: Applied Physics*, 54(25):255001, April 2021. doi:10.1088/1361-6463/abed71.

[98] D. Froes, M. Arana, J. P. Sinnecker, and L. C. Sampaio. Magnetoelastic modes in néel domain walls. *Journal of Applied Physics*, 132(22):223908, December 2022. doi:10.1063/5.0128775.

[99] David Castilla, Rocío Yanes, Miguel Sinusía, Gonzalo Fuentes, Javier Grandal, Marco Maicas, Tomás E. G. Álvarez-Arenas, Manuel Muñoz, Luis Torres, Luis López, and José L. Prieto. Magnetization process of a ferromagnetic nanostrip under the influence of a surface acoustic wave. *Scientific Reports*, 10(1), June 2020. doi:10.1038/s41598-020-66144-0.

[100] Pavol Krivosik and Carl E. Patton. Hamiltonian formulation of nonlinear spin-wave dynamics: Theory and applications. *Phys. Rev. B*, 82:184428, Nov 2010. URL: https://link.aps.org/doi/10.1103/PhysRevB.82.184428, doi:10.1103/PhysRevB.82.184428.

[101] T. Brächer, P. Pirro, and B. Hillebrands. Parallel pumping for magnon spintronics: Amplification and manipulation of magnon spin currents on the micron-scale. *Physics Reports*, 699:1–34, 2017. Parallel pumping for magnon spintronics: Amplification and manipulation of magnon spin currents on the micron-scale. URL: https://www.sciencedirect.com/science/article/pii/S0370157317302004, doi:https://doi.org/10.1016/j.physrep.2017.07.003.

[102] Qi Wang, Philipp Pirro, Roman Verba, Andrei Slavin, Burkard Hillebrands, and Andrii V. Chumak. Reconfigurable nanoscale spin-wave directional coupler. *Science Advances*, 4(1):e1701517, January 2018. doi:10.1126/sciadv.1701517.

[103] Abdulqader Mahmoud, Florin Ciubotaru, Frederic Vanderveken, Andrii V. Chumak, Said Hamdioui, Christoph Adelmann, and Sorin Cotofana. Introduction to spin wave computing. *Journal of Applied Physics*, 128(16):161101, October 2020. doi:10.1063/5.0019328.

[104] M. Madami, S. Bonetti, G. Consolo, S. Tacchi, G. Carlotti, G. Gubbiotti, F. B. Mancoff, M. A. Yar, and J. Åkerman. Direct observation of a propagating spin wave induced by spin-transfer torque. *Nature Nanotechnology*, 6(10):635–638, August 2011. doi:10.1038/nnano.2011.140.

[105] T Yoshino, K Ando, K Harii, H Nakayama, Y Kajiwara, and E Saitoh. Quantifying spin mixing conductance inF/pt (f=ni, fe, and ni81fe19) bilayer film. *Journal of Physics: Conference Series*, 266:012115, January 2011. doi:10.1088/1742-6596/266/1/012115.

[106] A. Conca, E. Th. Papaioannou, S. Klingler, J. Greser, T. Sebastian, B. Leven, J. Lösch, and B. Hillebrands. Annealing influence on the gilbert damping parameter and the exchange constant of CoFeB thin films. *Applied Physics Letters*, 104(18):182407, May 2014. doi:10.1063/1.4875927.

[107] M Gueye, F Zighem, M Belmeguenai, M S Gabor, C Tiusan, and D Faurie. Spectroscopic investigation of elastic and magnetoelastic properties of CoFeB thin films. *Journal of Physics D: Applied Physics*, 49(14):145003, March 2016. doi:10.1088/0022-3727/49/14/145003.

[108] Sergio C. Guerreiro and Sergio M. Rezende. Magnon-phonon interconversion in a dynamically reconfigurable magnetic material. *Physical Review B*, 92(21), December 2015. doi:10.1103/physrevb.92.214437.

[109] Evan O. Kane. Theory of tunneling. *Journal of Applied Physics*, 32(1):83–91, January 1961. doi:10.1063/1.1735965.

[110] Felipe Garcia-Sanchez, Pablo Borys, Rémy Soucaille, Jean-Paul Adam, Robert L. Stamps, and Joo-Von Kim. Narrow magnonic waveguides based on domain walls.

*Physical Review Letters*, 114(24), June 2015. doi:10.1103/physrevlett.114.247206.

[111] K. Wagner, A. Kákay, K. Schultheiss, A. Henschke, T. Sebastian, and H. Schultheiss. Magnetic domain walls as reconfigurable spin-wave nanochannels. *Nature Nanotechnology*, 11(5):432–436, February 2016. doi:10.1038/nnano.2015.339.

[112] J. Jorzick, S. O. Demokritov, B. Hillebrands, M. Bailleul, C. Fermon, K. Y. Guslienko, A. N. Slavin, D. V. Berkov, and N. L. Gorn. Spin wave wells in nonellipsoidal micrometer size magnetic elements. *Physical Review Letters*, 88(4), January 2002. doi:10.1103/physrevlett.88.047204.

[113] Volker Sluka, Tobias Schneider, Rodolfo A. Gallardo, Attila Kákay, Markus Weigand, Tobias Warnatz, Roland Mattheis, Alejandro Roldán-Molina, Pedro Landeros, Vasil Tiberkevich, Andrei Slavin, Gisela Schütz, Artur Erbe, Alina Deac, Jürgen Lindner, Jörg Raabe, Jürgen Fassbender, and Sebastian Wintz. Emission and propagation of 1d and 2d spin waves with nanoscale wavelengths in anisotropic spin textures. *Nature Nanotechnology*, 14(4):328–333, February 2019. doi:10.1038/s41565-019-0383-4.

[114] Frederic Vanderveken, Jeroen Mulkers, Jonathan Leliaert, Bartel Van Waeyenberge, Bart Soree, Odysseas Zografos, Florin Ciubotaru, and Christoph Adelmann. Finite difference magnetoelastic simulator. *Open Research Europe*, 1(1):35, January 2021. doi:10.12688/openreseurope.13302.1.

[115] R. D. Gomez, J. S. Ma, A. Arkilic, S. H. Chung, and C. Krafft. Vortex-antivortex creation and annihilation on CoFeB crosstie patterns. *Journal of Applied Physics*, 109(7):07D310, April 2011. doi:10.1063/1.3536342.

[116] Claudia Hengst, Manfred Wolf, Rudolf Schäfer, Ludwig Schultz, and Jeffrey McCord. Acoustic-domain resonance mode in magnetic closure-domain structures: A probe for domain-shape characteristics and domain-wall transformations. *Physical Review B*, 89(21), June 2014. doi:10.1103/physrevb.89.214412.

[117] Lukas Döring, Claudia Hengst, Felix Otto, and Rudolf Schäfer. Interacting tails of asymmetric domain walls: Theory and experiments. *Physical Review B*, 93(2), January 2016. doi:10.1103/physrevb.93.024414.

[118] Sampo J. Hämäläinen, Marco Madami, Huajun Qin, Gianluca Gubbiotti, and Sebastiaan van Dijken. Control of spin-wave transmission by a programmable domain wall. *Nature Communications*, 9(1), November 2018. doi:10.1038/s41467-018-07372-x.

[119] Rasmus B. Holländer, Cai Müller, Julius Schmalz, Martina Gerken, and Jeffrey McCord. Magnetic domain walls as broadband spin wave and elastic magnetisation wave emitters. *Scientific Reports*, 8(1), September 2018. doi:10.1038/s41598-018-31689-8.

[120] B A Kalinikos and A N Slavin. Theory of dipole-exchange spin wave spectrum for ferromagnetic films with mixed exchange boundary conditions. *Journal of Physics C: Solid State Physics*, 19(35):7013–7033, dec 1986. URL: https://doi.org/10.1088%2F0022-3719%2F19%2F35%2F014, doi:10.1088/0022-3719/19/35/014.

[121] Frederic Vanderveken, Jeroen Mulkers, Jonathan Leliaert, Bartel Van Waeyenberge, Bart Sorée, Odysseas Zografos, Florin Ciubotaru, and Christoph Adelmann. Confined magnetoelastic waves in thin waveguides. *Physical Review B*, 103:054439, February 2021. doi:10.1103/PhysRevB.103.054439.

[122] K. Yu. Guslienko and A. N. Slavin. Boundary conditions for magnetization in magnetic nanoelements. *Physical Review B*, 72(1), July 2005. doi:10.1103/physrevb.72.014463.

[123] Q. Wang, B. Heinz, R. Verba, M. Kewenig, P. Pirro, M. Schneider, T. Meyer, B. Lägel, C. Dubs, T. Brächer, and A. V. Chumak. Spin pinning and spin-wave dispersion in nanoscopic ferromagnetic waveguides. *Physical Review Letters*, 122(24), June 2019. doi:10.1103/physrevlett.122.247202.

# APPENDICES

# Appendix A

# Experimental work

The following appendix provides information on the experimental results obtained during the course of this study, the fabrication and characterization of the samples. Although these results were not conclusive and were not included in the main text due to the ongoing nature of the work, they are presented here as a reference for future investigations in the field.

The samples were fabricated using thin film growth and nanolithography techniques, and characterized using a range of techniques, including X-ray diffraction, electron microscopy, and Brillouin light scattering. This appendix provides descriptions of the experimental procedures and techniques used, as well as the obtained results and their interpretation.

## A.1 Introduction

The present work aims to experimentally study the elastic excitation of spin waves due to the magnetoelastic interaction for magnonic applications. The use of surface acoustic waves (SAWs) to excite spin dynamics has attracting interest for the fundamental aspects of the interaction between the magnon and phonon quasi-particles but also for the technological prospective of Joule effect-free computing devices. In this project we employed an experimental approach to elastically excite the magnetization of magnetoelastic samples.

In the preliminary results we have fabricated crystalline piezoelectric thin films with the sputtering technique, and characterized by X-ray diffraction and scanning electron microscopy. Electron-beam lithography was employed to fabricate interdigital transducers on the piezoelectric/magnetostrictive (ZnO/YIG) film. Electrical transmission measurements and Brillouin light scattering measurements have shown that the ferromagnetic resonance of the YIG was excited but no elastic signal was found, showing that the SAWs presented a strong attenuation either due to the cristallinity of the piezoelectric film and/or due to the electrical measurement system.

## A.2 Objectives

This study aims to investigate the elastic excitation of spin-waves and the magnetoelastic interaction in coupled piezoelectric-magnetostrictive thin films through a combination of electrical transmission and light scattering experiments. The objective is to fabricate surface acoustic wave devices that are coupled to magnetostrictive materials. To achieve this goal, several steps must be undertaken.

Initially, high-quality piezoelectric ZnO films will be obtained via magnetron sputtering by depositing ZnO under different conditions and performing thermal treatment of the samples under varying annealing temperatures. Subsequently, scanning electron microscopy (SEM) and X-ray diffraction (XRD) will be used to verify the orientation of grains and crystallinity, and the optimal parameters for deposition and annealing will be selected.

Interdigital transducers (IDTs) will be fabricated on the ZnO piezoelectric films using electron-beam lithography. This will involve performing electron-beam lithography steps under different exposition parameters to obtain the desired pattern on the ZnO film, depositing metal, and performing lift-off. SEM images will be obtained to verify the quality of the structures, and the optimal fabrication parameters will be determined.

Finally, the final sample will consist of a bulk YIG magnetic film that is deposited via liquid phase epitaxy on a GGG substrate. The ZnO deposition and IDT patterning will be performed on this sample using the aforementioned optimal parameters. Electrical transmission experiments will be conducted between IDTs, with and without the presence of an external magnetic field. Additionally, Brillouin light scattering experiments will be performed to probe the coupling of spin-waves to the surface acoustic waves that are excited by the IDTs.

## A.3 Methods

### A.3.1 Sample fabrication

#### Magnetron sputtering

The deposition of films was achieved by the magnetron sputtering technique in high vacuum chamber, with base pressure in the order of $10^{-8}$ Torr. A 6-targets AJA International magnetron sputtering was used at the multi-user laboratory LABSURF/LABNANO/CBPF, controled by the Phase II AJA software. The targets are connected to either DC or RF power sources, and several parameters can be controlled for the deposition, such as the source power (or current), deposition time, working gas (argon and oxygen were employed in this work), deposition pressure and temperature.

Before the sample deposition, a deposition rate calibration step is performed by depositing the target material on a silicon substrate for a fixed amount of time under the exact deposition conditions. The film thickness, and thus the deposition rate, is obtained by an X-ray reflectivity measurement in a PANanalytical X'Pert PRO (Philips, Panalytical) diffractometer, with a Cu-K$\alpha_1$ source (0.154056 nm wavelength).

#### Nanolithography

Optical and electron-beam lithography techniques were employed for the fabrication of the interdigital transducers (IdTs) at the LABNANO/CBPF facilities.

The optical lithography was used for obtaining samples with dimensions higher than 10 $\mu$m, using a Heidelberg $\mu$PG 101 Laser Writer machine. For the samples used in this work a positive AZ1505 Clariant resist, with spectral photosensitivity between 310 and 440 nm were deposited in a class 1000 cleanroom with a spin coating technique. The resist 0.5 $\mu$m thickness was achieved by a 4000 rpm rotation for 40 seconds, followed be a thermal treatment at 100$^o$C at a hot plate for 60 seconds. The resist is then exposed to the laser in the areas determined by a LibreCad software file, with a optimum power and exposure time, which have to be calibrated before the exposition. After the laser exposition, a Clariant AZ300 MIF Photoresist developer is applied for 60 seconds at the sample in order to solubilize only the laser-exposed areas. The metal deposition step is then performed,

and a lift-off step is done by submerging the sample in acetone, in a ultrasonic bath, until the resist is fully dissolved and the geometry is imprinted on the substrate.

The electron-beam lithography with a Raith e-LiNE lithographic system was used for obtaining structure up to 500 nm in size. A working distance of 5.4 mm, 30 $\mu$m aperture size and a writefield of 100 $\mu$m were emplóyed in this work. A positive AR-P 672.045 resist from ALLRESIST was spin-coated to the substrate at 2000 rpm for 60 seconds, then places in a hot place at $150^o$ C for 3 minutes. The sample is then places in the Raith e-LiNE, where image calibration steps are performed, i.e. focus, astigmatism and writefield alignments, until obtaining a spot size around 15 nm. Then an e-beam exposure is performed with a pre-calibated dose, typically between 80-110 $\mu C/cm^2$. The sample is then developed at a 70% isopropyl alcohol 30% water mixture for 60 seconds. The desired material is sputtered on the substrate, and a lift-off with acetone is performed. For insulating substrate, such as ZnO, before the e-beam exposure, a 3 nm gold conducting layer is deposited on top of the resist to avoid charging effects.

### A.3.2 Sample characterization

#### X-ray diffraction

X-ray diffraction was used to obtain the crystal structure of the samples. A PANanalytical X'Pert PRO (Philips, Panalytical) diffractometer with a Cu-K$\alpha_1$ source, with a 0.154056 nm wavelength was employed.

#### Scanning Electron Microscope

A Jeol 7100FT Field Emission Gun (FEG) scanning electron microscope (SEM) with 1.2 nm resolution (30 kV) was used for obtaining images of the surface and cross section of the samples.

#### Brillouin Light Scattering

We employed wave-vector-resolved Brilouin light scattering (BLS) spectroscopy in order to measure the magnetic and elastic waves signal in the device under RF excitation. The experimental set-up is depicted in figure A.1.

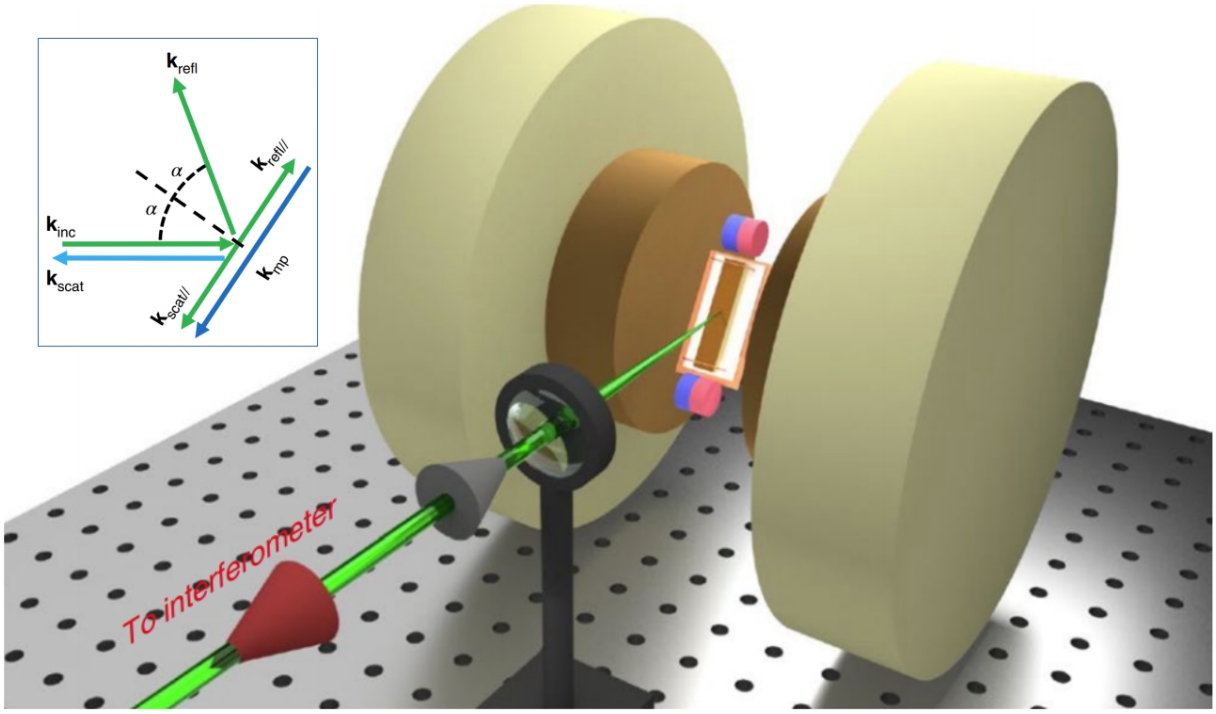


Figure A.1: Wave-vector-resolved Brillouin light scattering (BLS) spectroscopy experimental setup. The inset shows the conservation of wave-vector under the inelastic scattering of the incident laser light. Extracted from [59] (modified).

A silver film was attached behind the YIG/GGG device in order to scatter the incident laser ray inside the sample. The scattered light is collimated by an objective lens and is guided to a Fabry-Perot interferometer for frequency analysis.

In this configuration, from the conservation of angular momentum we obtain that the measured signal wave-vector is

$$k = 2k_L n \sin\alpha, \tag{A.1}$$

where $k_L$ is the laser wave-vector, $n$ is the index of refraction and $\alpha$ is the incidence angle. Thus, the wave-vector-resolution is obtained by varying the incidence angle $\alpha$. As we employed a 532 nm wavelength laser and considering the YIG index of refraction as $n = 2.2$, we obtain the relation $k = (5.197 \times 10^7) \sin\alpha \text{ m}^{-1}$ for our analysis.

## A.4 Preliminary results

The experimental work aimed to achieve surface acoustic wave devices in order to excite the dynamics of adjacent magnetic thin films. In order to do so, we started by obtaining high quality piezoelectric films, ZnO was the choice, from magnetron sputtering deposition. Then, producing metallic interdigital transducers (IdTs) from electron-beam lithography and lift-off onto the insulating piezoelectric surfaces. And finally, by doing electrical contacts in the transducers and performing transport and light scattering experiments.

### A.4.1 Device fabrication

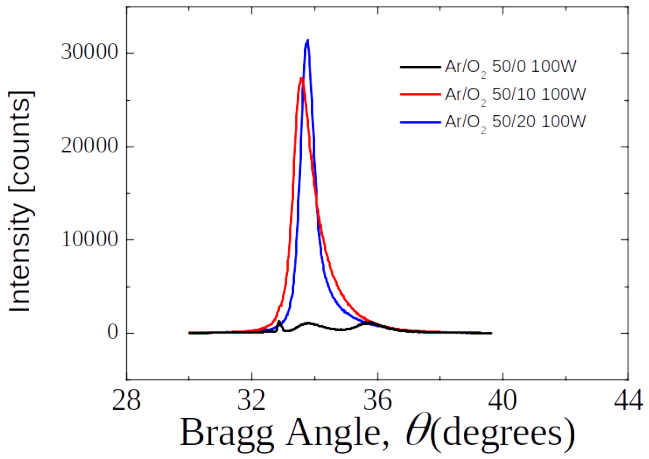


Figure A.2: XRD spectra of ZnO films deposited at room temperature (RT) without annealing at 100 W power for different Ar/O2 proportion atmospheres. The film deposited without oxygen (50/0) was the only one not to show the c-axis (002) orientation.

We employed the magnetron sputtering technique in order to deposit high quality piezoelectric ZnO films on either Si or YIG/GGG substrates. The deposition conditions and thermal treatment were varied in order to optimize the c-axis orientation of the film, seen at the (002) crystalline direction in the XRD spectrum. The film deposition rate was first calibrated for each deposition condition, and then a 1 $\mu m$ ZnO film was deposited and its XRD spectrum was obtained.

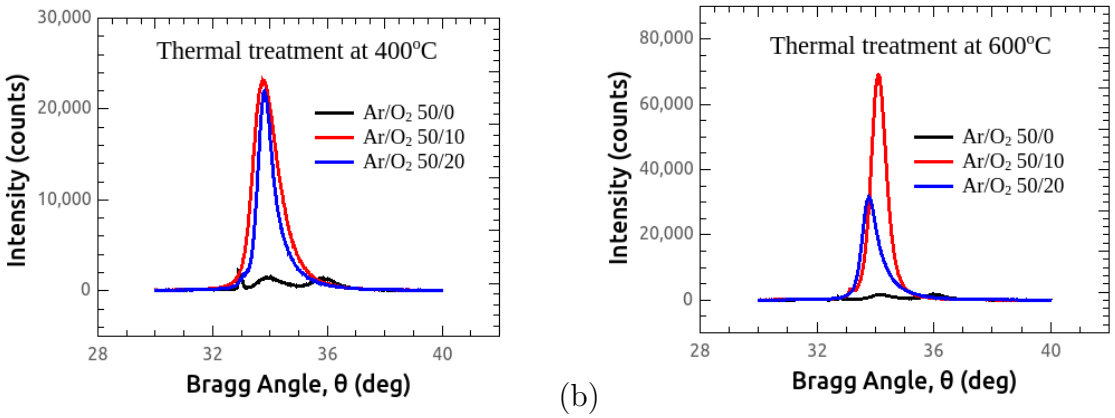


Figure A.3: XRD spectra of ZnO films deposited at room temperature after thermal treatment at (a) 400C and (b) at 600C for one hour at 100 W power for different $Ar/O_2$ proportion atmospheres.

We started by depositing at room temperature (RT) the ZnO films over Si by RF-magnetron sputtering at 100 W power, under a 5 mTorr base pressure with different $Ar/O_2$ flux (sccm) proportions: (a) pure Ar (50/0), (b) 50/10 and (c) 50/20 ratio atmosphere, without thermal treatment. The corresponding XRD spectra of these samples are shown in figure A.2. Different from the the pure Ar (50/0) atmosphere sample, which did not present the c-axis orientation, the mixed $Ar+O_2$ were indeed oriented in that direction.

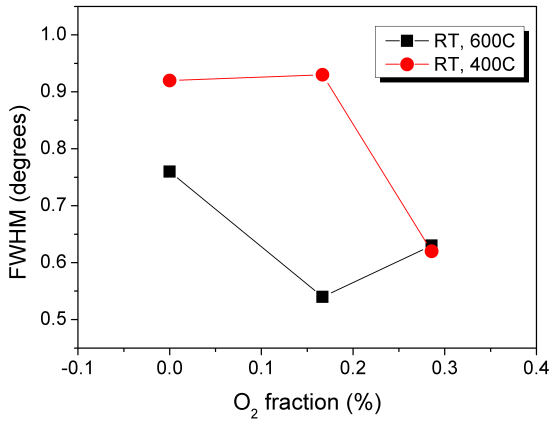


Figure A.4: These FWHM of the (002) peak as a function of the $0_2$ fraction and the annealing temperature are summarized.

We then checked the effect of a post-deposition thermal treatment for one hour at two different temperatures, either (a) 400C or (c) 600C, see figure A.3. The 50/0 $Ar/O_2$ samples did not become oriented after the annealing, but the other samples crystallinity was increased, and the 600C temperature was more effective than the 400C treatment, especially in the 50/10 sample.

In order to check the grain orientation in these samples, we obtained scanning electron microscopy (SEM) images of their cross section, by cleaving after freezing with liquid nitrogen. The images of the cleaved regions is shown in figure A.5. As expected, in the pure argon (50/0) samples, a and b, no grain orientation can be seen. Differently, the other samples a c-axis orientation is present at different levels. The most distinct sample is, just like from the XRD results, the 50/10 $Ar/O_2$ with annealing at 600C, figure A.5d.

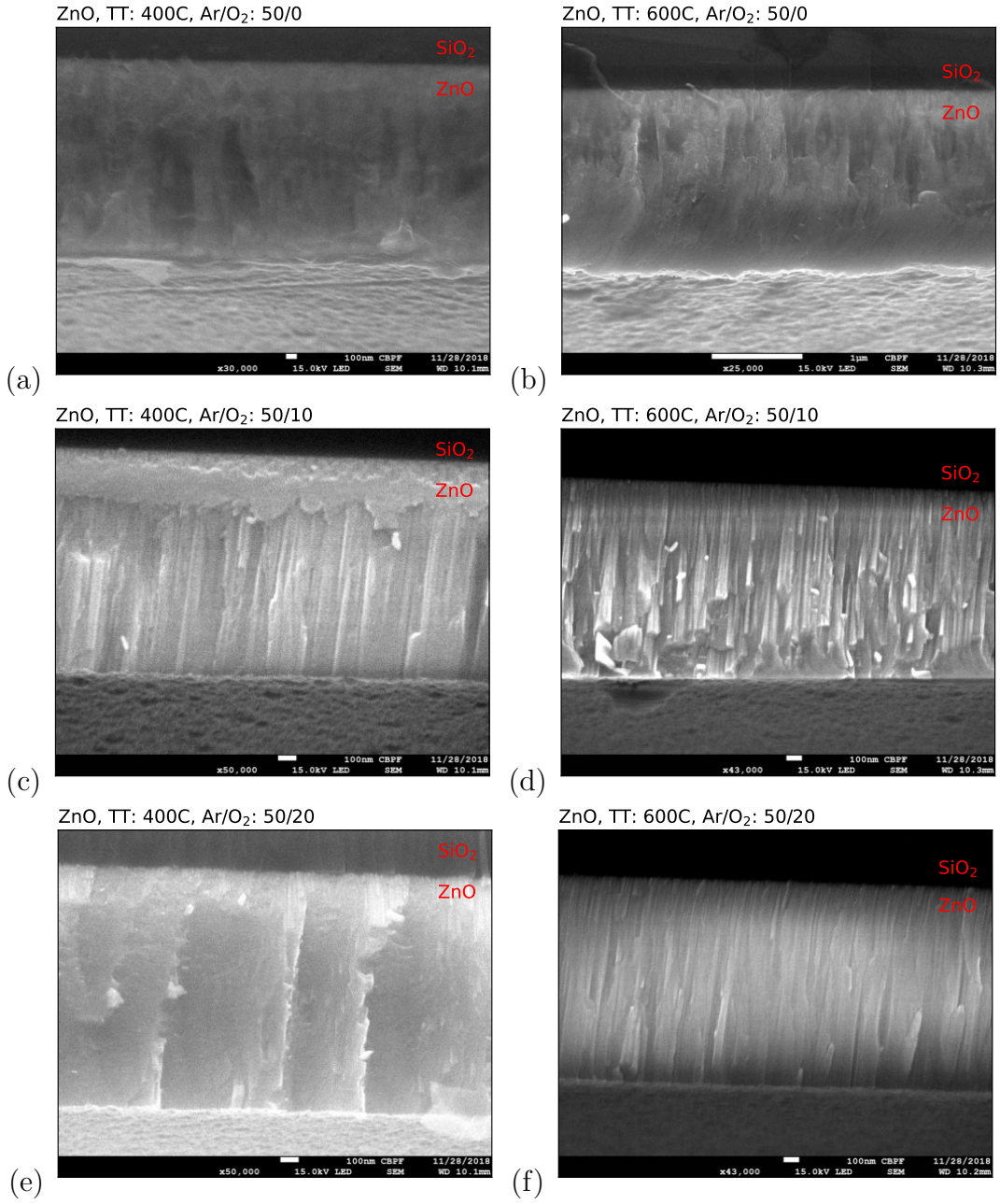


Figure A.5: SEM images of the cross section of the $ZnO/SiO_2$ film at different deposition conditions.

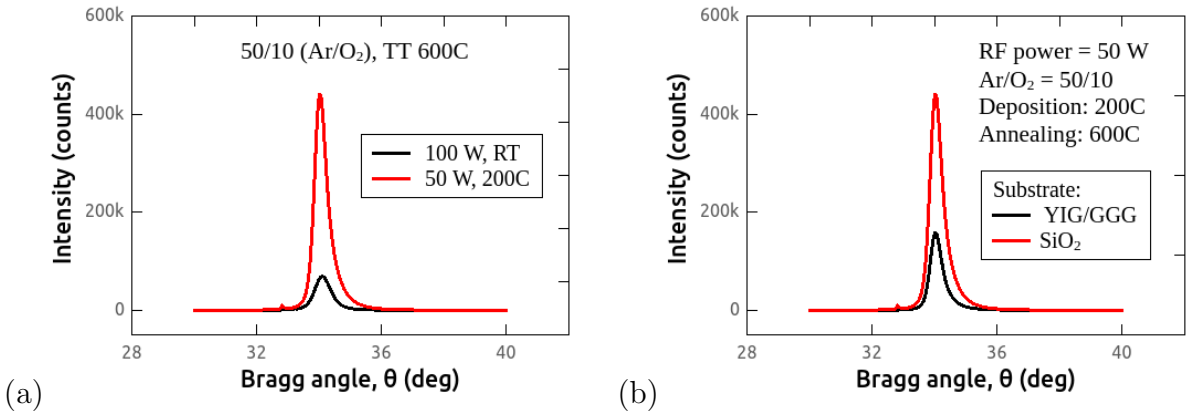


Figure A.6: (a) XRD spectra of the ZnO deposited on $SiO_2$ substrates with a 50/10 $Ar/O_2$ atmosphere ratio and thermal treatment for one hour at 600C under different RF power and deposition temperature. (b) XRD spectra of the final ZnO films. The FWHM were, respectively, 0.44 and 0.42 for $SiO_2$ and YIG/GGG substrates.

The film quality was further enhanced by having the deposition at a 200C temperature and lowering the RF power to 50 W, which reduced the deposition rate, see figure A.6a, where the FWHM could be reduced from 0.54 to 0.44. These were defined as the final optimum deposition conditions in our samples, see table A.1, and these conditions were tested in both the $SiO_2$ and the YIG/GGG subtrates, where the FWHM were respectively 0.44 and 0.42, as shown in figure A.6b.

| | |
|---|---|
| RF power | 50 W |
| Base pressure | 6 mTorr |
| $Ar/O_2$ ratio | 50/10 (sccm/sccm) |
| Deposition temperature | 200C |
| Annealing temperature | 600C |
| Film thickness | 1 $\mu$m |

Table A.1: Final ZnO magnetron sputtering deposition conditions to optimize the (002) grain orientation.

Interdigital transducers were then fabricated on top of the ZnO films from electron-beam lithography. As the films are insulating, in order to perform the e-beam exposition,

a 3 nm gold conductive layer had to be deposited on top of the resist. After exposition and development, a 60 nm gold layer was deposited and a lift-off step was performed. The final structures are shown in figure A.7, where 550 nm fingers with periodicity p = 4 $\mu$m, which corresponds a wavelength of $\lambda = 2p = 8$ $\mu$m.

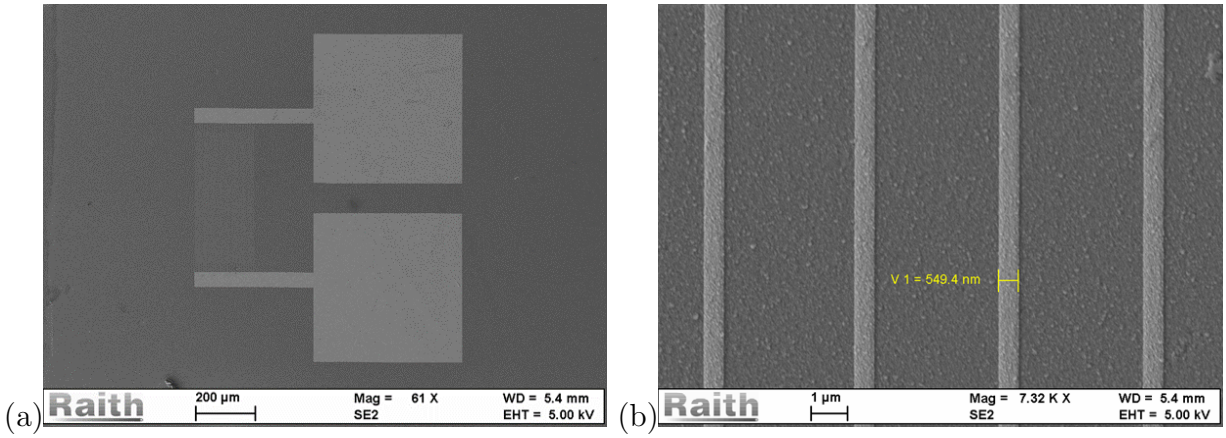


Figure A.7: Au interdigital transducers fabricated by electron-beam lithography and lift-off. The fingers were designed to have 500 nm width, with 4 $\mu$m separation.

The final sample model is shown in figure A.8. The process of fabrication can be summarized as:

1. YIG samples deposited on GGG substrates either via liquid phase epitaxy (LPE), crystalline bulk with 7 $\mu$m thickness, or by magnetron sputtering, 500 nm thick thin film, were used.

2. 1 $\mu$m of ZnO film was deposited via magnetron sputtering, keeping the middle of the sample protected by using a kapton tape.

3. Electron-bean lithography was performed on top of the ZnO islands in order to create the IdTs and contact pads geometries.

4. Magnetron sputtering of gold followed by a lift-off process were done to create the transducers.

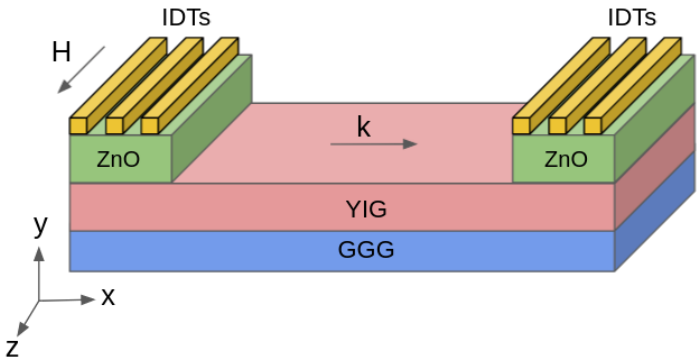


Figure A.8: Final sample model. Interdigital transducers (IdTs) on top of two ZnO islands deposited on a YIG/GGG substrate.

### A.4.2 Device characterization

The electrical transmission characterization was done by connecting the contact pads to SMA connectors using silver conductive ink, see figure A.9. Then the input IdT, was then connected to a RF source and the output IdT was connected to a rectifying diode and the output signal was measured by a DC voltmeter. A resistance measurement was done in order to assure that there was no electrical contact between the two IdTs.

Figure A.9: The experimental IdTs electrical transmission setup. The input IdT is connected to a RF signal generator, and the output IdT, to a rectifying diode and a DC voltmeter.

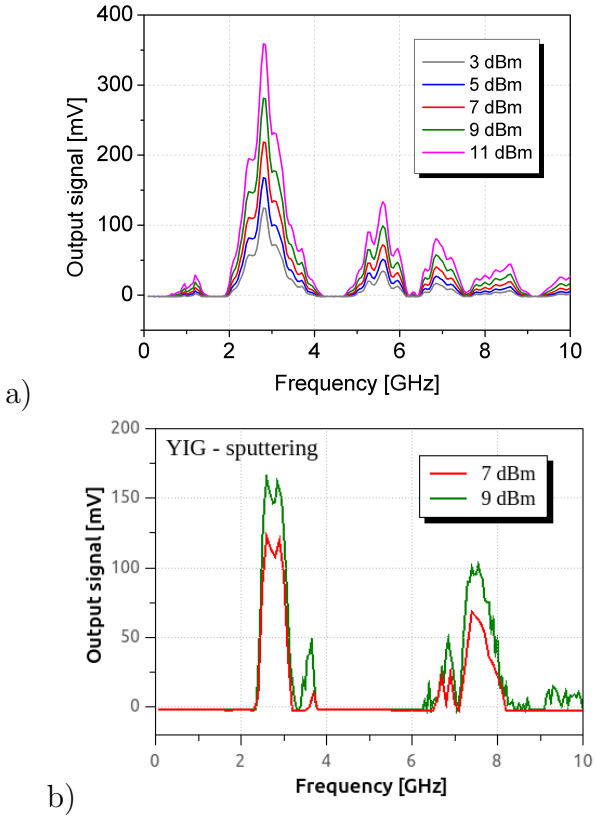


Figure A.10: The rectified DC electrical voltage measured at the output IdT without a bias magnetic field for several input amplitudes for (a) the thick YIG-LPE sample and (b) for the thin YIG-sputtering sample.

The potential difference amplitude measured at the output IdT as a function of the frequency of the input IdT is shown in figure A.10 for several input amplitudes, without a bias magnetic field. For the crystalline thick YIG-LPE sample the output signal, figure A.10a, presents a minor peak at 1.2 GHz and a series of peaks at 2.8, 5.6, 6.9 and 8.3 GHz. The thin YIG-sputtering, figure A.10b, only two major peaks are present, at 2.8 and 7.5 GHz.

In order to verify the transmission of surface acoustic waves from the IdTs a pulsed experiment was performed. Instead of a continuous sinusoidal RF excitation, we excited the input IdT with 100 ns wave packets with a fixed frequency $f$ and the output was connected

to an oscilloscope. This signal was obtained by doing an external modulation with 100 ns wide rectangular function with 2 $\mu$s separation at the sinusoidal signal. We expected the wave packet to be detected in the output with a delay time of 885 ns, as the IdTs separation is 3.4 mm and the YIG sound velocity 3.84 km/s. This output signal, however, was not detected. We attribute this to either the acoustic wave is strongly attenuated along the propagation or it is not even excited in our system. We intend to address this problem by enhancing the ZnO film crystallinity and improving our electric measurement setup.

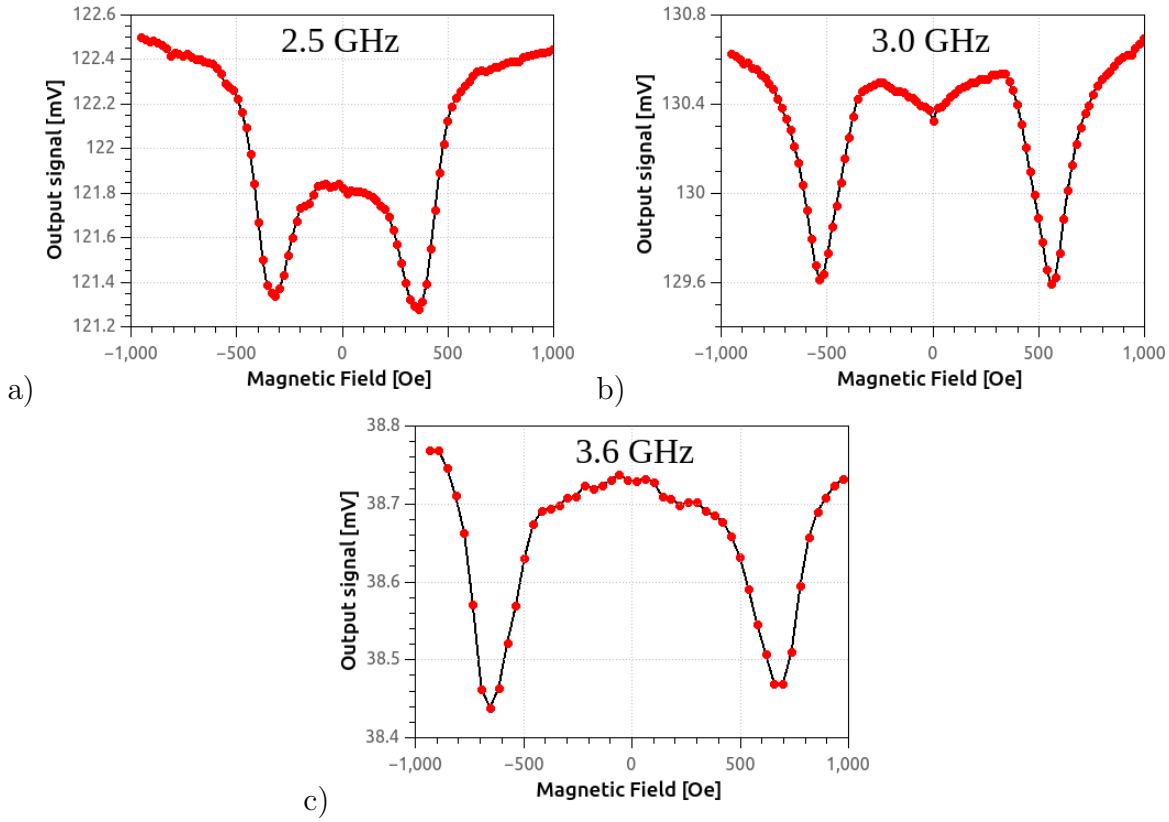


Figure A.11: The rectified DC electrical voltage measured at the output IdT with an applied bias magnetic field for the thin YIG-sputtering sample for several frequencies.

Nevertheless, in order to investigate the physical origin of the output signal shown in figure A.10, we repeated the experiment, an input RF signal with an output connected to a rectifying diode and voltmeter, under a non-null external magnetic field in the YIG-

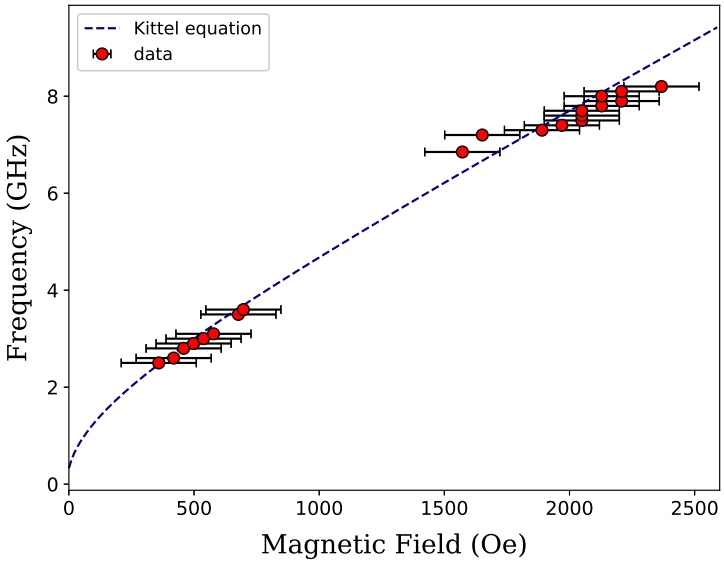


Figure A.12: The external magnetic field with maximum absorption measured at the output IdT for the YIG-sputtering sample plotted as a function of the input frequency in the regions with significant transmission. The data is compared to Kittel's equation for ferromagnetic resonance.

sputtering sample, see figure A.11. For each frequency, a clear absorption can be seen at an specific magnetic field.

As the output signal only presents a strong signal at specific frequency ranges, see figure A.10b, we can only obtain the absorption magnetic field within those ranges. We then plotted the positive magnetic field where the absorption takes place as a function of the frequency, see figure A.12. The result is compared to the ferromagnetic resonance frequency of the YIG sample, obtained from Kittel's formula, $2\pi f = \sqrt{\omega_H(\omega_H + \omega_M\omega_H)}$, with $\omega_M = \gamma 4\pi M_s$, $\omega_H = \gamma(H_0 + H_A + Dk^2)$, where $\gamma$ is the gyromagnetic ratio, $4\pi M_s$ is the saturation magnetization, $H_A$ is the anisotropy field and $D$ is the exchange parameter, using the parameters for YIG [59]: $\gamma = 17.59$ MHz/Oe, $4\pi M_s = 1.76$ kG, $H_A = 7.8$ Oe and $D = 5.4 \times 10^{-9}$ Oe cm$^2$.

This way we attribute the signal measured at the output IdT under an RF excitation in the input IdT to be of electromagnetic nature and not of elastic nature. The alternate signal in the input IdT creates a magnetic field that excites the ferromagnetic resonance

modes of the YIG-sputtering sample, which for instance, inductively create the output electrical signal.

Besides, a Brillouin light scattering (BLS) study of the YIG-LPE sample was performed in order to verify the above-mentioned results. The sample was placed in the BLS setup at a fixed angle of $22^o$, in order to keep the detected wave vector at a fixed value of $k$ = 19.5 $\mu$m$^{-1}$. One of the IDTs was connected to a RF frequency generator, and the other to a rectifying diode and a voltmeter. We then fixed the frequency and varied the external magnetic field on the sample until obtaining a maximum voltage value in the output IDT. The BLS spectrum was then obtained and repeated after a fine variation of the field intensity.

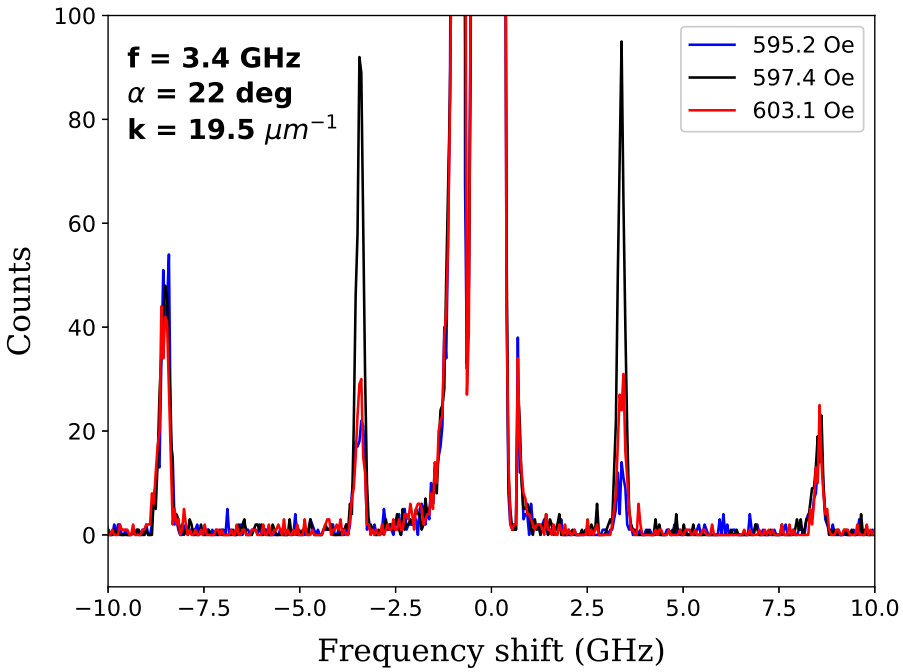


Figure A.13: Brillouin light scattering (BLS) spectrum of the sample for a microwave input of 3.4 GHz under three different external magnetic field values. The sample was measured with an incidence angle of $\alpha$ = 22 degrees (k = 19.5 $\mu$m$^{-1}$).

Examples of the resulting spectrum are shown in figure A.13 for a 3.4 GHz frequency for magnetic field values around 600 Oe. In each spectrum two peaks at ±8.55 GHz correspond to thermal phonons, which do not change with the input frequency, and two peaks at the

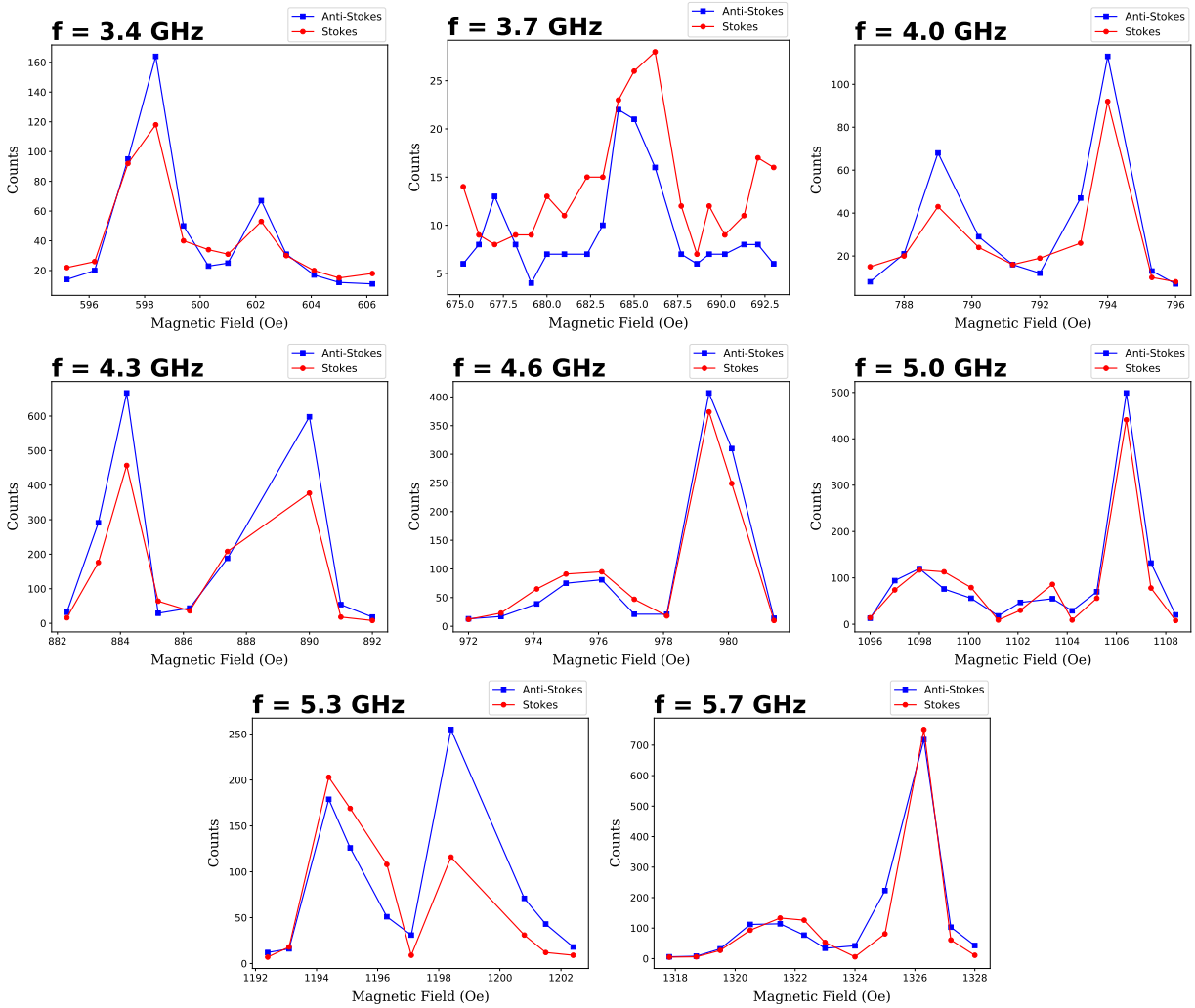


Figure A.14: BLS amplitude, Stokes and Anti-Stokes, at the corresponding microwave frequency for a fixed angle of $\alpha = 22$ degrees (k = 19.5 $\mu$m$^{-1}$) under different magnetic bias field intensities.

same frequency as the RF excitation frequency, 3.4 GHz in this example. By varying the magnetic field intensity, as expected, the thermal phonons counts is practically unchanged, but the RF excitation is significantly altered, which is an indication that we are actually measuring magnons.

The BLS intensity at the frequency coincident with the RF excitation was obtained for

several magnetic field values, as mentioned above. The frequency was then varied and the same procedure was repeated. The results are shown in Figure A.14, where each point was obtained from the amplitude of the RF frequency at the corresponding BLS spectrum.

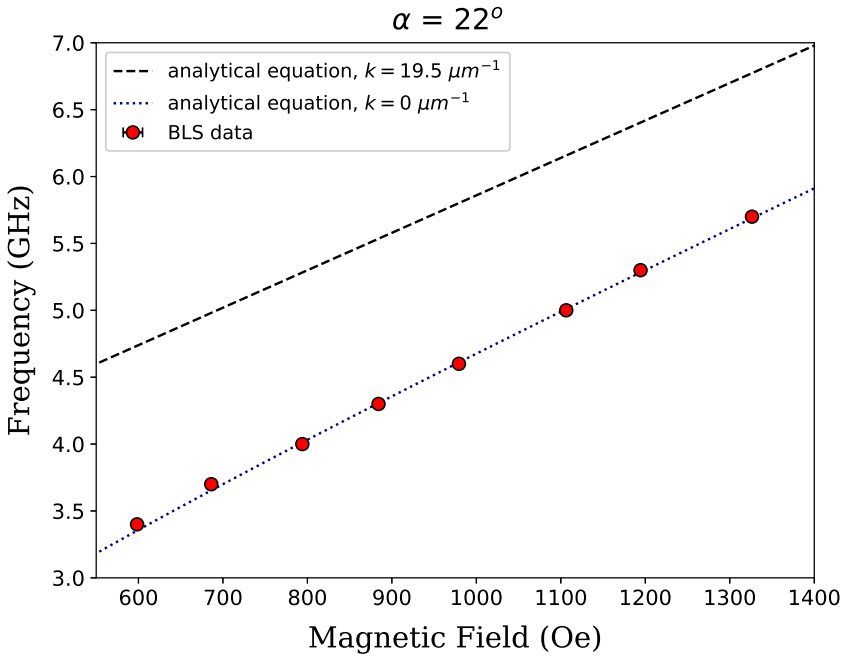


Figure A.15: The BLS peak positions as a function of the external magnetic field for a fixed incidence angle of $\alpha = 22^o$. The dashed lines correspond to the analytical model for magnetostatic surface spin waves for $k = 19.5\mu m^{-1}$, and the dotted lines for $k = 0$ (FMR).

In most of the graphs of Figure A.14 two peaks can be seen, a major and a minor one. The magnetic field in which there is a maximum count as a function of the RF frequency is shown in the dispersion relation shown in Figure A.15. We can compare the results with the theoretical equation for magnetostatic surface spin waves in a thin film where $\vec{k} \perp \vec{m}$ [79],

$$2\pi f = \sqrt{\omega_H^2 + \omega_M \omega_H + \frac{\omega_M^2}{4}(1 - e^{-2kt})}, \tag{A.2}$$

with $\omega_M = \gamma 4\pi M_s$, $\omega_H = \gamma(H_0 + H_A + Dk^2)$, where $\gamma$ is the gyromagnetic ratio, $4\pi M_s$ is the saturation magnetization, $H_A$ is the anisotropy field, $D$ is the exchange parameter and $t$, the film thickness. Using the parameters for YIG [59]: $\gamma = 17.59$ MHz/Oe, $4\pi M_s$

= 1.76 kG, $H_A$ = 7.8 Oe, $D = 5.4 \times 10^{-9}$ Oe cm$^2$ and $t = 7$ $\mu m$, we obtain the analytical equations of Figure A.15.

The experimental and the analytical equation for $k = 19.5$ $\mu m^{-1}$, however, do not fit each other. The data is, however, well-fitted with the ferromagnetic resonance (FMR), $k = 0$, which indicates that the magnetic field excited by the transducers is of long-range compared to the BLS laser spot size, generating a infinite wavelength (k = 0) magnetic excitation. This result is in tune with the IdT electrical transmission experiment performed in the YIG-sputtering sample that the transducers are acting as electromagnetic emitters and not exciting acoustic waves.

## A.5 Conclusion and future work

In this project we aimed to study the magnetoelastic interaction by means of the experimental fabrication of piezoelectric/magnetostrictive samples and magnetic and elastic characterization of the coupled excitation, mainly by means of electric transport and Brillouin light scattering experiments.

The experimental work focused in obtaining good quality piezoelectric ZnO films via the magnetron sputtering technique by varying the deposition and annealing parameters. The best parameters were chosen and interdigital transducers (IDTs) were patterned on their surface, through electron-beam lithography. Electron transmission measurements of between the two pairs of IDTs were performed, and a series of resonant peaks were found in the frequency domain.

These peaks, however, were not associated with the propagation of surface acoustic waves in the sample, as pulse propagation experiments did not show the expected sound wave velocity. We believe that the acoustic wave signal is highly attenuated in the sample, which cannot be detected in our setup, and the electromagnetic induction creates a cross-talk between IDTs which overshadows the SAW signal. The main excitation presented in the sample is, then, of electromagnetic origin and no elastic waves were detected.

A sample of bulk YIG over a GGG substrate underwent the above-mentioned procedure, ZnO deposition and IDT patterning via e-beam lithography, and the same resonant peaks were found in the electric transmission experiment, here also associated to electromagnetic cross-talk between IDTs. By varying the external magnetic field, under a constant

frequency, an absorption was seen in the output voltage at a resonant field. These absorptions are associated to the ferromagnetic resonance eigenmodes of the YIG sample. This sample was studied by Brillouin light scattering experiments, where no phonon signal was detected, but the magnon signal was present. This is in consonance with the interpretation of the electromagnetic excitation of the uniform magnon mode ($k = 0$) from the IDT cross-talk.

As next steps, we intend to obtain better surface acoustic wave devices, by improving the quality of the piezoelectric film, enhancing the quality of our electric contacts and finding better a detection set-up for the desired experiment.